NUCLEAR ENGINEERING

MASSACHUSETTS INSTITUTE OF TECHNOLOGY

NATURAL CONVECTION IN HIGH HEAT FLUX TANKS AT THE HANFORD WASTE SITE

Mark van der Helm and Mujid S. Kazimi
February 1996

Acknowledgments

Abstract

A study was carried out on the potential for natural convection and the effect of natural convection in a High Heat Flux Tank, Tank 241-C-106, at the Hanford Reservation. To determine the existence of natural convection, multiple computations based on analytical models were made knowing the tank geometry and contents' thermal characteristics. Each computation of the existence of natural convection was based on the determination of the onset of natural convection generalizing the tank as a 1-D porous medium. Computations were done for a range of permeabilities considering the porous medium alone, with a superposed fluid layer, and with a salt gradient. Considering only the porous medium, the higher permeability value, $3.2 * 10^{-10}$ ft^2, allowed convection, though the lower permeability, $2.6 * 10^{-14}$ ft^2, did not. The presence of the superposed layer induced convection throughout the porous medium for the full range of permeabilities. Considering the effect of the salt gradient and superposed layer together, the effect of the superposed layer is expected to induce convection despite the stabilizing salt gradient. Therefore, natural convection is expected to exist in Tank 241-C-106.

Secondly, because temperature measurements indicated lower temperatures at a location near the center of the tank, a thermal model was used to compute the local effects of a convective annulus around a thermocouple tree at that location. A conduction model of the tank and surroundings was used to bound the local model. The local model allowing convection in the annulus set the size of the annulus based on the known temperature measurements of the thermocouple tree and the boundary conditions set by the conduction model. Previous published calculations on Tank 241-C-106, allowing for only conduction within the tank, reported a steam region at the bottom of the tank with an approximately 24 foot radius. In the present analysis, using the computer code, TEMPEST, it is found that the cooling effect of the annulus creates a region with a 12 foot radius surrounding the thermocouple tree in which the temperature is suppressed below the saturation temperature due to the effects of the convective annulus. The annulus gap width for matching temperatures and the boundary conditions is on the order of 1 inch.

Acknowledgements

Table of Contents

List of Figures

List of Tables

List of Symbols

Variables

a	horizontal wave number
d	annulus thickness [ft]
$\dot{e}$	evaporation rate [in/day]
h	heat transfer coefficient [Btu/hr/ft^2/°F]
h_{fg}	enthalpy of vaporization [Btu/lbm]
k	thermal conductivity [Btu/ft/hr/°F]
n	number of terms in Fourier series expansion
r	radius [ft]
p	pressure [lbf/ft^2]
p'	perturbation pressure [lbf/ft^2]
q	heat flux [Btu/hr/ft^2]
s	solute concentration [wt%]
tcon	contour temperature [°F]
u	x component of velocity [ft/s]
v	y component of velocity [ft/s]
w	z component of velocity [ft/s]
z	vertical distance [ft]
A	area [ft^2]
$\bar{A}$	vector of Fourier expansion coefficients
C_p	heat capacity [Btu/lbm/°F]

D	depth of overlying fluid [ft]
D_p	porous particle diameter [in]
Da	Darcy number
D_d	molecular diffusivity [ft^2/s]
D_d*	effective molecular diffusivity for a porous media [ft^2/s]
H	annulus height [ft]
L	vertical height of porous region being modeled [ft]
$\bar{\bar{M}}$	generated matrix from applying the Galerkin method
Nu	Nusselt number
Pr	Prandtl number
P	permeability of porous matrix [ft^2]
Q_v	internal heat generation of porous region [Btu/hr/ft^3]
R_I	internal Rayleigh number based on internal heat generation
R_E	external Rayleigh number based of boundary temperature differences
R_S	solute Rayleigh number based of solute gradient
Sc	Schmidt number
S	nondimensionalized solute concentration perturbation
T	temperature [°F]
T'	perturbation temperature [°F]
V	volume [ft^3]
W	nondimensionalized vertical velocity
Z	nondimensionalized vertical dimension
α	concentration expansion coefficient[1/°F]

β	thermal expansion coefficient [1/°F]
δ	boundary layer thickness
ε	porosity
γ	ratio of fluid to porous region thermal conductivities
η	ratio of fluid to porous region height
κ	thermal diffusivity [ft^2/s]
μ	fluid viscosity [lbf s/ft^2]
μ'	porous region fluid viscosity [ft^2/s]
ν	dynamic viscosity [ft^2/s]
Θ	nondimensionalized temperature perturbation
ρ	density [lbm/ft^3]
σ	time constant for perturbation
τ	ratio of thermal to molecular diffusivities
Ω	time constant [sec]

Subscripts

a	annulus
b	bottom of region
f	fluid property
i	inner
m	combined property of porous material and saturating fluid
o	outer
p	property of solid material in porous region

t	top of region
u	up
A	air
BL	boundary layer
E	external
I	internal
S	solute
T	total
U	universal
W	water
1	fluid region
2	porous region

Operators

<>	average over the vertical
—	average over the horizontal
D	derivative
Δ	top value less bottom value
$\rightarrow$	vector quantity

Notes

Variables appear italicized in equations but often boldface in the text. No difference in the quantity represented is implied by this difference in style.

Chapter 1

Introduction

1.1 Background

The Hanford Plant near Richland, Washington is one of four main plutonium production facilities that make up the materials production sector of the United States' nuclear weapons complex. Wastes from this processing are categorized as high-level in that they are "aqueous wastes resulting from the operation of the first-cycle solvent extraction system, or equivalent, and concentrated wastes from subsequent extraction cycles, or equivalent, in a facility for reprocessing irradiated fuel" [1]. The wastes are stored in 177 underground tanks, both single-shell and double-shell, containing approximately 200MCi of fission product radionuclides[1].

For all Hanford operations three transport pathways carrying radionuclides from the facility to locations of potential harm to the local population have been hypothesized. These pathways include atmospheric releases, water outlet directly into the Columbia River, and tank leakage to the ground and transfer by groundwater[2,3]. For the third pathway, feasibility studies on the threat to public health from a 'worst case scenario', a large volume release of fresh waste, computed the final health impact to be a radiation exposure equal to 1% of the natural background. The largest tank leak to have happened at Hanford was near 15% of this volume with the surrounding soil of higher radionuclide retention[1][1]. Therefore, only the first two pathways, the atmosphere, and the Columbia River were studied extensively in computing and reporting health impacts. For these pathways the majority of the released radionuclides generated from chemical separation plants and reactor cooling, respectively. Both sources of the releases are no longer in operation. Neither reported radiation exposure exceeded that received from natural background levels[2,3].

---

1. The feasibility study assumed a transport time of 3 years for traveling to the water table. This largest tank leak resulted in transport one half the distance in 20 years.

Present day tank contents consist of plutonium processing waste and additives to ensure safe disposal. Most of the waste originating as acid solutions were neutralized with sodium hydroxide and sodium carbonate which increased the volume and produced precipitate sludge. This addition was made to protect steel liners of the tanks against acid attacks by the high-heat acid solutions. The thermally hot alkaline mixture, however, induced stress corrosion cracking which over time caused leaks. To minimize leakage, a program has been put in place to drain those tanks for which draining will not compromise tank integrity. Thus the tanks contain liquid, sludge, salt cake, with varying amounts of drainable liquid[1].

Current safety analysis involves determining the potential for increased temperature due to migration and concentration of radionuclides causing 'hot spots' which could initiate chemical reactions, initiate nuclear reactions (by reaching criticality), or reduce heat transfer mechanisms. Then increased temperatures could cause pressurization from rapid release of evolved gases within the sludge ('bumping'), flashing steam from water near or at the saturation temperature ('steam bumping'), or runaway reactions (explosions). The increased pressurization could cause tank failure of the steel liner(s) and concrete or degrade the filtered ventilation system for the tank.

Radioactive releases by chemical reaction in a waste system was experienced by the accident in 1957 at Kyshtym, a waste storage facility within the Mayak plutonium production plant located in the Southern Urals in Russia[1]. The tank explosion, releasing approximately 20 MCi of radionuclides, was attributed to a spark from a malfunctioning monitoring system initiating the exothermic reaction of dry sodium acetate and sodium nitrate[4]. Significant differences exist between the conditions at Kyshtym and those presently at Hanford. At Kyshtym high radiation fields near the tank prevented repair of both the monitoring system and the cooling system allowing the tank contents to dry out. For all the tanks at Hanford monitoring systems and cooling systems are checked periodically for damage. In addition, tank contents at Hanford are quite old with tanks experiencing few additions in the last 10-20 years. At Kyshtym the tanks' contents were

---

1. Reports on the accident previous to the Soviet Union's public admission in mid 1989 often refer to this accident as the 'Southern Urals accident'.

actively changed and overheating was a constant problem[4]. The accidents occurred less than one year following the last waste addition to the tank.

To clarify and prioritize safety concerns, four limiting safety conditions were defined and all tanks evaluated to determine if the tank contents exceeded these limits. This procedure generated four watch lists of tanks according the following quantifiable conditions: a high amount of ferrocyanides, a high concentration of organic salts, a high potential for accumulation of hydrogen gas, and a high heat generation rate[5]. These conditions, then, outline the major safety concerns for the Hanford wastes. Tank 241-C-106, the focus of this thesis, is listed under the last category with the greatest heat load among the Hanford tanks.

From the level data from this tank, investigators have inferred a steam region to likely exist at the bottom of the tank during the summer months[6]. The high heat load and this conclusion result in the greatest safety concern to be a 'steam bump' resulting in over-pressurization of the tank. The analysis concluding the existence of a steam region used a sludge thermal model which only included heat conduction. Inclusion of natural convection in the analysis is essential to determining the magnitude and likelihood of this steam region. This thesis presents analysis on both the potential for convection and the effect of a local convective region on the size of the predicted steam region.

1.2 Tank Information

1.2.1 Tank Data

Available data on Tank 241-C-106 come from two thermocouples trees (TC), TC-8 and TC-14, and a level sensor (see Figure 1.1). TC-14, located 15.5 ft from the tank center, has 4 thermocouples in the sludge and 8 thermocouples in the dome air space. TC-8, located 34 ft from the tank center, has 4 thermocouples in the sludge and 2 in the dome air space. Thermocouples on each tree are counted beginning with the lowest thermocouple, and increasing with height. Measurements are available for TC-14, TC-8, and the level sensor from 1982, 1983, and 1981, respectively. Daily measurements for these instruments are not recorded until 1991, 1992, and 1989, respectively (see Appendix A).
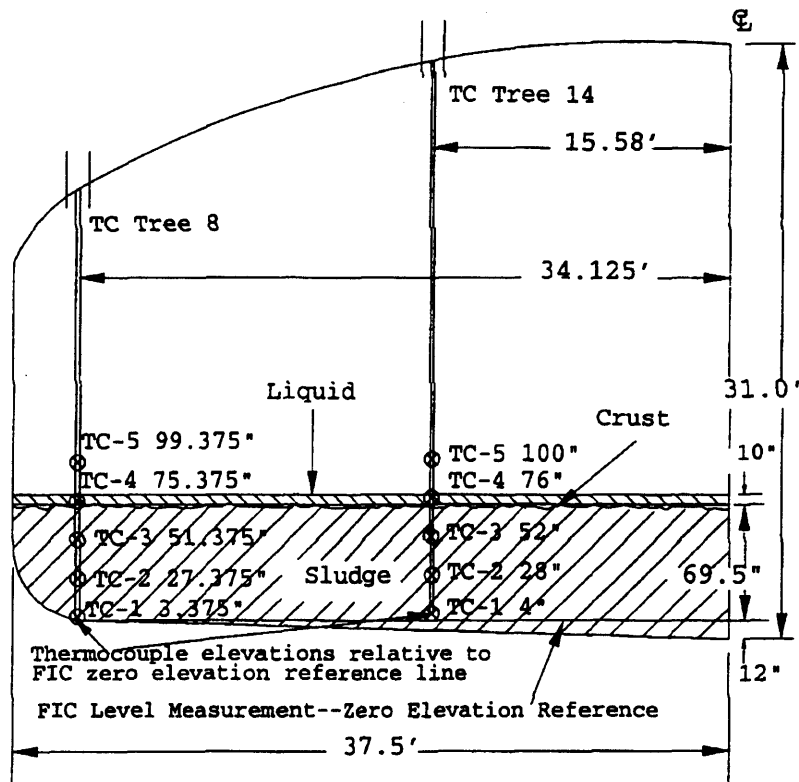
Figure 1.1: Tank 241-C-106 side view showing tank dimensions [6].

Three external conditions affecting the data are: normal operations, ventilation outages, and any Process Test. Normal operations consist of oscillations caused by diurnal and seasonal changes in temperature and humidity and approximately monthly additions of water, to compensate for water lost due to evaporative cooling. Accidental ventilation outages occurred in 1990 for a period of a month and 1992 for a period of 4.5 months (see Appendix A, Figure A.2). In a Process Test conducted in 1994, no additions of water to compensate evaporative cooling were made for three months. This allowed the normally existing water layer over the sludge to dryout exposing the top part of the sludge. Appendix A gives the level and temperature data reflecting the three external conditions described.

Three features of the data are unexplained. First, TC-14 measurements of temperature made closer to the tank center are lower at a similar elevation as compared to those on TC-8 (farther from the tank center). For a heat producing medium cooled externally this trend

is counter intuitive. Second, over the period of water additions, the temperature rises following water addition for TC-14 and drops over the second half of the period. Lastly, the level data indicates that the evaporation rate of the water is not constant over this period. The rate is approximately half of the average for the first 10-15 days and then increases (see Appendix A, Figure A.6).

1.2.2 Tank Characteristics

Contents of Tank 241-C-106 are products of three different sets of additions from processes generating waste between 1947 and 1979. The first set, made between 1947 and 1965, was from a bismuth and tributyl phosphate process which generated 'metal' waste. The second addition, from PUREX processing, consisted of a sludge supernatant with cesium and strontium as the primary heat producers and was added between 1970 and 1972. The high content of strontium in this layer is due to a failed decanting step of the PUREX sludge. The wash solution used in this step was pumped into Tank 241-C-106 with the strontium solids still suspended[7]. The third addition was strontium sludge from noncomplexed waste added between 1977 and 1979[8]. In earlier conduction studies [8,9,10], different thermal properties are associated with each of these layers. Later conduction studies and the analysis presented in this thesis consider only the internal heat generation distribution to be nonuniform, thereby simplifying the analysis.

Figure 1.1 shows dimensions of the single-shell Tank 241-C-106 sideview, indicating the dished bottom and thermocouple radial placements. Figure 1.2 shows the tank top view giving the circumferential position of TC-8 and TC-14. Finally, Figure 1.3 shows the tank position relative to the ground water below and the ground level above. The radial distanceindicatedishalfofthemeandistancetoadjacenttankcenters.

No.	Dia.	Elev.	Description and Comments
1	4"	646.15	FIC, BM
2	12"	646.18	Exhauster Riser
3	12"	647.24	Lead Covered WC
4	4"		Recirculating Dip Leg WC
5	4"		Recirculating Dip Leg WC
6	12"	646.01	Sluicing Access/Flange
7	12"	646.46	OBSV Port/Press. Gauge
8	4"	645.86	B-221 Temperature Probe
9	42"		Sludge Pump
13	26"		Distributer Jet WC
14	4"	645.5	Temperature Probe
15	12"		Air Inlet Filter
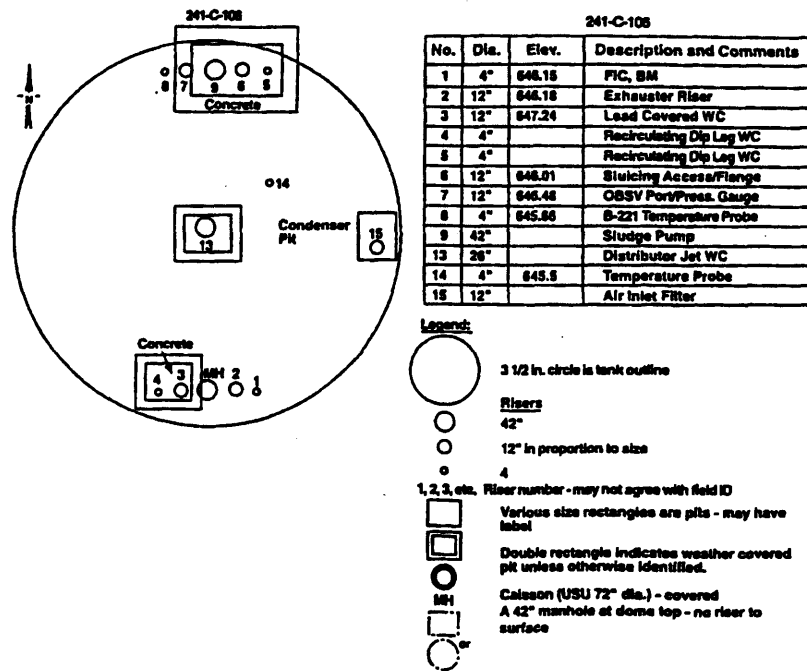
Figure 1.2: Tank 241-C-106 top view of instrument and thermocouple positions [7].
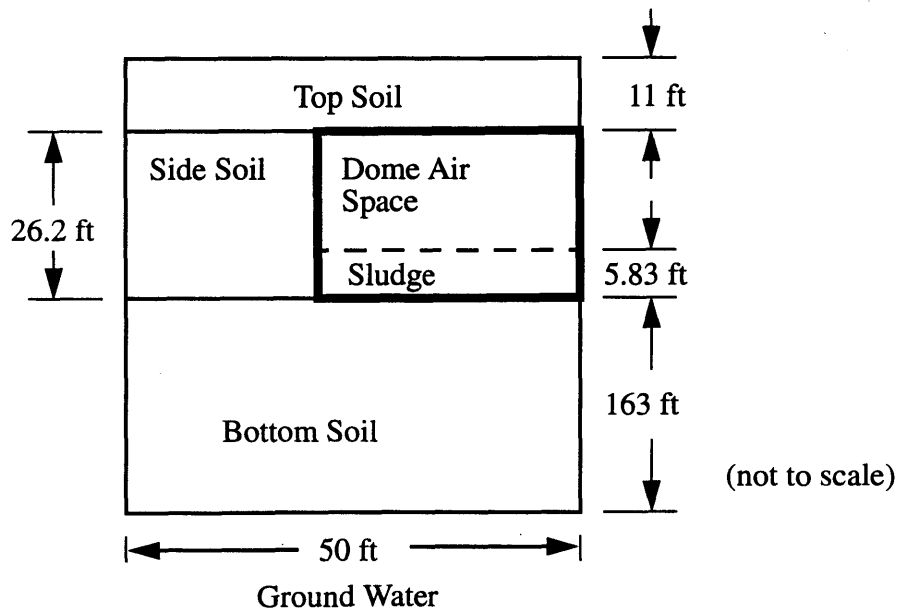
Figure 1.3: Tank 241-C-106 ground placement relative to ground water and ground surface.

1.3 Previous Thermal Analysis on Tank 241-C-106

1.3.1 Conduction Modeling

All previous thermal analyses of Tank 241-C-106 modeled only conductive heat transfer in the sludge. Bander's conductivity analysis showed the effect of varying internal heat generation and thermal conductivity both axially according to the characteristics of the aforementioned levels and radially segmenting the tank into an outer and an inner ring[8]. In the analysis, Bander attempted to match calculated temperatures at the locations of both TC-8 and TC-14 with those measured. The final result did not match the profile and over predicted temperatures by 20-70°F. In a separate analysis on the effects of ventilation flow rate and dryout of the waste, Bander found a maximum temperature of 236°F with nonuniform heat generation, under existing conditions of waste water content and ventilation flow rate[9]. The depth of waste used, however, was larger than that accepted as correct by current analyses [6,7]. Knowing the maximum temperature difference to be roughly proportional to the depth squared and using a more current thermal conductivity estimate, one finds that if Bander had used the depth of more recent analyses, the maximum temperature would be closer to 225°F. This result is significant in that the saturation temperature would be near 228°F at the bottom of the tank, when accounting for pressure head and salt content [6]. Bander's result then, would be that no steam region exists.

Reid and Eyler varied the thermal conductivity for the three layers of sludge in a 1-D model that matched calculated temperatures to measured TC-8 temperatures[10]. The thermal conductivity in the layers varied from 0.5 to 1.5 Btu/hr/ft/°F for matching the profiles. The thermal conductivity used for the following analysis is near 0.6 Btu/hr/ft/°F as was used for more recent analyses [6,7]. Reid and Eyler used a higher heat generation rate and a larger sludge depth, however. Adjusting these values to those used in the following analysis generates a thermal conductivity needed to match temperatures calculated to measured ranging from 0.35 - 1.05 Btu/hr/ft/°F. The midpoint for this range, 0.7 Btu/hr/ft/°F, is higher than that used for the recent analyses. In the presence of

convection heat transfer this calculated conductivity would be an effective conductivity and be expected to be larger than the actual conductivity.

More recently Thurgood and Bander issued reports again modeling the sludge with only conduction[6,7]. The tank properties used and results are discussed in Chapter 3. Unlike previous analyses, these reports concentrated on level data from both the Process Test and normal operations using a uniform thermal conductivity and a nonuniform internal heat generation. From the level data trends [11] and conduction model temperatures, both authors conclude that a steam region exists at the bottom of the tank during the summer months.

1.3.2 Convection Modeling

Two papers analyzed the potential for convection within the tank. Thurgood et al. discuss localized convection in the form of a hypothesized annulus existing around TC-14 [6]. They found that an annulus width of 1/16 of an inch, with an assumed convective heat transfer coefficient in the annulus, gave temperatures that match TC-14 while keeping the surrounding sludge at temperatures near that generated from pure conduction models without an annulus. The affected zone for the annulus was assumed to be 6 feet. Chapter 3 gives a more detailed description of this analysis and its characterization of the annulus.

McGrail et al. analyzed convection throughout the porous sludge in determining the potential for the transport of ^{137}Cs to a localized area [12]. To simplify the analysis the porosity was assumed isotropic. The analysis was done for a tank other than 241-C-106 in which the ferrocyanide concentration was high. Using TEMPEST, a thermal hydraulics code, McGrail et al. modeled a saturated porous region with uniform internal heat generation and no temperature difference between the top and bottom boundaries for a range of Darcy numbers defined as,

$$Da = \frac{P}{L^2},$$ (1.1)

where L is the characteristic length of the region and P is permeability defined as,

$$P = \frac{D_p^2 \varepsilon^3}{175(1-\varepsilon)^2}, \qquad (1.2)$$

where D_P is the particle diameter, and ε is the porosity. This permeability relates velocity to pressure drop in a porous medium, which for low flow velocities is given as:

$$u = \frac{P\Delta p}{\upsilon_f \rho_f L}, \qquad (1.3)$$

where the temperature dependence of properties has been neglected for the medium. McGrail et al. calculated the effect of convection on the temperature profile for a range of permeabilities, region depths, internal heat generation rates and thermal conductivities. A non dimensionalization of these temperature profiles as

$$T^\circ = \frac{T}{\frac{q''L^2}{k}} \qquad (1.4)$$

and a rough extrapolation of the presented data shows the potential to change temperatures in the upper half of the tank by 2°F for a permeability of $1*10^{-13}$ and by 10°F for a permeability of $3.0*10^{-10}$. Figure shows the trends presented by McGrail et. al, and in which Table 1.1 compares their model properties against those estimated to exist for Tank 241-C-106.

	Figure Properties McGrail et. al. [12]	Tank 241-C-106 Properties [7,6]
Volumetric Heat Generation (Btu/hr/ft^3)	2.59	4.04
Thermal Conductivity (Btu/hr/ft/°F)	1.33	0.59
Porous Medium Height (ft)	36.1	5.83

Table 1.1: Model Properties Used for Figure and Tank 241-C-106
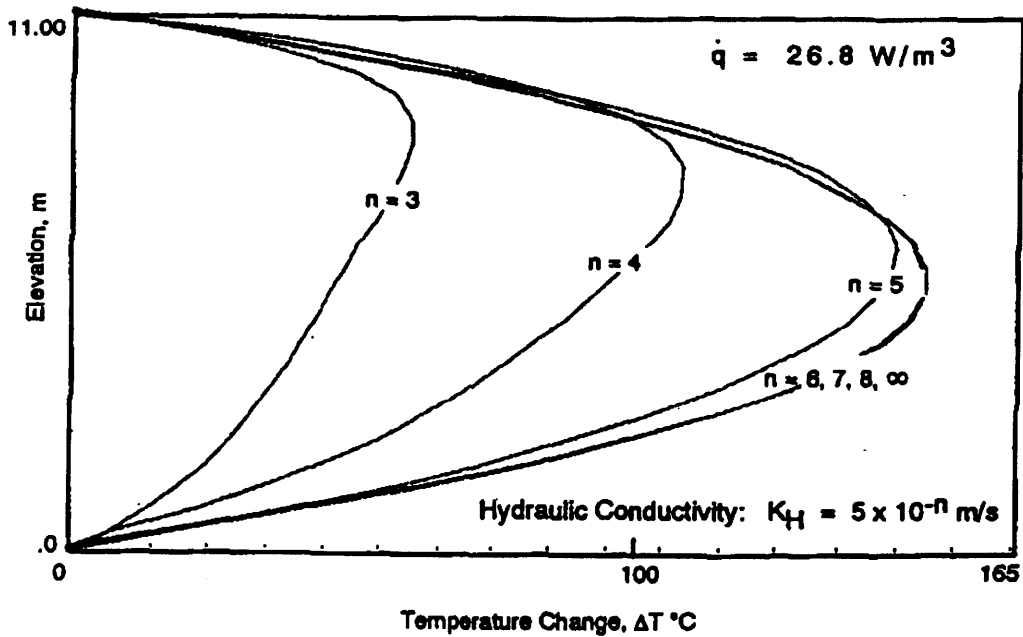
Figure 1.4: Temperature contours in sludge with varying hydraulic conductivity [12].

Note that the graph uses metric units and plots the effect of hydraulic conductivity. The numbers given above have been converted knowing the definition of permeability (equation 1.3) and hydraulic conductivity:

$$u = \frac{K_H \Delta p}{g \rho_f L},$$
(1.5)

resulting in,

$$P = \frac{K_H \nu_f}{g}.$$
(1.6)

The expected range of permeabilities for Tank 241-C-106 is $3.2*10^{-10}$ and $2.6*10^{-14}$ as taken from Piepho [13]. The best estimate conduction model of Thurgood's paper overpredicts the temperatures at TC-8 by 8°F near the bottom of the tank, 28°F near the midpoint, and 20°F in the upper region of the tank[6]. Comparison to Figure shows these differences to fit the trend of convection, though the differences are larger than those roughly extrapolated from data of McGrail et al.. Convection in the tank then can

26

potentially explain the profile at TC-8. In addition, differences exist between Tank 241-C-106 and the model of McGrail et al. In Tank 241-C-106, there exists a temperature decrease from the bottom to the top and an overlying liquid layer above the saturated porous region. Both characteristics would increase convection.

Chapter 2

Analytical Studies on the Onset of Convection

The first step in determining the effects of convection analysis on understanding the phenomena within the high heat flux tanks is quantifying the conditions which allow convection. Three models are considered here for the onset of convection: an internally heated porous medium, an internally heated porous medium overlayed with a region of fluid, and an unheated porous medium having a solute gradient. In all cases the porous region is saturated.

2.1 Onset of Convection in a Porous Layer

The most basic model of an internally heated, porous medium was studied by Gasser and Kazimi [14]and compared well with experiments of Buretta [15], Sun [16], and Hwang [17]. The following Sections 2.1.1 and 2.1.2 summarize the approach used by Gasser and Kazimi[14].

2.1.1 Analytical Description

Beginning with the equations for mass, momentum, and energy,

$$\frac{D\rho}{Dt} + \rho \nabla \bullet \vec{v} = 0 , \tag{2.1}$$

$$\rho \frac{D\vec{v}}{Dt} = (0, 0, \rho g) - \nabla p - \frac{\mu}{P}\vec{v} + \mu \nabla^2 \vec{v} , \tag{2.2}$$

$$\rho C_p \frac{DT}{Dt} = k_m \nabla^2 T + Q_v , \tag{2.3}$$

where

$$k_m = \varepsilon k_f + (1 - \varepsilon) k_s , \tag{2.4}$$

three assumptions are made. In the Boussinesq assumption, the temperature dependence

29

of density is included only as a buoyancy term in the momentum equation. The second assumption is the approximation of form resistance due to the porous matrix with Darcy's equation in which the pressure gradient is proportional to velocity and the ratio of viscosity to permeability,

$$\nabla p = -\frac{\mu}{P}\vec{v}.$$ (2.5)

Various equations for permeability exist attempting to match pressure drop with characteristics of the porous medium. This analysis uses the equation determined from the Ergun correlation [18]

$$P = \frac{D_p^2 \varepsilon^3}{175(1-\varepsilon)^2}$$ (2.6)

where D_p is the particle diameter and ε is the porosity. Lastly, a single energy equation is used for the solid and fluid in the porous region. This assumption, minimal local differences in temperature exist between the solid and fluid phases for small transients and steady-state, was confirmed experimentally by Wong and Dybbs [19]. Figure 2.1 shows the geometric model which these equations describe.
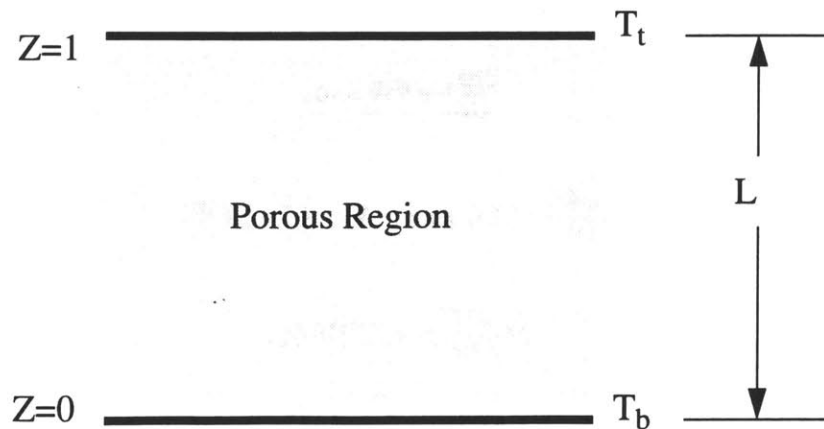
Figure 2.1: Porous medium configuration.

30

At the onset of convection these equations may be solved for the steady-state (d/dt=0), conduction (v=0) solution. This solution gives the pressure, temperature, and velocity distributions as a function of height. With this solution one applies linearized stability theory assuming a disturbance of the form,

$$g = e^{\sigma t} \cdot f(x, y) \cdot G(Z) \tag{2.7}$$

The real part of σ is assumed   negative so that the disturbance reaches a stable steady-state. Physically, the disturbance is advecting heat and momentum altering its own form and the distribution of energy to reach a finite equilibrium. Note also that the disturbance is assumed separable between the vertical and horizontal directions.

This form of the disturbance allows the following relations to be used in the balance equations:

$$T = T_o + T' \tag{2.8}$$

$$\vec{v} = \vec{v}_o + u\vec{i} + v\vec{j} + w\vec{k}, \tag{2.9}$$

$$p = p_o + p', \tag{2.10}$$

where p_o, T_o, and v_o are the conduction profiles and θ, u, v, w, and p' the finite disturbances. The resulting steady-state balance equations in which second order terms are neglected follow as

$$\frac{\partial u}{\partial x} + \frac{\partial v}{\partial y} + \frac{\partial w}{\partial z} = 0, \tag{2.11}$$

$$(0, 0, g\beta T') - \frac{1}{\rho}\left(\frac{\partial}{\partial x}, \frac{\partial}{\partial y}, \frac{\partial}{\partial z}\right)p - \frac{\nu}{P}(u, v, w) + \nu\nabla^2(u, v, w) = 0, \tag{2.12}$$

$$(\rho C_p)_f\left(u\frac{\partial T}{\partial x} + v\frac{\partial T}{\partial y} + w\frac{\partial T}{\partial z}\right) = k_m\nabla^2 T'. \tag{2.13}$$

By eliminating the pressure, applying continuity, and nondimensionalizing length, temperature, velocity and pressure, two nondimensionalized equations for momentum and

energy in the vertical direction result

$$\left(D^2 - a^2 - \frac{L^2}{P}\right)(D^2 - a^2)\, W(Z) = a^2 \Theta(Z) ,$$ (2.14)

$$(D^2 - a^2)\, \Theta(Z) = \left[\gamma R_I \left(\frac{1}{2} - Z\right) - \gamma R_E\right] W(Z) ,$$ (2.15)

in which

$$\Theta = \frac{T'}{T_b - T_t} ,$$ (2.16)

$$Z = \frac{z}{L} , \text{and}$$ (2.17)

$$W = \frac{w}{\left(\dfrac{g\beta\,(T_b - T_t)\,L^2}{\nu_f}\right)}$$ (2.18)

have been used as dimensionless parameters. In these equations, a is the horizontal wave number replacing the horizontal Laplacian of temperature and velocity. The D is a the derivative operator with respect to the dimensionless height, Z. . The internal Rayleigh number, R_I, is defined as

$$R_I = \frac{g\beta Q_v L^5}{\nu_f \kappa_f k_m} .$$ (2.19)

The external Rayleigh number, R_E, is defined as

$$R_E = \frac{g\beta \Delta T L^3}{\nu_f \kappa_f} .$$ (2.20)

2.1.2 Method of Solution

The boundary conditions used for a free surface above and a rigid surface below are as follows:

$$W(0) = DW(0) = 0 ,$$ (2.21)

$$W(1) = DW(1) = 0,$$ (2.22)

$$\Theta(0) = \Theta(1) = 0.$$ (2.23)

Velocity and temperature perturbation solutions are expanded in Fourier sine series matching the boundary conditions and solving the nondimensionalized momentum equation. The Galerkin method, first used on thermal convection problems by Veronis [20], is used in this analysis to determine the onset of convection. An advantage of the Galerkin method (over that used by Lapwood [21], e.g.) is that it determines not only the conditions for the critical mode of convection, but the n modes beyond, allowing the computation of heat transfer coefficients for Rayleigh numbers 50 to 100 times the critical value (see Section 2.4). In this approximation, the energy equation, incorporating the forms of velocity and temperature previously determined, is multiplied by sin(n*pi) where n equals the number of terms in the Fourier expansion and integrated from Z= 0 to 1. The resulting n*n matrix, denoted M, has unknowns Da $(=P/L^2)$, a, R_E, and R_I. The matrix is multiplied by the Fourier expansion coefficients, denoted A, and set equal to zero,

$$\overline{\overline{M}} \cdot \overline{A} = 0.$$ (2.24)

Solving this equation for nontrivial A implies

$$det\left(\overline{\overline{M}}\right) = 0.$$ (2.25)

The Darcy number is determined from the geometry being modelled. Setting R_E equal to zero, one can find the preferred wave number for the onset of convection as the lowest calculated value R_I $(dR_I/da=0)$. Plotting the values for various R_I and R_E, Gasser and Kazimi [14] found that if R_I and R_E are multiplied by $\gamma \cdot Da$ producing R_I',

$$R_I' = \frac{g\beta Q_v L^3 P}{\upsilon_f \kappa_f k_m} \cdot \frac{k_f}{k_m},$$ (2.26)

and R_E',

$$R_E' = \frac{g\beta \Delta TLP}{\upsilon_f \kappa_f} \cdot \frac{k_f}{k_m},$$ (2.27)

33

the curves are the same for any Darcy number.

Figure 2.2 shows the resulting curves from the above analysis used to determine if convection exists. For convective heat transfer to exist, the internal Rayleigh number (dependent on the volumetric heat generation rate) and the external Rayleigh number (dependent on the temperature difference between the bottom and the top boundaries) must exceed certain critical values. Two curves are plotted in Figure 2.2 each defining an envelope beyond which convection will occur due to the combined effect of external heat generation and boundary temperature differences. The lower curve is for destabilizing external temperature gradients with the lower temperature greater than the upper temperature. The higher curve is for stabilizing external temperature gradient in which the internal generation rate must compensate (increase) as stabilization of the external gradient increases.
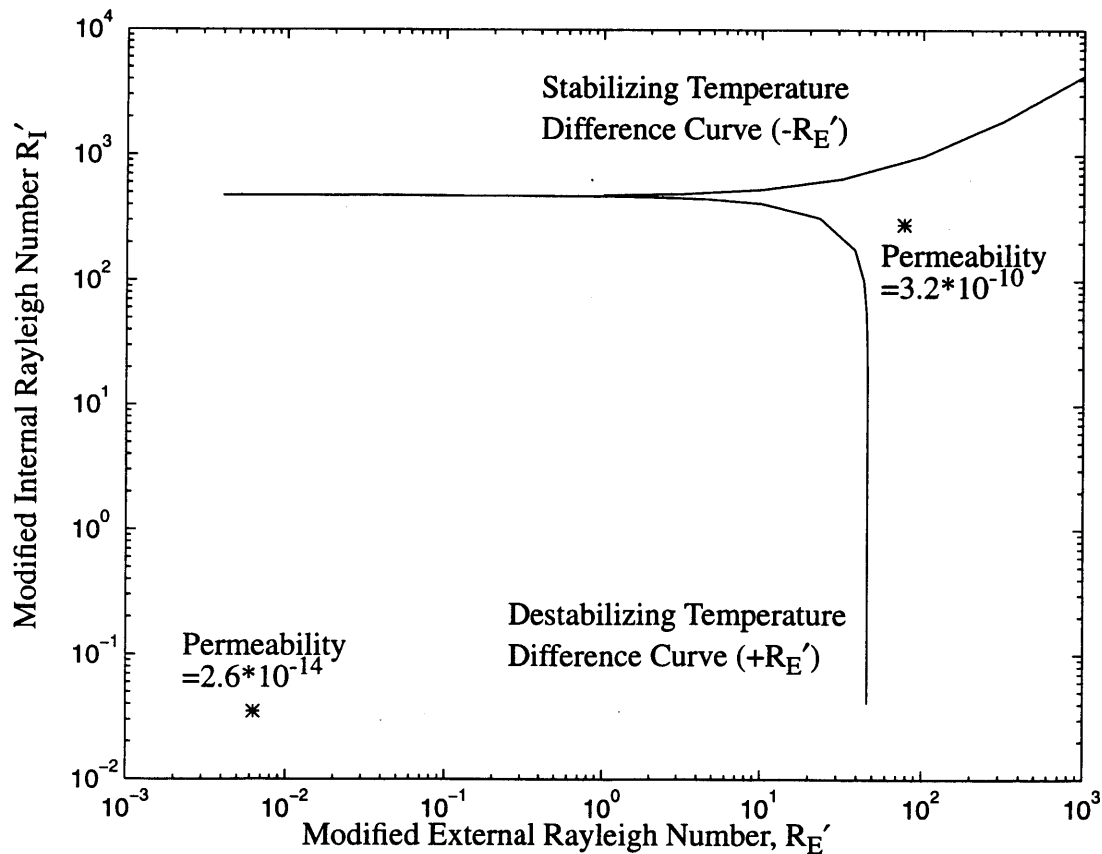
Figure 2.2: Critical internal Rayleigh number vs. external Rayleigh number for stabilizing and destabilizing temperature gradient

2.1.3 Application to High Heat Flux Tanks

For the high heat flux tank, Tank 241-C-106, values exist for temperature difference, heat generation, and fluid properties with the fluid assumed to be water. The geometry of the porous medium is known and the permeability range can be estimated from Piepho's anticipated sludge characteristics [13]. Therefore one may determine whether the combination of external and internal Rayleigh numbers for conditions in the tank exceeds critical values.

The temperature difference used in the calculations is that measured by TC-8 at the edge of the tank. As discussed in Chapter 4, TC-14 nearer the center of the tank is hypothesized to have a convecting annulus surrounding it so that the temperature measurements do not reflect the local sludge temperatures. It is expected that the temperature difference nearer the center of the tank is greater, because of the direction of the heat flow and the assumption of uniform heat generation throughout the tank. Thus, using the measured summer, external, destabilizing temperature difference of 65 °F (slightly lower than that measured during winter) yields a conservative estimate of $R_E[7]$.

Internal volumetric heat generation, 4.06 Btu/hr/ft^3, is based on an estimate of total heat generation from Bander's study of transient heating due to loss of cooling and the volume of the tank [22]. The height of the porous region is taken as that of the top of the sludge visualized during the process test to be 70 in above the bottom of the tank knuckle. This estimate neglects the effects of the material in the slightly dished tank bottom. This material, however, has been assumed to be hard pan and impervious to water flow [23].

This analysis uses a range of permeabilities proposed in a study by Piepho [13] on the potential drainage characteristics of the tank. Two calculations one based on low permeability of $2.6*10^{-14}$ ft^2 and one on a high permeability of $3.2*10^{-10}$ ft^2 are performed. These permeabilities correspond to a particle diameter (D_p) of $3.3*10^{-5}$ and $3.6*10^{-3}$ in, respectively, using a porosity of 0.52 (proposed by Thurgood) and equation 2.6 [6].

As Catton mentions, the best method of determination of the porous region conductivity (k_m) is measurement [24]. No accurate conductivity has been experimentally measured for the porous medium within the tank. However, Thurgood's modeling of the tank to dissipate energy only by conduction generated an effective thermal conductivity of 0.59 Btu/

hr/°F/ft [6]. Because this effective thermal conductivity is hypothesized to involve both convection and conduction the actual thermal conductivity may be lower for the composite particle bed. Choosing a thermal conductivity of 0.59 Btu/hr/°F/ft is conservative as it produces a lower estimate of both the internal and external Rayleigh numbers within the tanks. The saturating fluid is taken as water and the properties are evaluated at the mean of the upper and lower boundary temperatures. Table 2.1 summarizes these values.

Variable	Value	Units
Fluid Dynamic Viscosity, ν_f	5.4e-6	ft^2/s
Fluid Thermal Diffusivity, κ_f	1.7e-6	ft^2/s
Gravity, g	32.2	ft/s^2
Thermal Expansion Coefficient, β	2.8e-4	$°R^{-1}$
Fluid Thermal Conductivity, k_f	0.38	Btu/hr/ft/°F
Porous Medium Thermal Conductivity, k_m	0.59	Btu/hr/ft/°F
Porosity, ε	0.52	-

Table 2.1: Characteristic Tank Parameters

Table 2.2 summarizes the results of the calculations. For the low permeability estimate the conditions in the tank are below critical as the internal and the external Rayleigh numbers are graphically within the critical envelope (see Figure 2.2), so convection is not predicted to occur. For the high permeability estimate, the conditions are outside the critical envelope indicating the possibility of convection. These results are plotted in Figure 2.2.

	$P=2.6*10^{-14} ft^2$	$P=3.2*10^{-10} ft^2$
$R_I{}'$	$3.5*10^{-2}$	$2.8*10^2$
$R_E{}'$	$6.3*10^{-3}$	$7.7*10^1$
CONVECTION	NO	YES

Table 2.2: Computed Rayleigh Numbers For Porous Region

2.2 Onset of Convection in a Porous and Superposed Fluid Layer

Because of the large heat generation in the high heat flux Tank 241-C-106, the tank is cooled by a superposed layer of evaporating fluid replenished approximately monthly. Incorporating the effect of this water layer into the analysis, one can not solve the problem separately, that is matching boundary conditions after solving the fluid layer and porous layer for velocity and temperature, as Suo-Antilla and Catton [25] found in their work. The onset of convection in this model involves a coupling of velocity and temperature and the equations for both regions must be solved simultaneously. The work of Somerton and Catton [26,27] presents the procedure for determining the onset of convection for a fluid saturated porous medium superposed by a fluid layer.

2.2.1 Analytical Description

Figure 2.3 shows the general geometry of this model. Analogous to equations 2.1 to 2.3 for the porous region are the following for the fluid region

$$\frac{D\rho}{Dt} + \rho \nabla \cdot \vec{v} = 0, \tag{2.28}$$

$$\rho \frac{D\vec{v}}{Dt} = (0, 0, \rho g) - \nabla p + \mu \nabla^2 \vec{v}, \tag{2.29}$$

$$\rho C_p \frac{DT}{Dt} = k_f \nabla^2 T. \tag{2.30}$$

Nondimensionalizing as in Section 2.1.1, eliminating pressure, and applying the continuity equation results in momentum and energy equations for the fluid and porous regions denoted as

$$(D^2 - a^2)^2 W_1 = a^2 \Theta_1, \tag{2.31}$$

$$(D^2 - a^2) \Theta_1 = \frac{-W_1}{(\eta + \gamma)(\eta + 1)} \left[R_E (1 + \eta)^2 + \frac{1}{2} R_I \right], \tag{2.32}$$

$$(D^2 - a^2)^2 W_2 - \frac{1}{Da}(D^2 - a^2) W_2 = a^2\Theta_2, \tag{2.33}$$

$$(D^2 - a^2)\Theta_2 = -W_2\{\frac{1}{(\eta + \gamma)(\eta + 1)}\left[R_E(1 + \eta)^2 + \frac{1}{2}R_I\right] + Z\gamma R_I\}, \tag{2.34}$$

where γ is the ratio of fluid to porous region thermal conductivity, η is the ratio of fluid height to porous region height, and Da is the Darcy number, P/L^2. The equations for the fluid region are similar to those of the porous region except that the lack of form resistance is reflected in not having a Darcy term in the momentum equation and the lack of internal energy generation removes the z dependence in the convection term of the energy equation.
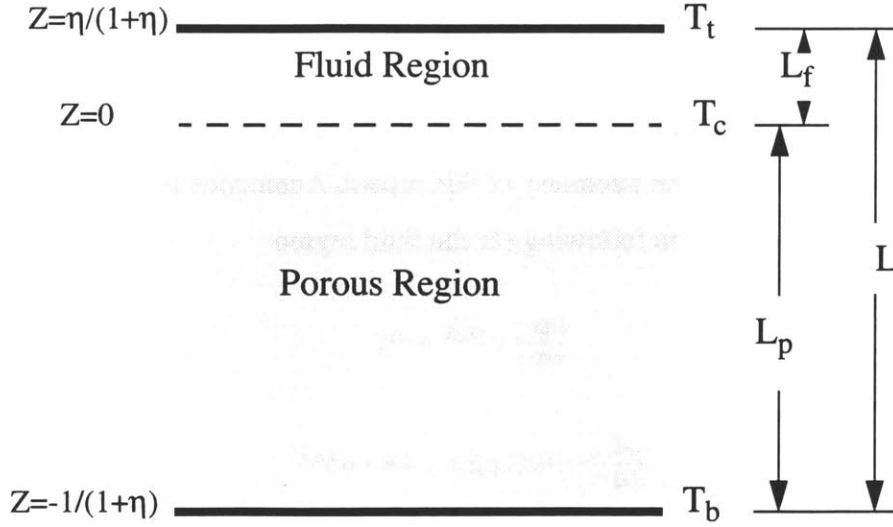
Figure 2.3: Porous layer superposed by a fluid layer diagram

The upper and lower boundaries are held at constant temperature and are rigid such that at the edges vertical and horizontal velocities are zero, denoted as

$$W\left(\frac{\eta}{\eta + 1}\right) = DW\left(\frac{\eta}{\eta + 1}\right) = \Theta\left(\frac{\eta}{\eta + 1}\right) = 0, \tag{2.35}$$

$$W\left(\frac{-1}{\eta+1}\right) = DW\left(\frac{-1}{\eta+1}\right) = \Theta\left(\frac{-1}{\eta+1}\right) = 0. \tag{2.36}$$

Note that as a two dimensional problem the equation of continuity for an incompressible fluid equates radial velocity with a change in vertical velocity.

Across the interface between the fluid and porous regions vertical velocity, horizontal velocity, horizontal shear stress, and pressure are equal. A significant assumption in the analysis involves the equivalence of shear stress at the interface, z=0:

$$\mu\frac{\partial u_1}{\partial z} = \mu'\frac{\partial u_2}{\partial z}, \tag{2.37}$$

$$\mu\frac{\partial v_1}{\partial z} = \mu'\frac{\partial v_2}{\partial z}. \tag{2.38}$$

Elaborate models exist for quantifying μ', the effective viscosity in the porous region. Neale and Nadar [28], however, have shown that setting $\mu'=\mu$ fits experimental data well in that the actual value used has little effect on the final analytical result so this equivalence is used in this analysis. The resulting coupling equations for velocity are

$$W_1(0) = W_2(0), \tag{2.39}$$

$$DW_1(0) = DW_2(0), \tag{2.40}$$

$$D^2W_1(0) = D^2W_2(0), \tag{2.41}$$

$$(D^2 - a^2)DW_1 = (D^2 - a^2)DW_2 - \frac{1}{Da}DW_2. \tag{2.42}$$

In addition temperature and heat flux are continuous across the interface resulting in coupling conditions

$$\Theta_1(0) = \Theta_2(0), \tag{2.43}$$

$$\gamma D\Theta_1(0) = D\Theta_2(0). \tag{2.44}$$

2.2.2 Method of Solution

As in the previous analysis, the Galerkin method is used to find the onset of convection. The resulting combinations of critical Rayleigh numbers, however, do not reduce to a single graph. The combination of γ, η, and Da result in a minimized internal Rayleigh number with respect to wave number for a chosen external Rayleigh number. The wave number corresponding to this minimized internal Rayleigh number is independent of the chosen external Rayleigh number. This implies a relationship between external and internal Rayleigh numbers which depends on γ, η, and Da only. Somerton and Catton [26,27] found this universal Rayleigh number to be

$$R_{E,U} = \frac{\eta^4}{(1+\eta)^5(\gamma+\eta)}\left[R_E(1+\eta)^2 + \frac{1}{2}R_I\right] \qquad (2.45)$$

Therefore the numerical procedure must be applied for each combination of γ, η, and Da. Though the theory presented by Somerton and Catton [26,27] is correct the numerical calculations presented are incorrect and should not be used for validation of further numerical results (see Appendix A).

2.2.3 Application to High Heat Flux Tanks

Applying the numerical procedure associated with the Galerkin method resulted in calculations exceeding computer capabilities for low Darcy numbers (such as those found in the high heat flux tanks). Appendix B summarizes the manipulations of calculations within the Galerkin method used for solving the velocity and temperature profiles for low Darcy numbers.

The liquid level normally varies from 5 to 9 inches above 70 inches of the porous medium so that η varies from 0.07 to 0.13 [4]. Other values used are explained in Section 2.1.3. Tables 2.3 and 2.4 outline the critical Rayleigh numbers for low and high permeability and two different liquid levels.

With the fluid layer, the onset of convection takes place at much lower external and internal Rayleigh numbers. This onset is dominated by the fluid layer for low Da numbers and will begin convecting at much lower Rayleigh numbers, because no form resistance exists in the fluid layer. Because of the continuity of velocity from fluid to porous layers,

	$P=2.6*10^{-14}$	$P=3.2*10^{-10}$
R_I	$6.4*10^{13}$	$6.4*10^{13}$
R_E	$1.6*10^{13}$	$1.6*10^{13}$
R_U	$1.2*10^9$	$1.2*10^9$
$R_{E,cr}$	$6.0*10^7$	$6.0*10^7$
$R_{I,cr}$	0	0
$R_{U,cr}$	$1.4*10^3$	$1.4*10^3$
CONVECTION	YES	YES

Table 2.3: Critical and Tank Rayleigh Numbers (η=0.07)

	$P=2.6*10^{-14}$	$P=3.2*10^{-10}$
R_I	$8.3*10^{13}$	$8.3*10^{13}$
R_E	$1.8*10^{13}$	$1.8*10^{13}$
R_U	$1.3*10^{10}$	$1.3*10^{10}$
$R_{I,cr}$	$7.4*10^6$	$7.4*10^6$
$R_{E,cr}$	0	0
$R_{U,cr}$	$1.5*10^3$	$1.5*10^3$
CONVECTION	YES	YES

Table 2.4: Critical and Tank Rayleigh Numbers (η=0.13)

there is convection in the porous layer as well as indicated by profiles in Figures 2.4. Note that velocity perturbations are known to within a constant so that the x axis is valid only in quantifying relative perturbations within a single graph.

Figure 2.4 shows numerous convection cells within the porous layer. This characteristic follows the trend indicated in the literature [26,27], in which the number of cells increases with decreasing Darcy number and decreasing fluid height ratio, η. The strength of the velocity in the porous region relative to the fluid region is much higher for the higher permeability case as expected. In addition, the increase in fluid ratio degrades the
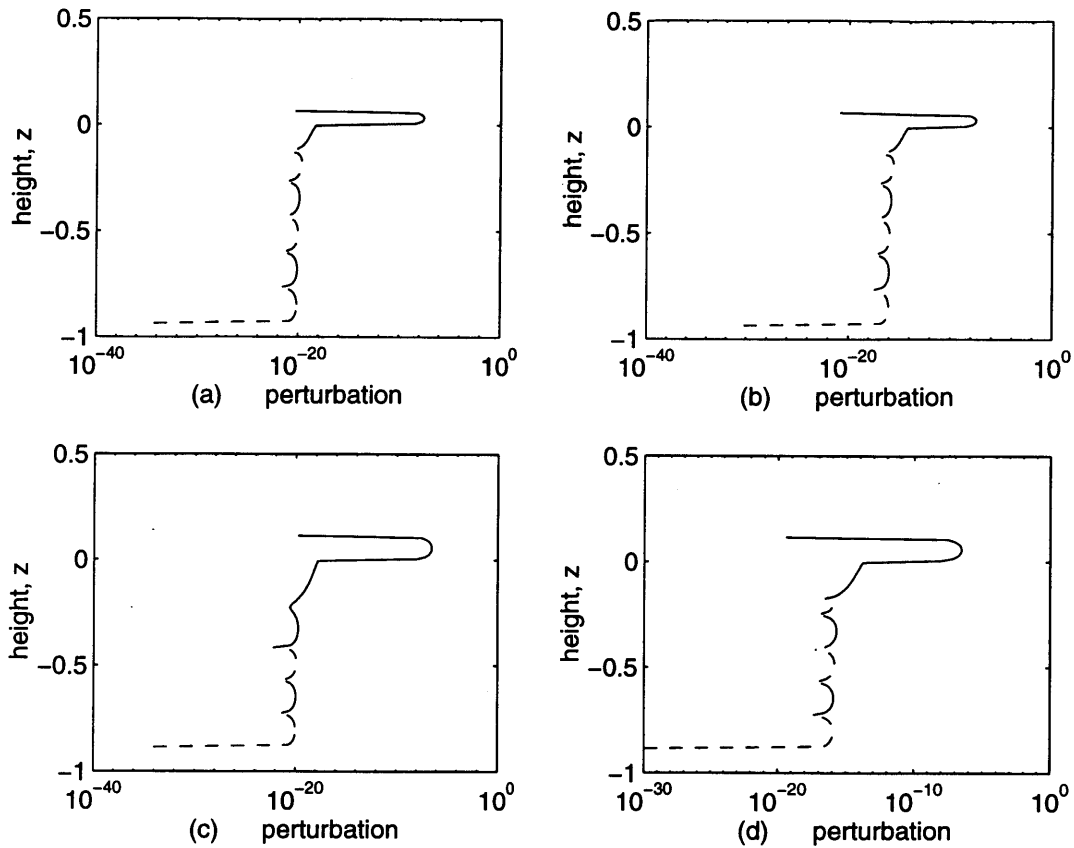
Figure 2.4: Velocity perturbation profiles vs. nondimensionalized height: (a) $P=2.6*10^{-14}$, $\eta=0.07$; (b) $P=3.2*10^{-10}$, $\eta=0.07$; (c) $P=2.6*10^{-14}$, $\eta=0.13$; (d) $P=3.2*10^{-10}$, $\eta=0.13$. (Negative perturbations are shown as dashed lines.)

multiple convection cell characteristics. Figure 2.5 shows the corresponding temperature profile for case (a). The cell pattern matches that of velocity but the difference of temperature fluctuations between the porous and fluid layers is much less than that of velocity because of the relative magnitude of the thermal resistance as indicated by γ.

2.3 Porous Medium Having a Solute Gradient

The previous two analyses have not incorporated the effect of a possible solute gradient in the tank. This third analysis quantifies the effect of the solute gradient and the

42
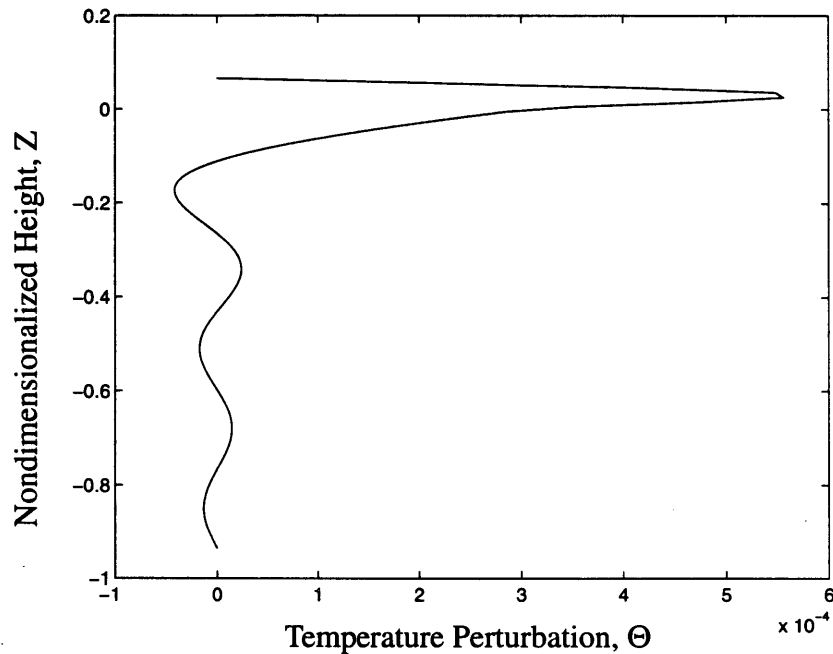
Figure 2.5: Characteristic temperature perturbation for $P=2.6*10^{-14}$ and $\eta=0.07$.

temperature gradient due to boundary temperature differences and qualitatively discusses the effects of internal heat generation and the overlying fluid layer based on physical arguments and trends in analytical studies.

2.3.1 Assumptions

The average solute concentration within Tank 241-C-106 has been estimated by Agnew as 34 wt% [29]. Information on the only core sample taken (in 1976) was not reported as a function of depth but as a lumped average value. Data on the potential solute gradient then does not exist. Plans to sample the core in recent years have been halted because present thermal analyses of the tank indicate the presence of a steam zone [6].

Because the water added as a cooling upper layer is steam condensate and relatively pure, the average concentration change from bottom to top of the tank must be at least 34 wt%. This solute gradient is stabilizing as concentration decrease from bottom to top causes density decrease from bottom to top. Because the temperature decreases (the majority of the heat is rejected up) from bottom to top, considering only temperature dif-

ferences across the tank yields a close approximation to the onset of convection. The study of Gasser and Kazimi [14] shows this approximation to be conservative in that considering internal heat generation will induce convection at a lower boundary temperature difference or higher stabilizing solute gradient. Further, the Gasser and Kazimi study shows that except for a small region, the external and internal Rayleigh numbers act independently, one changing criticality by much less than an order of magnitude over a wide range of the other (see Figure 2.2). Figure 2.6 shows a qualitative comparison of the temperature gradient assumed and that measured in the tank. Calculations of Section 2.1 show that the temperature difference is the major contributor to the onset of convection. Therefore neglecting the effects of internal generation will yield a close, conservative approximation to the actual onset of critical conditions found in Tank 241-C-106.
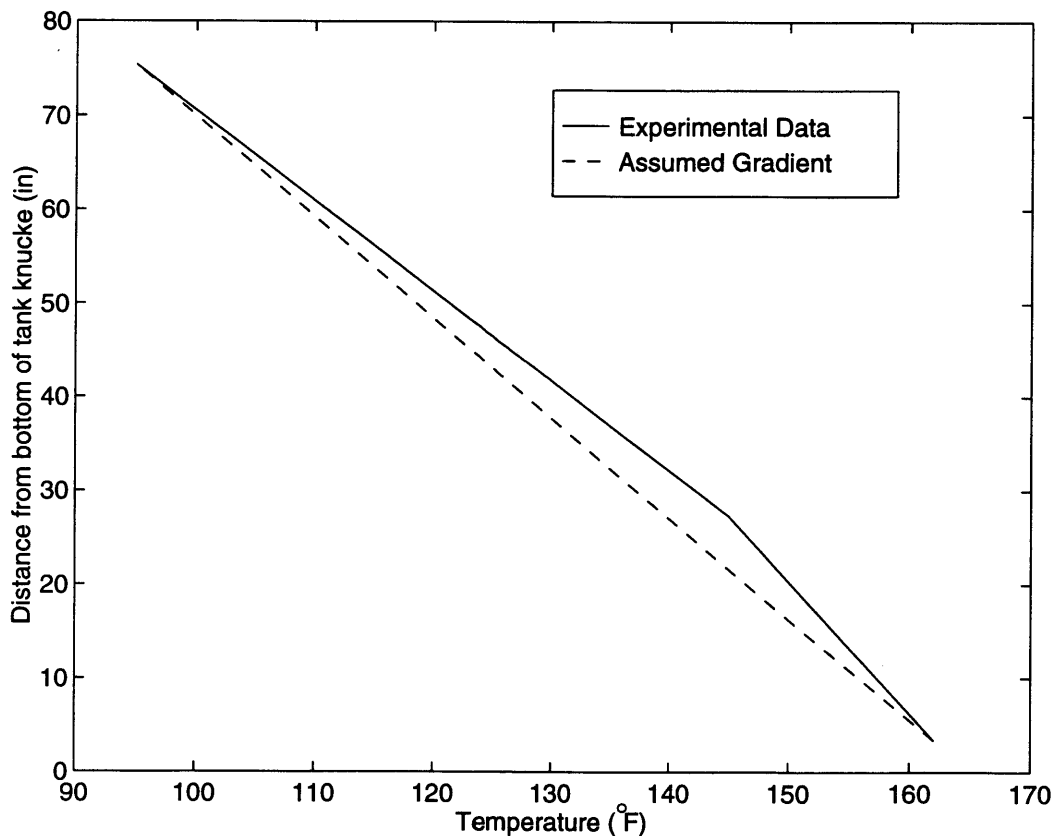
Figure 2.6: Measured temperature profile vs. assumed profile for Tank 241-C-106.

2.3.2 Method of Solution

Nield studied the onset of convection with linear temperature and solute gradients for a porous medium bounded by rigid walls [30]. This analysis uses the figures resulting from his work. He began with the following equations for mass, momentum, energy, and solute conservation

$$\frac{D\rho}{Dt} + \rho \nabla \bullet \vec{v} = 0 , \tag{2.46}$$

$$\rho \frac{D\vec{v}}{Dt} = (0, 0, \rho g) - \nabla p - \frac{\mu}{P}\vec{v} , \tag{2.47}$$

$$\rho C_p \frac{DT}{Dt} = k_m \nabla^2 T , \tag{2.48}$$

$$\varepsilon \frac{Ds}{Dt} = D_d \nabla^2 s , \tag{2.49}$$

where

$$\rho = \rho_o [1 - \beta (T - T_o) + \alpha (s - s_o)] , \tag{2.50}$$

$$\rho_o = \rho (T_o, s_o) , \tag{2.51}$$

and S is the solute concentration. Note that these equations neglect the internal resistance due to fluid viscosity for this porous region unlike those of the two previous analyses. As before, determination of the onset of convection is based on linear stability theory and the assumption of a small stable perturbation profile beyond the conduction solution. Nondi-mensionalization of the perturbed solution and application of the continuity equation results in the following steady-state perturbation equations

$$(D^2 - a^2) W = -a^2 R_E \Theta + a^2 R_S S , \tag{2.52}$$

$$D^2 \Theta - a^2 \Theta = W , \tag{2.53}$$

$$D^2 S - a^2 S = W , \tag{2.54}$$

where R_S is the solute Rayleigh number

$$R_S = \frac{-(g\alpha PL\Delta s)}{D_d{}^* v_f}, \tag{2.55}$$

where the effective molecular diffusivity in the porous region is experimentally correlated according to the porosity and a constant m determined experimentally

$$D_d{}^* = \frac{D_d}{\varepsilon^{1-m}}. \tag{2.56}$$

In this analysis m is taken as 1.4 [31]. Because no fluid layer overlies the porous layer, Figure 2.1 shows the geometry. These equations are solved with boundary conditions

$$W(0) = S(0) = \Theta(0) = 0, \tag{2.57}$$

$$W(1) = S(1) = \Theta(1) = 0, \tag{2.58}$$

and the expansion of the solutions of θ, W, and S in Fourier series.

Nield's results are shown in Figure 2.7 (note that R_S is positive to the left) in which the line XZ is given as

$$R_E + R_S = 4\pi^2, \tag{2.59}$$

and the line XW is given as

$$\left(\frac{Sc}{Sc+Pr}\right)R_E + \left(\frac{Pr}{Pr+Sc}\right)R_S = 4\pi^2. \tag{2.60}$$

The line of static stability PQ is

$$R_E + \frac{R_S}{\tau} = 0, \tag{2.61}$$

where $\tau = \kappa/D_d{}^*$.

The two lines shown in Figure 2.7 are a result of the physical difference in thermal and molecular diffusivities. Line XZ covers destabilizing concentration gradient and stabilizing temperature gradient in which infinitesimal fluid motion is monotonic. If a fluid parcel loses heat and drops a less concentrated parcel will replace the initial parcel because of the slow response of molecular diffusion. However, if a concentration gradient is stabilizing and the temperature gradient is destabilizing, a fluid parcel which gains density due to dif

46
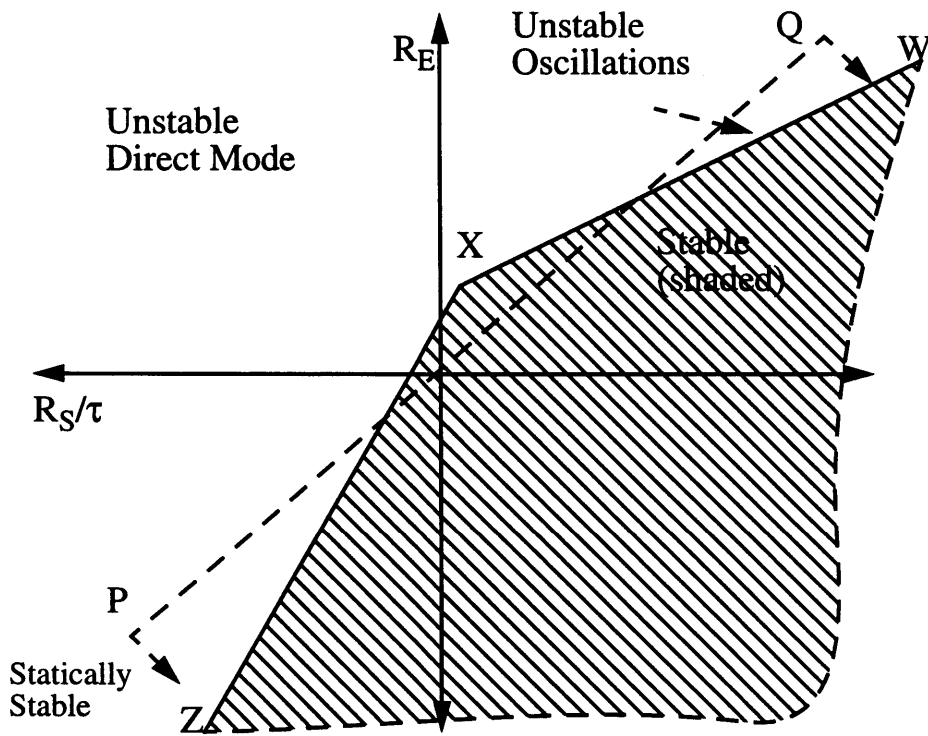
Figure 2.7: Stability regions for combined thermal and solute gradients[30]

fusive flux will drop, but due to the quickness of thermal diffusion the same parcel will heat and experience oscillation. Line XW defines critical conditions for oscillatory instability. Note that line PQ indicating the points of zero density gradient is not sufficient to define these critical conditions.

2.3.3 Application to the High Heat Flux Tank

The lower permeability Rayleigh number is below the critical Rayleigh number based on external temperature gradient. Adding a stabilizing concentration gradient amplifies this effect. Calculations then will only be done for the higher permeability case. Literature provided D_d as $1.77*10^{-8}$ ft^2/s [32] and α as $9.7*10^{-3}$ wt%$^{-1}$ [33]. Computing the R_S for the higher permeability case yields using these values gives

$$R_S = 1.2 \cdot 10^5.$$

Computing R_E yields

$$R_E = 1.2 \cdot 10^2.$$

These values can be plotted or used in equation 2.60 for which the left side yields $-8.5*10^2$ which is less that $4\pi^2$ so that the value is in the shaded region of Figure 2.7 and convection initiation has not been reached. Thus, for both low and high permeability cases, the combination of destabilizing temperature gradient and potential stabilizing concentration gradient results in a condition below that of critical.

It is hypothesized, however, that like the cases studied with internal and external Rayleigh numbers, the presence of an overlying fluid greatly reduces the critical Rayleigh number. I found a single study written by Chen and Chen [34], which considered both effects of a solute gradient and an overlying fluid layer. Their results corroborate this hypothesis. Chen and Chen produce calculations based of a destabilizing solute gradient and stabilizing temperature gradient. Beyond a low depth ratio, critical Rayleigh numbers are on the order of that which would exist for a pure fluid layer. Their results, further, show transition between porous and fluid region dominated convection near $\eta = 0.1$ which is in the range found in the tank (0.07-0.13). Chen and Chen repeating previous calculations with only an external temperature difference found a bimodal stability curve overlooked by previous investigators. This bimodal nature was also found when the solute concentration was included and thought to be the source of this transition of convection dominance from porous to fluid region with increasing η. This transition then indicates that for the higher permeability the liquid level change in the tank may cause fluctuations in the existence or strength of convection within the tank. Because the previous analysis of Section 2.2 showed that the fluid layer dominated the onset of convection regardless of the conditions in the porous region and this dominance was noted in the calculations done in the Chen and Chen analysis, the critical Rayleigh number for the conditions in the high heat flux Tank 241-C-106 is assumed to be below that computed for the tank due to the presence of the temperature difference across the fluid layer.

2.4 Quantification of Heat Transfer Beyond Onset of Convection

The previous sections looked only at the Rayleigh number at the onset of convection. This section outlines the theory quantifying heat transfer beyond the onset of convection and applies the analysis to conditions within the tank. Because the magnitude of solute gradient is unknown within the tank and the fluid layer is assumed to cause convection despite the solute gradient, quantification of heat transfer will not be based on the presence of a solute gradient. The presented analysis models the effects of temperature differences at the boundary, internal heat generation, and the overlying liquid layer on convection in the porous medium. The method, however, is only valid for near critical Rayleigh numbers as found in the analysis of Section 2.1. Therefore the calculations presented neglect the effect of the overlying fluid layer as Section 2.1 does.

2.4.1 Analytical Description and Solution

The methods outlined below are derived from the work by Catton [24]. In this work Catton used results of the work of Somerton and Catton[26,27], the generated nondimensionalized profiles of velocity and temperature. The method first applied to convection problems by Malkus and Veronis [35] is a power integral solution where velocity and temperature perturbations are volumetrically averaged. The Stuart assumption, that profiles of velocity and temperature do not change for Rayleigh numbers 50 to 100 times critical, is used in these averages[36].

Using the energy equation to find the heat flux due to both convection and conduction, one can define the Nusselt number as the ratio of total heat flux to that due to conduction. Again this method depends on the assumption of stability beyond onset of convection to eliminate the time dependent terms. The resulting Nusselt number is based on the 2n solutions of the 2n*2n matrix M found in an equation similar to equation 2.24 which involves a Fourier expansion of n terms for each region of the tank.

The Nusselt number is denoted as

$$Nu = 1 + \sum_n N_n \left(1 - \frac{Ra_{cr,n}^*}{Ra^*} \right) U\left(Ra^* - Ra_{cr,n}^* \right) \qquad (2.62)$$

where

$$Ra^* = R_E(1+\eta)^2 + R_I, \tag{2.63}$$

$$Ra_{cr}^* = R_{E,cr}(1+\eta)^2 + R_{I,cr}, \tag{2.64}$$

$$U(Ra^* - Ra_{cr,n}^*) \text{ is a step function,} \tag{2.65}$$

$$N_n = \frac{N_{2,n}F_{2,n}(1+N_{1,n})(\gamma+\eta) + \eta(1+N_{2,n})N_{1,n} + \gamma(1+N_{1,n})N_{2,n}}{\gamma(1+N_{1,n}) + \eta(1+N_{2,n})}, \tag{2.66}$$

where

$$N_{1,n} = \left[\frac{\langle(\overline{W_{1,n}T_{1,n}})^2\rangle}{\langle(\overline{W_{1,n}T_{1,n}})\rangle^2} - 1\right]^{-1}, \tag{2.67}$$

$$N_{2,n} = \left[\frac{\langle(\overline{W_{2,n}T_{2,n}})^2\rangle}{\langle(\overline{W_{2,n}T_{2,n}})\rangle^2} - 1\right]^{-1}, \text{ and} \tag{2.68}$$

$$F_{2,n} = \frac{2(1+\eta)\langle\overline{ZW_{2,n}T_{2,n}}\rangle}{\langle\overline{W_{2,n}T_{2,n}}\rangle}. \tag{2.69}$$

Tables 2.3 and 2.4 show that including the effect of the liquid layer yields critical Rayleigh numbers more than 50 to 100 times less than those for conditions in the tank. For the high permeability case of Section 2.1, however, the tank Rayleigh number is near critical and the method applicable. Simplifying Equation 2.66 to neglect the fluid layer by setting $N_{1,n}$ and η to zero generates

$$N_n = \left[\frac{\langle(\overline{W_nT_n})^2\rangle}{\langle(\overline{W_nT_n})\rangle^2} - 1\right]^{-1}\left(\frac{2\langle\overline{ZW_nT_n}\rangle}{\langle\overline{W_nT_n}\rangle} + 1\right). \tag{2.70}$$

2.4.2 Application to Tank Conditions

Using equations 2.62 - 2.65 and 2.70, the higher permeability case results in Nusselt number

$$Nu = 1.82$$

50

with the first critical Rayleigh number $Ra_{cr,1}^*=40$ and $Ra^*=77$.

Further information can be derived from the temperature and velocity profiles. The profiles generated from the expansion coefficients give each solution to within a constant. Because this constant is the same for both velocity and temperature, a quantification of velocity can be found for a given temperature perturbation. For this analysis temperature is nondimensionalized with T_b-T_t and velocity is nondimensionalized with $g\beta(T_b-T_t)L^2/v_f$. At maximum temperature for both the fluid and porous regions, the ratio of temperature to velocity perturbations is shown in Table 2.5. The large ratios found for the fluid region are indicative of the proclivity towards convection in this region as compared to the porous region. Note also that the increase in η has a large effect in the fluid region while permeability, P, has a large effect in the porous region. Numbers computed for the porous region neglecting the effect of the overlying fluid layer are on the order of those shown in the porous column of the table.

	Porous Region Perturbation (ft/s/°F)	Fluid Region Perturbation (ft/s/°F)
P=2.6e-14, η=0.07	4.6e-11	3.3
P=3.2e-10, η=0.07	4.7e-7	3.3
P=2.6e-14, η=0.13	2.5e-11	10
P=3.2e-10, η=0.13	3.3e-7	12

Table 2.5: Ratio of Velocity to Temperature Perturbations

2.5 Summary

In summary of Chapter 2, 4 cases were studied for the onset of convection. These cases combined high and low permeability and a low range of fluid to porous region depth ratios(η). In the first analysis only the porous region was considered (η=0), for which the high permeability case allowed convection and the low permeability case did not. The second analysis included the fluid layer. In this analysis the permeability made little

difference as the fluid layer dominated the onset of convection allowing convection for all cases. The third analysis considered a porous region with a stabilizing solute gradient. The effect of the solute gradient was sufficient to depress the onset of convection for the high permeability case. Because of lack of data on the tank, the magnitude of the solute gradient is unknown and the estimate used may have been to conservative. The effect of the overlying fluid layer is assumed to make this issue moot in that literature shows the fluid layer to dominate the onset of convection as was found in the second analysis. Finally, the Nusselt number and ratio of velocity to temperature perturbations for cases that allowed convection was computed for comparison with results from future modeling of global convection in Tank 241-C-106.

Chapter 3

Convective Annulus Hypothesis and Characterization

3.1 Introduction

Speculation on the existence of thermal convection within Tank 241-C-106 is largely a result of the temperatures recorded near thermocouple tree 14 (TC-14), 15.6 feet from the tank center. These temperature readings at thermocouple position 1 (TCP-1), near the bottom of the tank, are lower by almost 100 °F from those predicted by an analysis modeling thermal conduction only. While some studies focused on the appropriate distributions of internal generation and sludge thermal conductivities needed to match temperature profiles [8, 10], more recent reports have attributed the lower temperatures to local convective effects [6]. (See Section 1.3.1 for a discussion of the former.) The following section begins by outlining the analysis in the more recent reports concerning the potential for convection around TC-14. Secondly, with the annulus assumed to be the sole path of convection, the annulus width is estimated and characterized by matching temperature profiles from numerical simulations with the recorded data.

3.2 Previous Convective Channel Analysis

3.2.1 Multiple Channel Analysis

Reference to convection as a mode of dissipative heat transfer through the porous sludge region was made by Agnew of Los Alamos National Labs in a series of letters to O'Dell and others of Westinghouse Hanford Company (WHC), detailing Agnew's concerns for Tank 241-C-106 safety and recommendations on avoiding a possible tank bump during a Process Test that delayed water addition to the tanks for several weeks [37]. Agnew was not concerned with the temperature rise itself. The temperature rise, however, was expected to reach beyond the boiling point of 228 °F (adjusted for salt concentration and hydrostatic pressure) and to cause steam formation and dry out of the

waste. The dry waste would have to absorb additional energy (from the decay heat) due to loss or reduction of convective and conductive cooling paths. The resulting hot spot was speculated to be a substantial steam source which could either release steam in numerous relatively harmless gurgles or could flash steam in a longer steam bump. Trickling water into the hot zone was expected to be the cause of steam surges and was used to explain rapid tank level fluctuations. Agnew's concerns were based on the modeling assumption of numerous convective chimneys called 'fumaroles' and an interpretation of the reduced liquid evaporation as reduced capability in external dissipation of heat, resulting in of a heat up driven steam bump.

WHC and associates responded immediately, in a letter, and later in a report issued by Numerical Applications [38]. The letter, written by Apley, a member of the Tank 241-C-106 Temperature Response Team, questioned the modeling assumption of numerous convective chimneys as unsupported by the data. In addition, Apley noted that the rapid temperature rises were most significant for the TC-14 (which had historically read low temperatures) for predicted local waste temperatures. Low temperatures in this case are relative to those generated by using thermal conduction models of Tank 241-C-106. Thus, these fluctuations could be caused by TC-14 momentarily reaching temperatures expected for the nearby sludge. Further, a reduction in evaporation rates was typical immediately following water addition to the tank, which was done periodically to replenish the water level in the tank. This evaporation rate trend, an anomaly outlined in Chapter 1, is as of yet unexplained. As it happened, the temperature rise following the Process Test did not cause a steam bump.

3.2.2 Single Convective Channel Analysis

The authors of the Numerical Applications report, issued March 6, 1995, estimated the convection potential of the TC-14 region as a single annulus surrounding TC-14[6]. In justifying this single annulus assumption, the authors begin the analysis with the assumption of a central region of convection to match TC-14 temperature profiles. Convection is simulated by artificially enhanced thermal conductivity of the sludge. Simulations of cessation of evaporative cooling of the tank leaving only convective air cooling result in temperature increase rates in the sludge that are lower than those

observed in the Process Test data. The authors note that even adiabatic heating (cessation of both convective air cooling and water evaporation at the top surface) does not result in temperature increases at the rate observed and shown in Figure 3.1. The authors conclude that a large region is not being cooled by convection which might have ceased during the process test and that the convection is local, near TC-14. The authors do not determine the size of the region that could heat up at rates similar to the data.
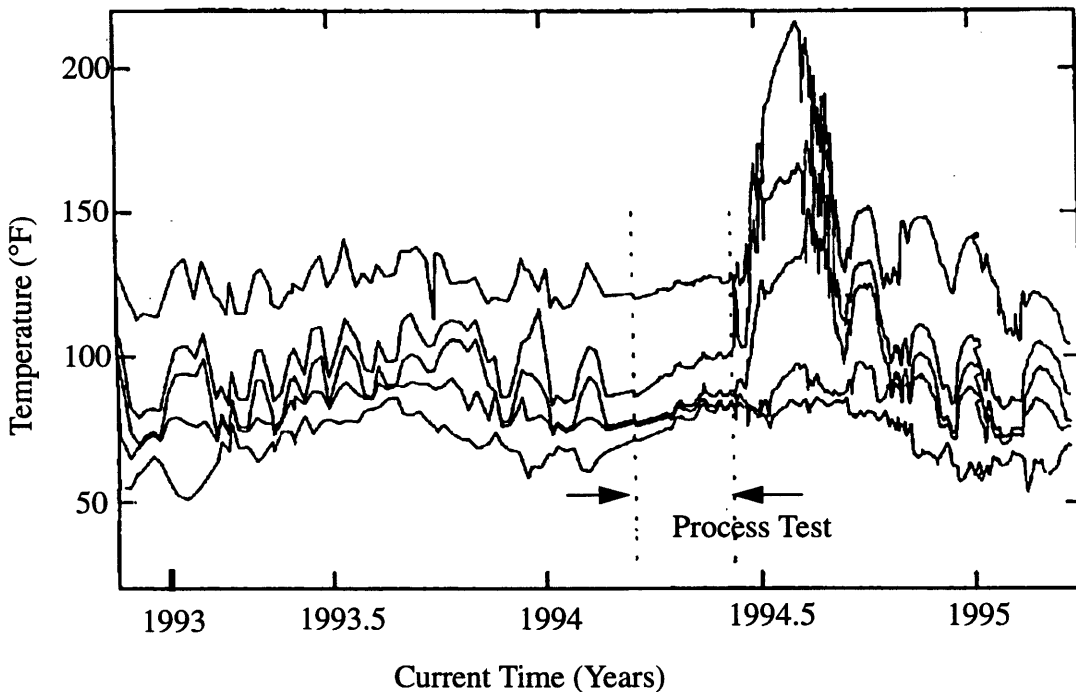
Figure 3.1: Plot of temperature history for TC-14 in Tank 241-C-106.

The authors' second investigation of convection, for the explanation of TC-14 temperature, models this annulus. The authors model an annular section of sludge with a radius of 6 feet, set the temperatures at the center of the annulus, and vary the heat transfer coefficient between the annulus axis and inner radius until the vertical profile at the external surface of the model is equivalent to that in a sludge with no annulus (see Figure 3.2). In this analysis, the top boundary convection coefficient and temperature are given and the bottom boundary is adiabatic. The authors note that an annulus width as small as 1/16th of an inch results in the assumed temperatures (shown in Figure 3.2) being

55

observed for TC-14, at the annulus center, while sludge temperatures as close as 6 feet, at the outside edge, are maintained at those found from pure conduction models. The authors use an annulus center temperature profile, however, not characteristic of measurements (see Figure 3.3). Explanation for determining nominal temperature measurements is found in Section 3.4. The significant difference is in the profile's shape. Figure 3.3 shows the profiles to differ by 10 °F at one edge but differ by 20 °F at the center of the axis. A constant difference between the two profiles can be explained by overall seasonal variations.
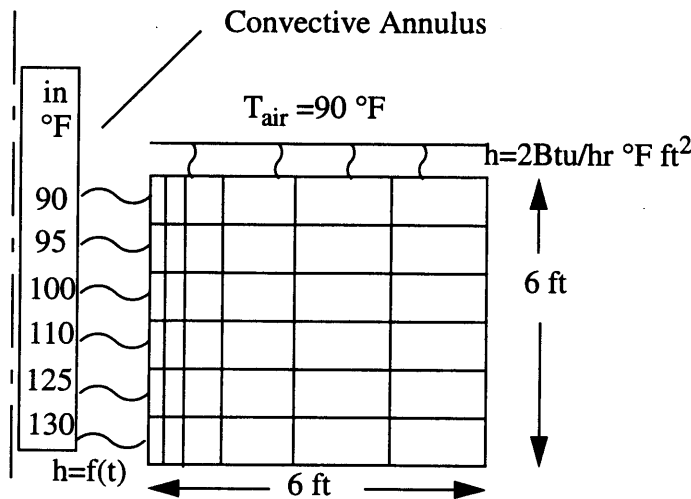
Figure 3.2: Annulus model used by Numerical Applications

During the Process Test, thermocouple position (TCP) 1 on TC-14 heated to 217 °F. Conduction models predict the temperature at the TC-14 location to be 225 °F. The authors postulate that sludge movement caused by sludge swelling closed the annulus Thus, the local convective cooling may have ceased causing rapid increase in the TC-14 readings as they approached adjacent sludge temperatures. Finally, the authors varied the heat transfer coefficient to match diurnal oscillations in the measured temperatures of TC-14 following the process test (see Figure 3.1). Temperature simulation results corresponded well to the measurements at these high temperatures. This fluctuation in heat transfer coefficient is assumed to exist due to temperature induced volume fluctuations of the nearby sludge.
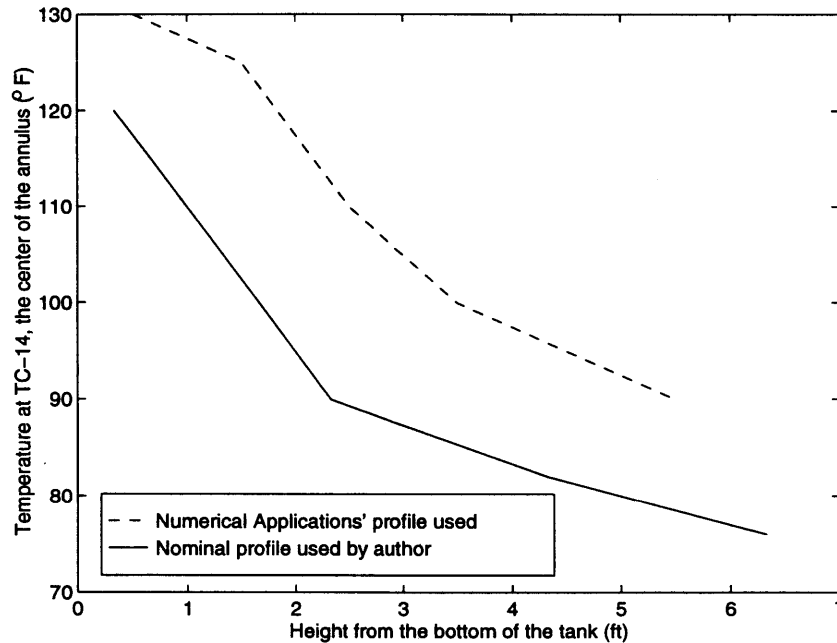
Figure 3.3: Temperature profiles assumed at the center of the annulus.

In summary, the annulus single channel convection work done so far consists of the following assumptions:

- the convection coefficient along the axial length of the annulus does not vary with height,

- the temperature profile used for the center of the annulus has larger temperature gradients at mid height than at either the lower or upper ends (see Figure 3.3),

- the distance affected by the presence of the annulus is limited to 6 feet,

- the modeled annulus and surrounding heat generating material are adiabatic at the bottom edge.

From these assumptions, conclusions of the work of Numerical Applications are that the necessitated annulus width is given as, $\Delta r = \frac{1}{16} in$. The following analysis will characterize the annulus through various thermal models by matching the geometry and temperature magnitude and profile at location TC-14.

3.3 Modeling Approach

The TEMPEST thermohydraulic code developed at PNL is used to model and characterize the annulus. Similar to the analysis of the Numerical Applications report, the cooling of TC-14 is assumed to be provided by a single annulus around the thermocouple tree.

To obtain the thermal steady-state conditions with TEMPEST, I ran a transient model because the convective velocities, coupled with heat transfer, were unknown. Each simulation was run as pseudo-transient consisting of two parts. The first part of the run consisted of a 'normal operation' transient with initial temperatures that were close estimates of final temperatures in which the velocity field was setup. 'Normal operation' consists of a time marching solution in which velocity and pressure changes are computed for a given time increment by satisfying conservation of mass and momentum. These values are then used to determine the temperature by satisfying the energy equation. This first part was a 500 second run. The second part using final temperatures and velocities of part one consisted of a transient which computed a 'steady-state heat transfer solution' (SHTS) at every hydrodynamic time step. This SHTS approach sets the $\frac{\partial T}{\partial t}$ term in the energy equation to zero so that the computed temperatures at each time step differ from the steady-state value only because the velocities computed at that step differ from steady-state values. If the estimate of velocities and temperatures are good this step will quickly approach the steady-state solution. For part two, the resulting steady-state temperatures had little effect on the established velocity field indicating good approximations from part one. This second part was a 500 second run. Trial runs included a third part which began with the final temperatures and velocities of the second part and the SHTS option turned off. No change in velocity or temperature resulted from runs as long as 10,000 seconds, indicating that parts one and two were successful in generating the steady-state solution.

The computer time reduction by this process in comparison to a pure transient was a reduction from a half day to near an hour. The reason for this large change in computer time was that the fluid solution has a much quicker time response than the modeled sludge. The fluid time step then dominated the computer time taken. Moving from part 1

to 2 then skips the long time to model the sludge response as a pure transient. An estimate of the simulated time needed to achieve steady-state conditions can be made assuming that the initial temperature estimate had a shape similar to that of steady-state in the sludge material. This assumption leads to the following energy balance equation:

$$V \rho C_P \cdot \frac{\partial T}{\partial t} + hAT = Q_v V \qquad (3.1)$$

where T is the temperature, V is the volume, and Q_V is the volumetric heat generation. The equation has a time constant, Ω, of

$$\Omega = \frac{hA}{\rho C_P V} \qquad (3.2)$$

This time constant evaluated for the geometry and properties of the sludge results in:

$$\Omega = 920 sec$$

This calculation and all other simulations have used an artificially low heat capacity, C_p, 1/600 of the actual value for the sludge. This value was chosen to quicken the approach to steady-state conditions yet not allow the sludge to be unnecessarily sensitive to oscillations in the convective layers. A calculation time period approximately five times the value of the time constant was found adequate for reaching steady-state when not exercising the SHTS option.

The method for generating boundary conditions for the annulus simulation was a 3 step process beginning with the modeling of the tank including the surrounding soil and finishing with a model of only the portion of the tank near the annulus. The following section describes the models of the three steps, the major assumptions of the models, and the information used from each model.

3.3.1 Tank and Surrounding Soil Model (Model A)

The first model shown in Figure 3.4 is that of the cylindrical tank bounded below by a constant temperature water table and at the sides limited by the proximity of adjacent tanks. Assuming that adjacent tanks have similar heat production the midplane between tanks is taken as adiabatic. The top boundary is just above the liquid level in the tank and extends out to the adiabatic midplane. The top boundary condition within the tank is set as convection to the nominal temperature for air within the tank. The convection coefficient is set knowing the evaporation rate and nominal water layer temperature. Outside the tank, a temperature boundary gradient along the solid portion of the top boundary is taken from simulations run in Bander's report [8]. The water table temperature and depth are taken from the Numerical Applications report [6].
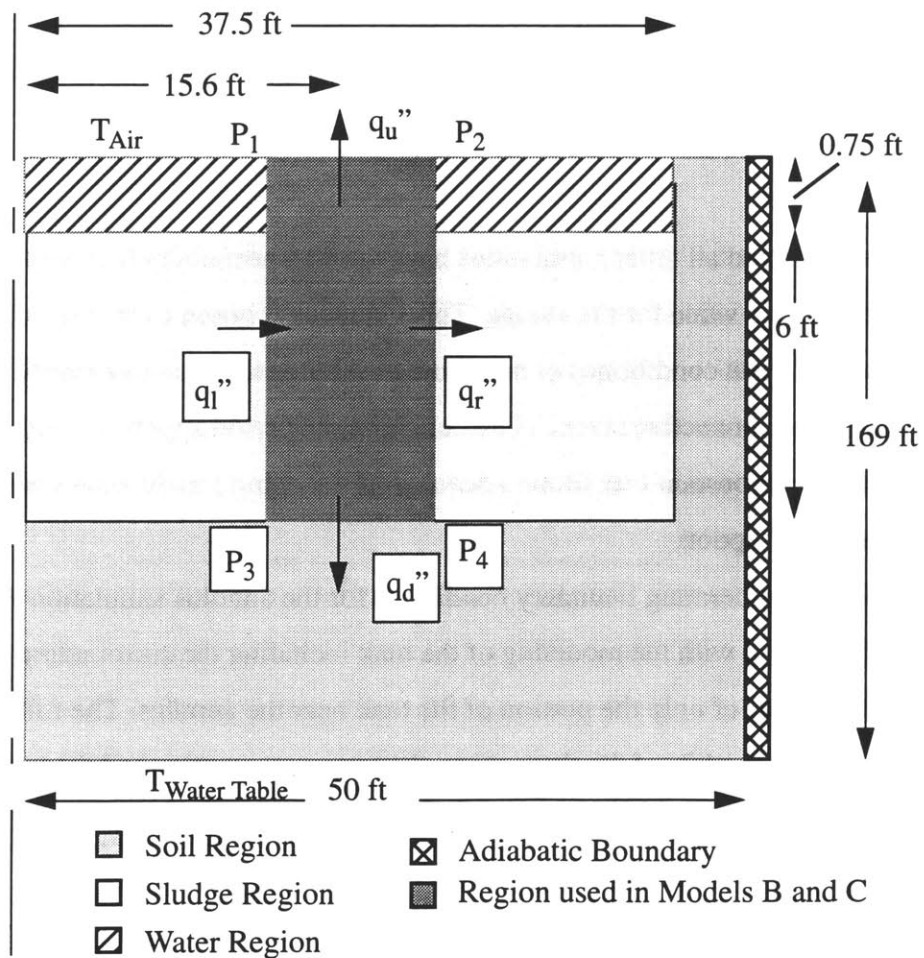
Figure 3.4: Model A: Tank and surrounding soil geometry, calculated heat flux planes, and calculated temperature points.

The figure depicts a 2-D cross section of the cylindrical tank and surroundings. The sludge in the tank, indicated in Figure 3.4, is taken as a solid with three layers of different volumetric heat generation rates. The layer thicknesses are based on settling discussed in an Agnew report outlining the tank history[4]. The relative heat generation rates are taken from a Bander analysis of the transient temperatures caused by the 1992 ventilation outage (see Table 3.1) [23]. The properties of the soil and tank sludge, thermal conductivity, heat capacity, and density, are taken from the Numerical Applications report and outlined in Table 3.2 [6].

Height Above Tank Bottom (ft)	Portion of Total Heat Generated Uniformly Within Designated Region
0-3	78%
3-4	10%
4-6	12%

Table 3.1: Heat Generation Distribution Used in Analysis (Total heat generation =110,000 Btu/hr).

Material	Density (lbm/ ft^3)	Heat Capacity (Btu/lbm/°F)	Thermal Conductivity (Btu/hr/ft/°F)
Sludge	79.7	0.6	0.59
Water	61.3	1.0	0.36
Soil	79.7	0.25	0.15
Thermocouple	61.3	1.0	0.006

Table 3.2: Properties of Elements within Tank

Two results are the object of this simulation. The first is the maximum temperature of the sludge to be compared with that given in previous reports. Second, the fluxes horizontal to the shaded area are compared to those in the vertical direction to check the assumptions made for the next model (Model B).

3.3.2 Tank Section Model Without Annulus (Model B)

The second model is for a section of the tank centered at the TC-14 location and again assumes azimuthal symmetry allowing 2-D representation of the cylindrical model (see Figure 3.5). The fluxes from the previous analysis are used to check the assumption made in this analysis of an adiabatic boundary at the side of this modeled cylinder (typically in the analysis of Model A, less than 97% of the heat transport is found to be in the vertical direction). The top boundary convection coefficient is adjusted knowing the flux at this plane and nominal temperatures of air and water. The bottom heat flux is taken from the previous analysis. This unidirectional heat flux model sets the temperature profile expected at the distance where the annulus cooling effects are negligible. This profile will be used in the next model to determine the area affected by the modeled annulus.
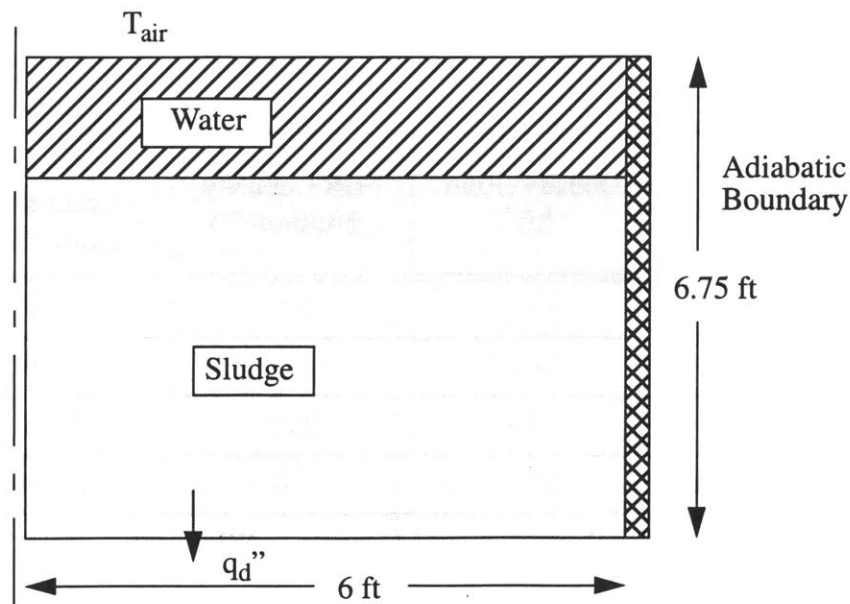
Figure 3.5: Model B: Tank section without annulus

62

3.3.3 Tank Section Model With Annulus (Model C)

Figure 3.6 shows the geometry of the third model which includes a thermocouple tree surrounded by an annulus which exchanges fluid with the layer of fluid overlying the heat generating sludge. The thermocouple tree is assumed to have a low thermal conductivity so that it does not act as a parallel conductive path transporting heat directly to the cooler tank air. The temperature measurements then are not dependent upon each other but upon the liquid temperature at that axial position which is an assumed design requirement for the thermocouple tree.
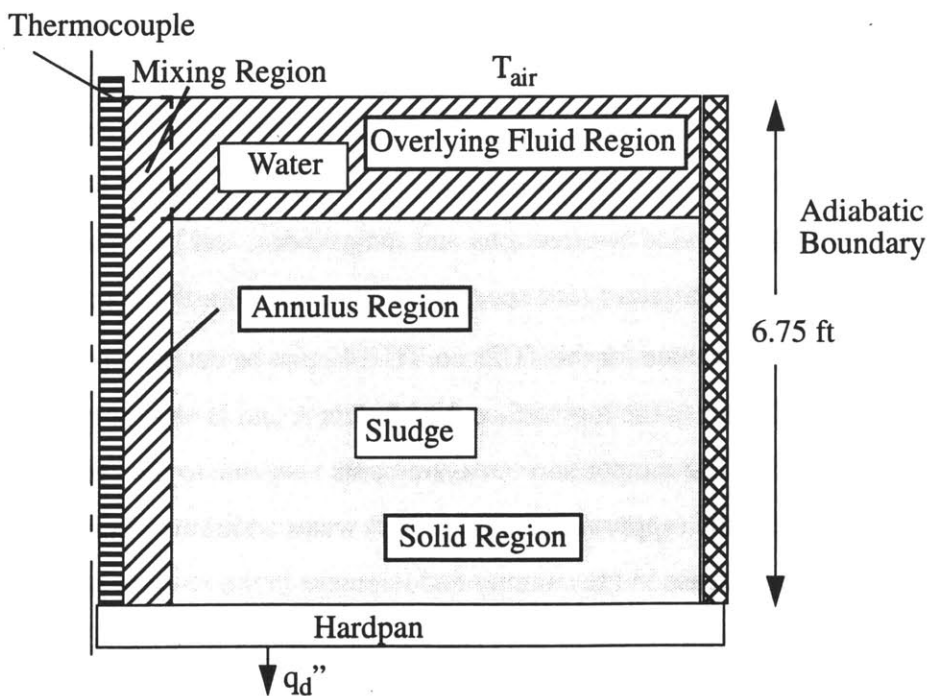
Figure 3.6: Model C: tank section with annulus

Previous models assumed the tank bottom to be flat. In actuality, the bottom of the tank has center sloping depression creating a low aspect ratio (H/r) cone below the tank (see Figure 1.1). This region, referred to as the hardpan, is expected to be impervious to fluid [23]. This hardpan supplies heat below the annulus. The radial variation in thickness is removed but the volume kept constant by approximating this low aspect ratio inverted cone as a low aspect ratio cylinder. Boundary conditions are kept as determined for the second model. Again the fluid is modeled with zero slip for the fluid at the bottom and

63

both sides of the annulus and at the bottom of the overlying fluid layer; because the thermocouple, sludge, and hardpan are modeled as solid.

This model and slight variations establish the numerical results reported in this chapter. The results include the necessitated annulus width and the area thermally affected by the annulus. Model variations are used to establish the effects of heat generation in the annulus, varying annulus width with height, and changing the overlying fluid layer thickness, Sections 3.5.3-3.5.5, respectively.

3.4 Validation and Generation of Tank Section Model with Annulus

For each model the number of nodes was doubled to determine if the simulated temperature and velocity results were affected by the mesh size used to generate results. Further, temperature magnitudes, velocity directions and magnitudes, and heat fluxes where compared to those reported in literature for experiments describing similar geometries.

The nominal temperature values for the TCPs on TC-14 must be determined for setting heat transfer coefficients at the top surface for Models A and B and for matching annulus profiles in Model C. The temperature measurements vary due to the seasonal external conditions and periodic (approximately monthly) water additions. As may be expected, the temperature increase in the summer and decrease in the winter for TCPs closer to the tank surface are more pronounced. The oscillations due to water addition, however, are more significant for TCPs close to the tank bottom.

For the purpose of estimating annulus characteristics the following procedure was used to generate nominal temperatures at the positions of TC-14. First, it is assumed that reducing the overlaying water layer thickness has little effect on the water temperature profile in the annulus, as will be shown in Section 3.5.5. This assumption implies that the water temperature increase, lasting near 10 days, after water addition and the ensuing temperature drop as the water continues to evaporate is not modeled. Second, from graphs provided in Bander [7] a visual curve was drawn averaging the monthly oscillations, but following the seasonal variations. Maximum and minimum values were taken from the curves as the summer and winter values, respectively. After subtracting the amplitude

oscillation caused by the water additions (because of the above outlined assumption) the winter and summer values were averaged to generate nominal values for five positions on TC-14. Table 3.3 outlines the results of these visual estimates. The resulting profile is compared to that presented in the Numerical Applications report in Figure 3.3. Differences in the profile are discussed in 3.2.2.

Distance from Bottom of Tank (ft)	Summer Median Value (°F)	Winter Median Value (°F)	Summer Low Value (°F)	Winter Low Value (°F)	Summer and Winter Low Average (°F)
8.33	80 ±4	58 ±4	76	54	65
6.33	90 ±4	70 ±4	86	67	76
4.33	95 ±6	80 ±6	89	74	82
2.33	105 ±7	90 ±8	98	82	90
0.33	130 ±6	120 ±4	124	116	120

Table 3.3: Temperature Estimate of TC-14 Profile from Figure 3.1

3.4.1 Tank and Surrounding Soil Model (Model A)

The first model, shown in Figure 3.4, incorporates the soil surrounding the tank and boundary conditions described in Section 3.3.1. The value used for the soil thermal conductivity was the lower of two provided in the Numerical Applications report. Increasing this value reduced the maximum temperature at the center bottom of the sludge and increased the radial temperature gradient in the sludge as expected.

The boundary heat transfer coefficient was determined by knowing the average evaporation rate from the liquid level and using the nominal temperatures of the tank air and water. The expression used for the effective heat transfer coefficient,

$$h = \frac{q''}{\Delta T} = \frac{\dot{e} h_{fg} \rho}{T_W - T_A} \qquad (3.3)$$

results in the following coefficient with an evaporation rate, $\dot{e}$, of 0.08in. per day [11],

65

$$h = 1.65 \frac{Btu}{hrft^{2\circ}F}$$

Figure 3.7 shows the effect of halving the mesh size, comparing temperature profiles for the two mesh sizing. The figure shows that negligible temperature variations are found with the increase in the number of nodes and that the present meshing predicted temperatures are satisfactory.
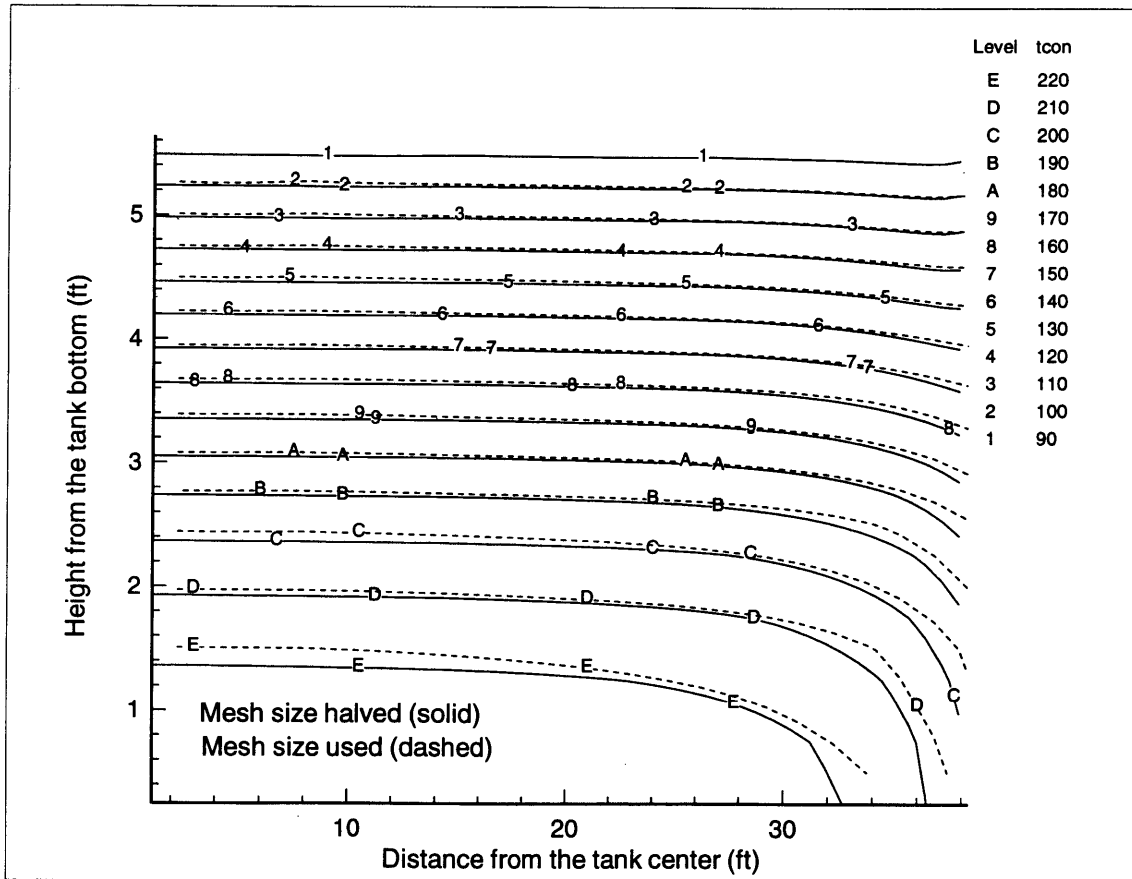
Figure 3.7: Effect of reducing mesh size for Model A in (°F)

The code's calculation of heat transport across the liquid layer can be checked against that reported in the literature for convection between plates. Hollands et al. correlated previous data and their own data for water convection in this configuration [39]. Transition to turbulent convection based on water depth, D, is near an external Rayleigh number of 10^6, where

$$R_{E,D} = \frac{g\beta\Delta T_T D^3}{\nu\kappa} = 1 \cdot 10^6. \tag{3.4}$$

From the parameters calculated in the code and fluid properties, the external Rayleigh number is:

$$R_{E,D} = 4.1 \cdot 10^8$$

for $\Delta T_T = 1.0$ °F and D=0.75ft, validating the use of turbulent heat transfer above the porous layer in the code. For such a highly turbulent heat transfer the fluid can be modeled in two sections: one that is near the boundary, the conduction layer, with the same resistance as the actual boundary layer and an isothermal core of well mixed fluid (see Figure 3.8). This isothermal core is formed at the center of the liquid layer. In addition, as reported by Chu and Goldstein, increasing these high Rayleigh numbers generates vigorous horizontal fluid movement and breaks down the convective cells [40]. Assuming negligible end effects due to the low aspect ratio of the region, the conduction layer thickness is given by:

$$\delta_{BL} = \frac{1}{C_t}\left(\frac{\nu\kappa}{g\beta\Delta T_{BL}}\right)^{1/3} \tag{3.5}$$

where C_t is a weak function of Prandtl and estimated to be 0.13 for water by Fuji and the temperature difference is that across the boundary layer [41]. For the temperature drop from the porous layer to the isothermal core taken from the simulation, the conduction layer thickness is

$$\delta_{BL} = 0.1in$$

based on the calculated $\Delta T_{BL} = 0.5$ °F (or $\Delta T_T = 1.0$ °F). For a boundary layer of the same order we see that mesh sizing of 1.5" is too large to capture this layer detail. Knowing an estimate of the heat flux at this point from the simulation one can estimate the expected temperature drop according to the correlation. The correlation for Nusselt number

$$Nu = 0.0516\,(R_{E,D})^{1/3} \tag{3.6}$$

can be converted to an expression for temperature drop in terms of known heat flux and fluid properties.

$$\left(Nu = \frac{q''D}{\Delta T k}\right) \Rightarrow \Delta T = \left(\frac{q''}{k}\left(\frac{1}{0.0516}\left(\frac{g\beta}{v\kappa}\right)^{-\frac{1}{3}}\right)\right)^{3/4} \tag{3.7}$$

which gives:

$$\Delta T_T = 1.2°F$$

Note that this temperature difference is not a function of water depth, D, as expected given the isolated boundary layers at each edge.
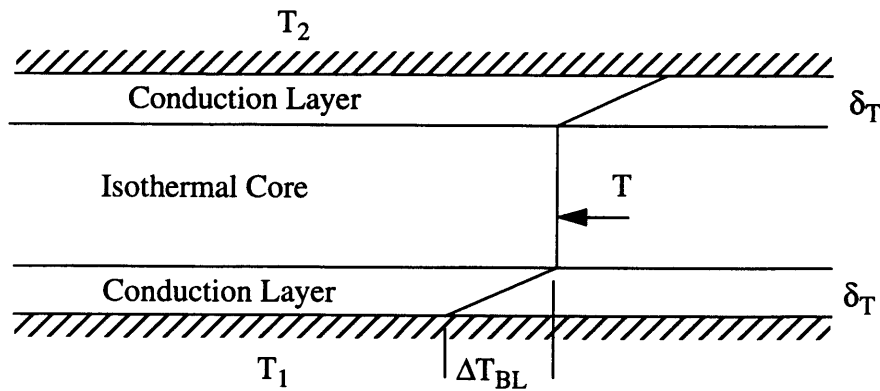
Figure 3.8: Regions of the turbulent heat transfer model between two horizontal plates.

Two questions result from this analysis: (1) what causes the computational and experimental difference in temperature drop, and (2) is this difference significant? The cause as mentioned before may be the mesh sizings. A second cause may be the turbulent model used in the TEMPEST code which is the (K,ε) model with coefficients that are supposed to model forced convection as well as the natural convection present in this case. Using a single set of coefficients for two situations with considerably different physics may be the source of this error. The difference in the calculated drop and expected drop, however, is 0.2 °F, a degree not justifying the order of magnitude decrease in mesh size

and corresponding increase in computation time necessitated to model this boundary layer explicitly.

The results from this first model, Model A, give a maximum sludge temperature of 231 °F at the tank center bottom. Because the saturation temperature is estimated to be 228-230 °F, however, this number reflects the presence of steam. The steam region, area exceeding 228 °F, is about 48 ft in diameter and 0.8 ft in height (see Figure 3.9). (Note that the graph's y-axis begins at 0.5 ft.) The heat fluxes around the shaded section of Figure 3.4 are summarized in Table 3.4. The temperatures at the points marked on Figure 3.4 are given in Table 3.4. From the relative magnitude of horizontal to vertical heat fluxes and lateral temperature differences the second model assumes adiabatic side boundaries and a tank section with predominant vertical heat transfer.
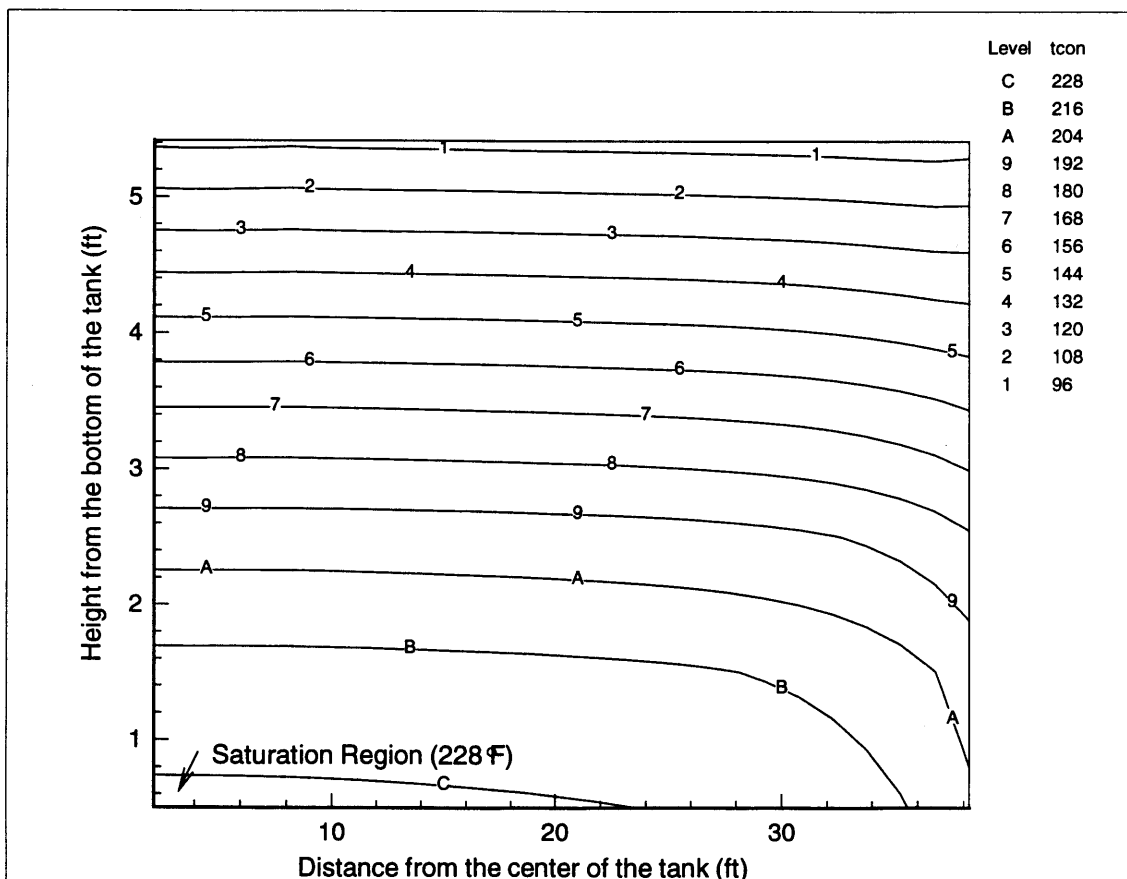

Figure 3.9: Temperature contours showing steam region in full tank model (°F).

69

Point of Figure 3.4	Temperature (°F)	Boundary of Shaded Region in Figure 3.4	Heat Flux (W/m^2)
P$_1$	93.66	Upper	6.6e-3
P$_2$	93.28	Lower	1.1e-4
P$_3$	230.09	Left	1.3e-5
P$_4$	229.37	Right	1.7e-5

Table 3.4: Computed Temperatures and Heat Fluxes from Model A

3.4.2 Tank Section Model Without Annulus (Model B)

The second model shown in Figure 3.5 is centered at the TC-14 location 15.6 ft from the tank center. Knowing the relative heat fluxes from Model A, the heat transfer coefficient was computed for the top boundary using the nominal temperatures of the tank air and water. The expression for the effective coefficient,

$$h = \frac{q''}{\Delta T} = \frac{Q_v}{A_u} \cdot \left(\frac{q_u}{q_t}\right)\frac{1}{\Delta T},$$
(3.8)

gives

$$h = 2.2\frac{Btu}{hrft^{2\circ}F},$$

knowing that 97% of the heat generated is dissipated from the top boundary.

Using equations 3.6-3.7, the temperature drop across the overlying fluid from the simulation, 1.4 °F, and the temperature drop expected from equation 3.7, 1.1 °F, differ by 0.3 °F. The conduction boundary layer thickness from equation 3.5 is 0.11 in, much less than the used mesh size of the liquid 1.5 in. Again, this difference is not considered large enough to justify renodalization.

Figure 3.10 shows the axial temperature profile generated from this simulation. The maximum temperature is slightly lower than that found from the first model at this position. The results from halving the mesh size are shown as well with no increase in

accuracy. This profile will be matched to that at the edge of the annulus model, Model C, to determine the amount of sludge affected by the annulus.
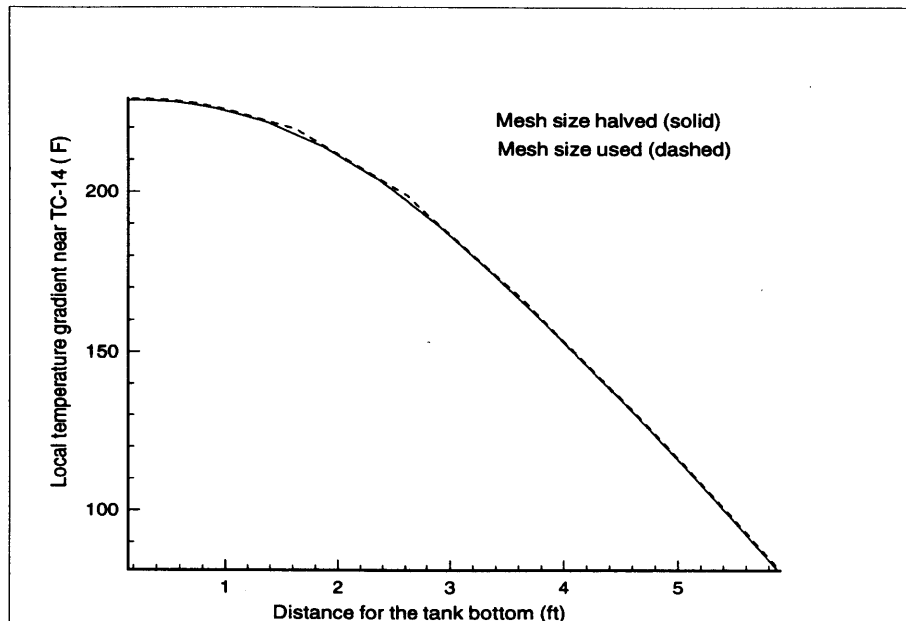

Figure 3.10: Comparison of the effect of mesh sizing on the 1-D Gradient of Model B.

3.4.3 Tank Section Model With Annulus (Model C)

Four major regions exist in the annulus model as shown in Figure 3.6, the solid region, the overlying water region, the annulus water region, and the mixing region connecting the two water regions. The mixing region velocity and temperature distributions are strong functions of the other two regions and will be assumed to be correctly modeled if the others are. The following validation was done for a nominal annulus gap width, Δr, of 1in. The inner radius of the annulus, set by the radius of the thermocouple tree, is taken as 0.5in. The amount of surrounding sludge modeled by the solid region is increased until further increase does not affect annulus temperatures and velocities. The complete region is modeled with 24 cells in the radial direction and 35 cells in the axial direction including the boundary cells around the perimeter (see Figure 3.11). Note that Figure 3.11 does not include the full number of cells in the mid range of the annulus nor those at large radii

which follow the sizing trends indicated in Figure 3.11. Dimensions of the cells depend on the simulation. The annulus is modeled with 10 equivalently sized cells in the radial direction. The remaining 12 cells' thickness steadily increases in the radial direction through the solid. The axial mesh heights are small at the bottom of the annulus and top of the annulus where 2-D flow effects tend to be more pronounced. The center of the annulus has larger height cells. As the meshing increases in the solid radially so does that in the overlying layer of fluid. The overlying fluid layer depth is modeled with six cells.

3.4.3.1 Solid Region Validation

The solid region should have temperatures at the edges on the same order as those found from the second model without an annulus. The temperature gradient should increase due to internal heat generation and direction of the heat flux, as one moves toward the annulus and up from the bottom. Figure 3.12 shows the solid temperature map in which both previously discussed trends exist. (Note that the annulus center is the axis for the concentric cylinders which compose the edges of the annulus.)

3.4.3.2 Overlying Liquid Region Validation

The overlying fluid layer can be checked as done previously for Models A and B. Assuming infinite parallel horizontal plates, negligible end effects due to both the edge and the annulus of this low aspect ratio region, the same correlation can be used. Results are similar in that the temperature drop predictions differ by a negligible amount. The TEMPEST calculated temperature drop is $\Delta T = 1.2°F$. From equation 3.5, the conduction layer thickness is $\delta_T = 0.11 in$. The expected temperature drop from equation 3.7 is $\Delta T = 1.2°F$. Again the isothermal core is present as expected (see Figure 3.13).
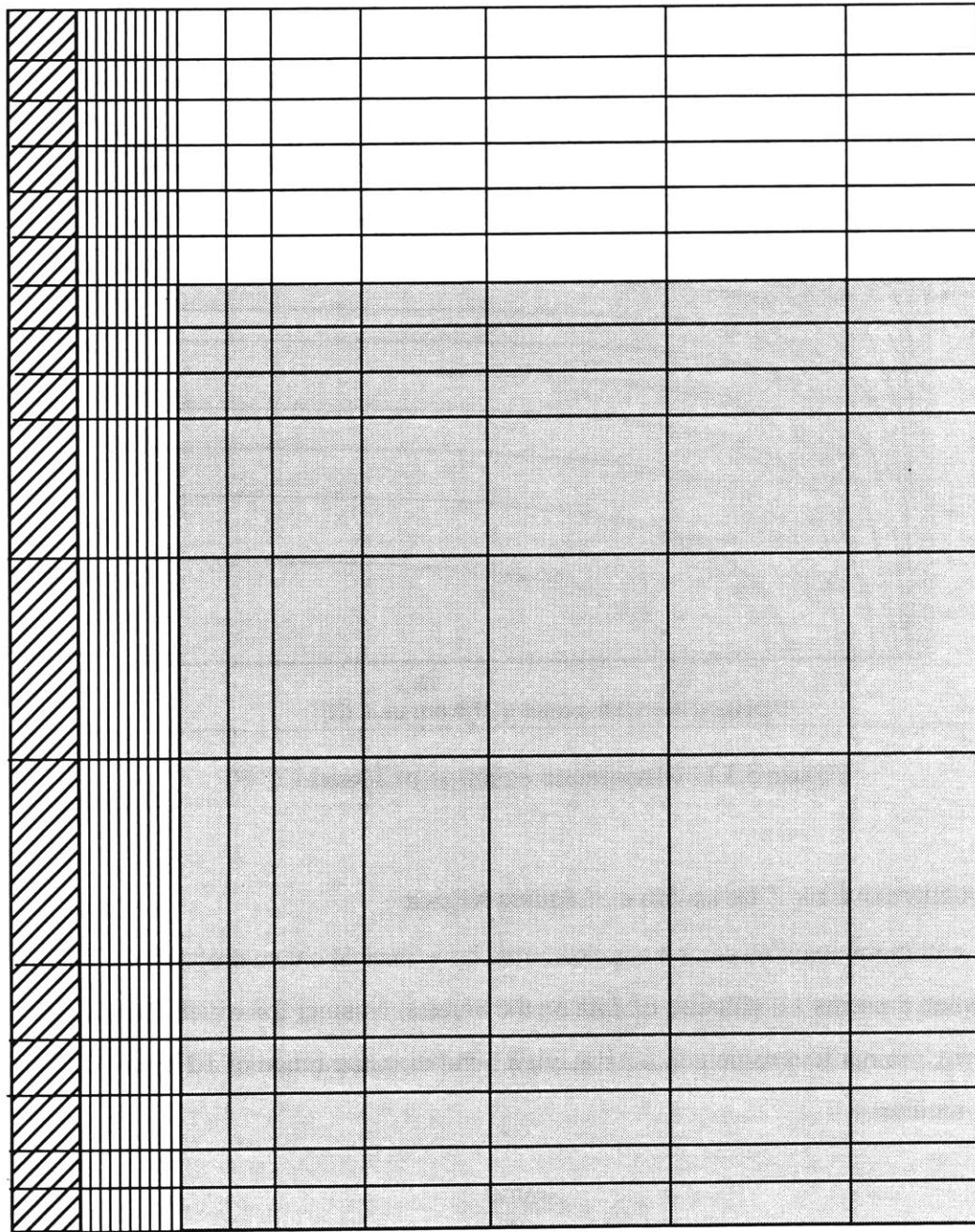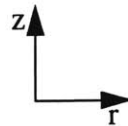
Figure 3.11: Qualitative meshing of Model C
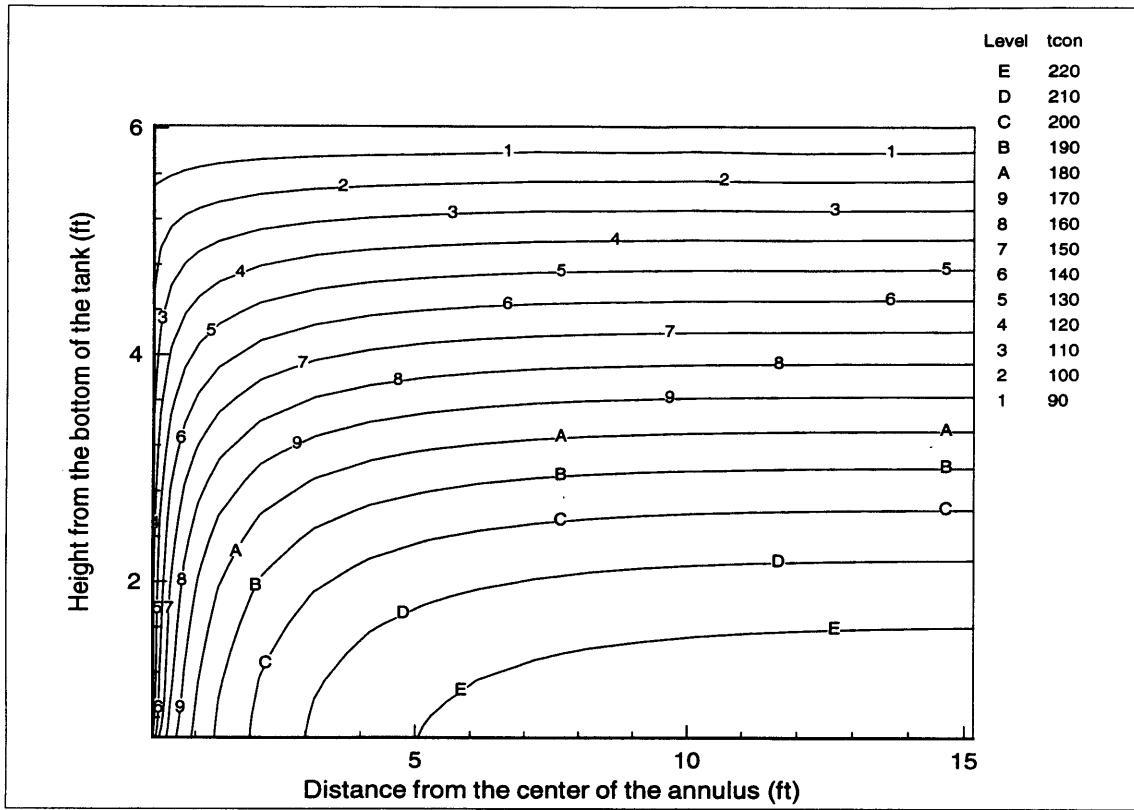
Figure 3.12: Temperature contours of Model C (°F)

3.4.3.3 Qualitative Flow Description of Annulus Region

Flow within the annulus can be approximated by a vertical channel of infinite depth [42]. Holman presents a collection of data on the vertical channel for which the transition region from laminar to turbulent is for Rayleigh number in the range of 10^6 to 10^7, where Rayleigh number is

$$R_{E,d} = \frac{g\beta\Delta T d^3}{\nu\kappa} \tag{3.9}$$

based on channel thickness, d (see Figure 3.14). Using code generated ΔT across the annulus the Rayleigh number based on an 8 °F temperature difference is

$$R_{E,d} = 1.7 \cdot 10^6$$

which is in the transition region.

74
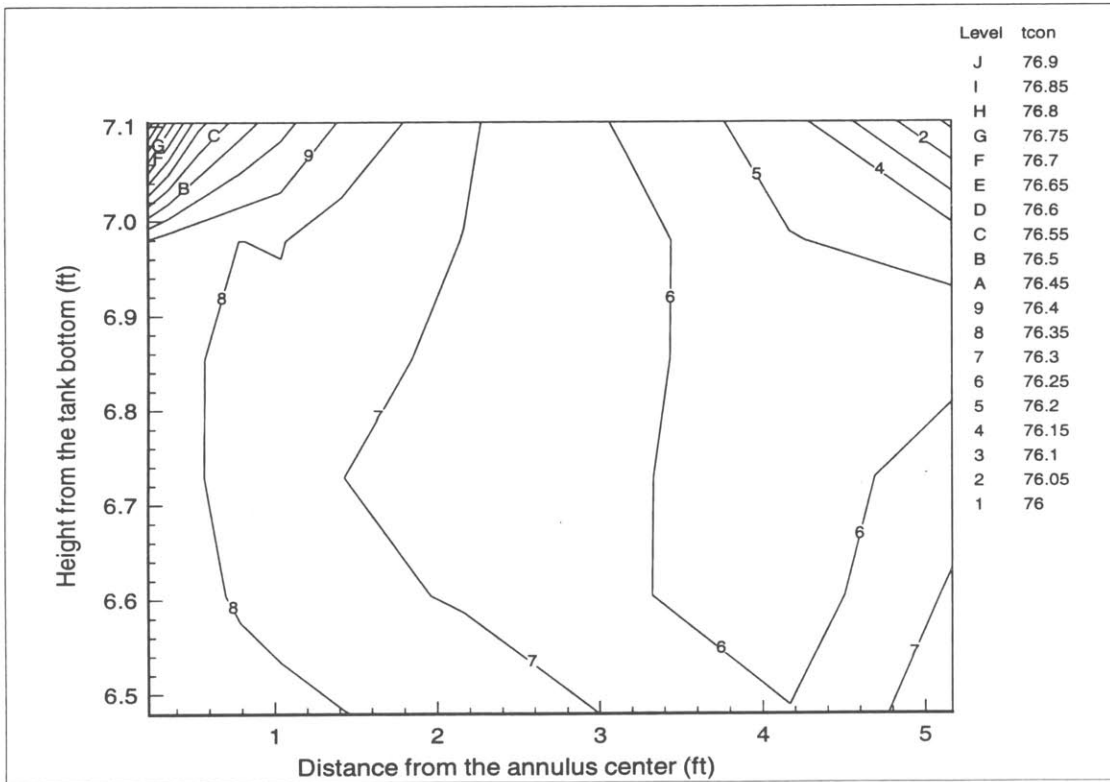
Figure 3.13: Temperature contours calculated in overlying water layer (°F). (Note that this height includes the height of the hardpan.)
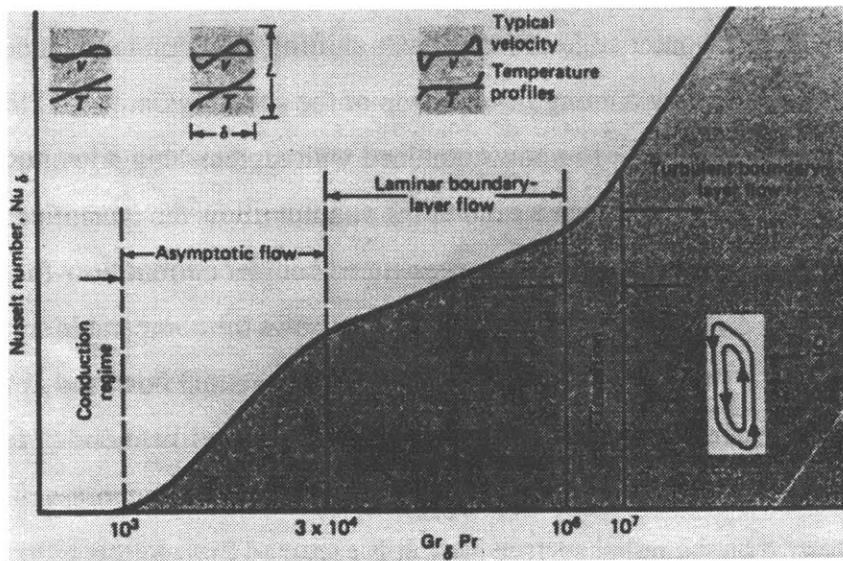
Figure 3.14: Flow regions in narrow convective channels as a function of Rayleigh number, Holman [42].

The TEMPEST code computes both a turbulent effective viscosity based on the (K,ε) model, compares it with the fluid viscosity, and uses the greater of the two for the momentum equation. Because of the value of the Rayleigh number and the particular constants of the (K,ε) model used, however, the code may make an error in computation necessitating the user to impose either turbulent or laminar flow. Figure 3.15 compares laminar and turbulent modeling within the annulus. Because the outer annulus wall formed by the surrounding sludge is likely to be rough with height dependent radius, two characteristics inducing turbulence, the flow in the annulus is assumed turbulent. The TEMPEST code calculates the flow as turbulent using the (K,ε) model.

3.4.3.4 Quantitative Comparison of Annulus Region Flow Results

A major assumption of this modeling is that the flow field is adequately described by a 2-D cross section of the cylinder so that a 3-D model of the flow is unnecessary. Considering the annulus entrance region, high aspect ratio, and low thickness ratio, this assumption may not be true (see Figure 3.17 for definitions). Figure 3.16 shows a typical flow pattern for the simulations. The left edge is adjacent to TC-14 and the right edge is adjacent to the heat producing sludge for the bottom 5.83 feet. The mixing region shows the upward flow from the outer edge of the annulus shifting direction to the inner edge after interaction with the flow coming from the top of the solid region. In 3-D this could involve circumferential regions of upflow combined with replenishing downflow for the annulus. The aspect ratio and thickness ratio of the annulus allow the quantification of the interfacial shear area existing between the necessitated counter current flow for this geometry (see Figure 3.17). A top view of the annulus shows the comparable surface areas for flow directions as a function of planar angle, Φ, circumferential flow, and as a function of r, radial flow. Increasing the thickness ratio would increase the likelihood of radial flow. For a thickness ratio of 2 (found in the range of this analysis), the circumferential surface area is 60% greater than the radial surface area. It is expected that counter current flow in the annulus would flow in a manner that would reduce friction, in this case reduce the
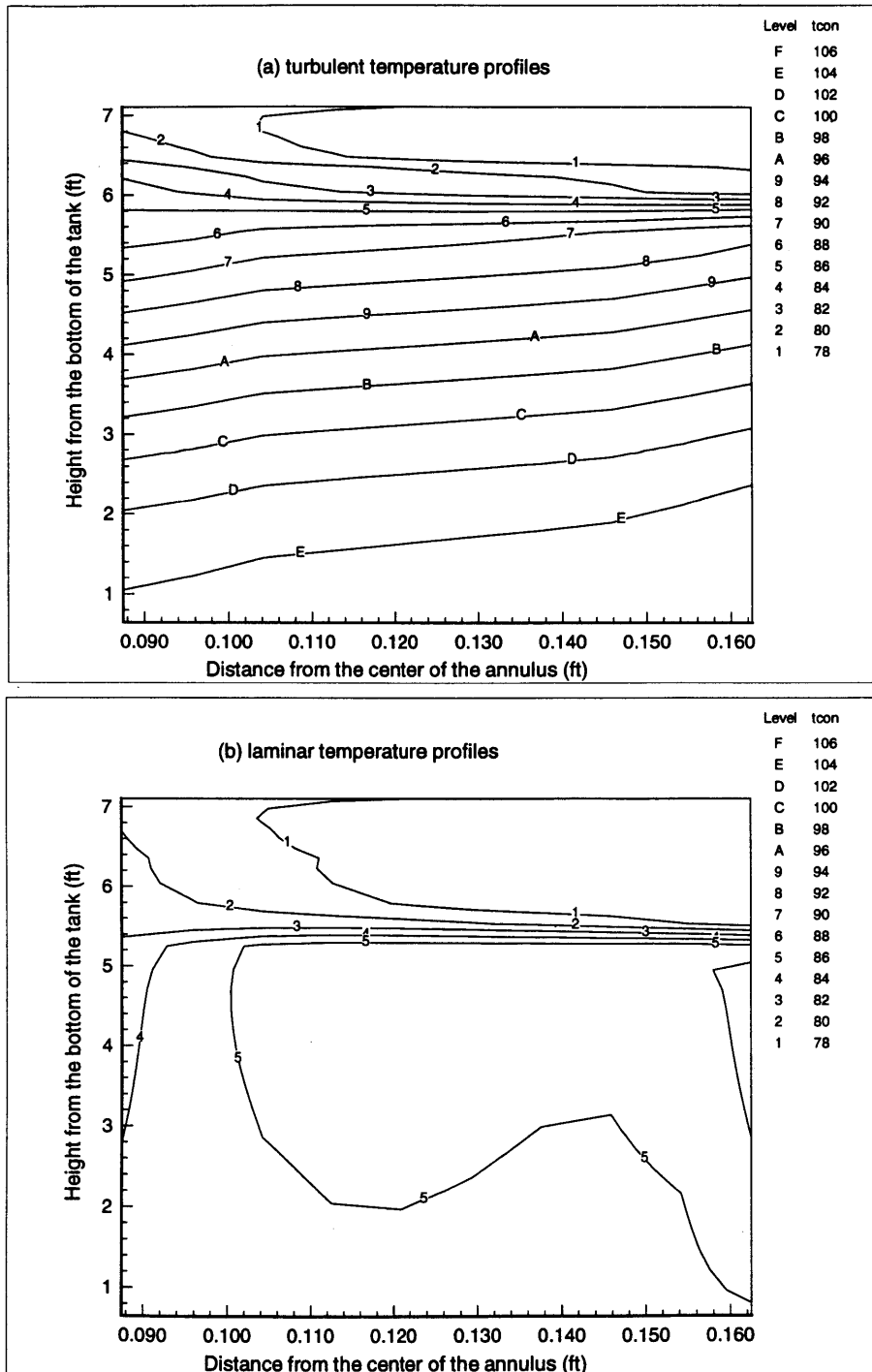
Figure 3.15: Thermal mass in the annular region with (a) turbulent flow imposed and (b) laminar flow imposed (°F).

contact surface between upward and downward flows. A greater surface area for interaction between the flows for circumferential area case would then imply the flow would be radial to minimize the friction between the counter current flows. Literature shows that for a thickness ratio lower than 0.075 the flow is circumferential [43,44]. A high aspect ratio also increases the counter current surface area and possibly induces circumferential flow. For this region, however, the driving force for the flow is the heat addition at the outer edge of the annulus. The 2-D assumption then is that the upward buoyancy at the outer edge of the annulus draws fluid down the center of the annulus regardless of the entrance region so that the flow is radial. Analysis of an annulus of 1/16 in. width, as suggested by the Numerical Applications report, would more likely require a 3-D model for this size of a thermocouple tree.

Figure 3.16: Typical flow observed within the annulus region for various configurations (note that the top flow arrows are large enough to overlap so that only the arrow head is distinct).

Aspect Ratio = $H/(r_o - r_i)$

Thickness Ratio = $(r_o - r_i)/r_o$

...... Interface v=v(phi)

_ _ Interface v=v(r)
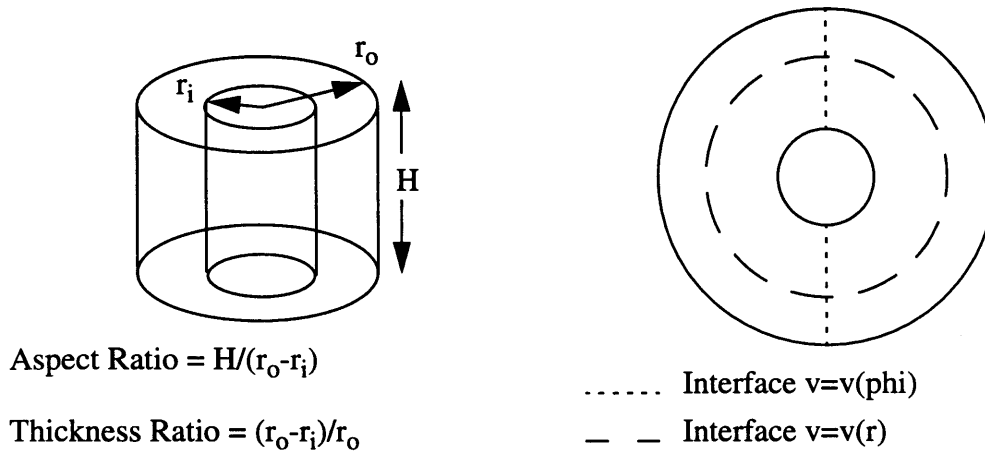
Figure 3.17: Annulus region definitions and potential flow patterns.

For the annulus, the TEMPEST results for the heat flux at the outer radius, temperature distribution and velocity distribution should correlate with the data from the literature both quantitatively and qualitatively. I draw from three different flow experiments to provide this validation. The fi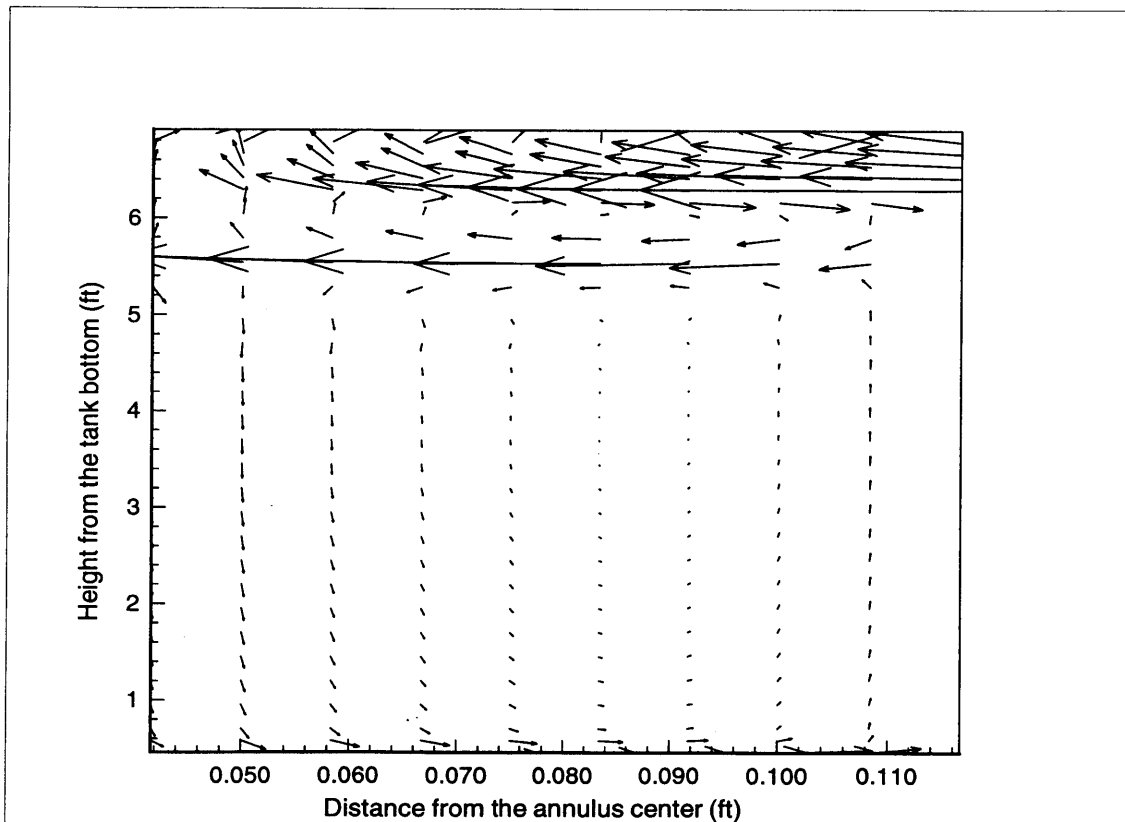rst is a 2-D convection cell (note that the annulus geometry is often generalized to an infinite depth 2-D cell) of similar order height and width, heated from the bottom, cooled from the side and insulated elsewhere (see Figure 3.18a) [45]. Because of the high Rayleigh numbers, this experiment generates boundary flows at the walls distinct from a turbulent isothermal core. The second experiment, shown in Figure 3.18b, is differentially heated, long concentric cylinders insulated at the ends with $R_{E, d} < 10^5$, causing laminar flow ($R_{E, d, tr} = 10^6$) [46]. The third is a collection of data for a range of differentially heated high aspect ratio convective channels (see Figure 3.14) [42].

The temperature distribution in the annulus for our nominal case with a gap width of 1 inch is shown in Figure 3.15a. The temperature distribution shown in this figure has a larger temperature gradient at the top than at the bottom of the annulus, a characteristic noted in the isotherms of a long thin annulus with a thickness ratio of 0.5, an aspect ratio of 10, and laminar flow[46]. In the convective cell experiment, modeling the equivalent of a thick annulus in turbulent flow [45], the vertical cooling surface is isothermal giving an
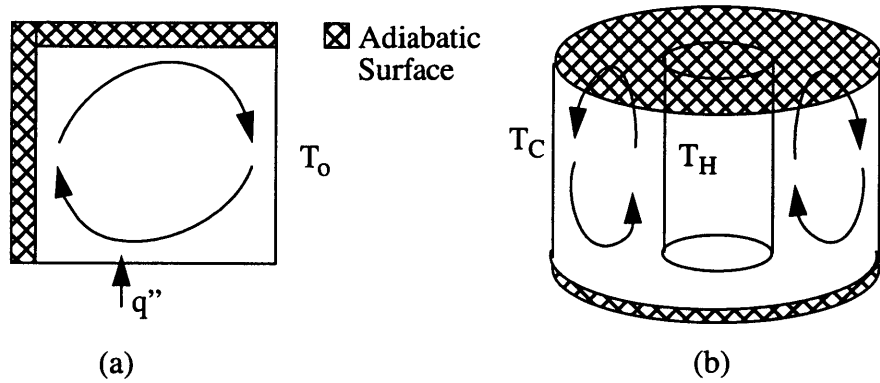
Figure 3.18: Geometry of experimental studies used to validate calculations.

isothermal core. The simulation profile plot may be a reflection of the highly turbulent nature of the flow within the annulus which has a core profile similar to the boundary surface. For the simulation, the core profile is parabolic as is the profile at the solid edge (see Figures 3.15a and 3.12 respectively). The core profile then parallels that at the edge. The overall matching of core to wall temperature profiles is due to the significant mixing present in turbulent flow. The lateral temperature gradients of Figure 3.15a, however, show that the core is not radially isothermal either as would exist for noninteracting boundary layers in a turbulent cell. For a noninteractive boundary layer on the outer radius of the annulus of height, H, this boundary layer is on the order of

$$\delta_a \sim \frac{H}{(R_{E,H})^{0.2}} = 0.23 in \tag{3.10}$$

where

$$R_{E,H} = \frac{g\beta\Delta T_H H^3}{\nu\kappa} \tag{3.11}$$

which is on the order of two annulus mesh widths, but less than the total annulus width [45]. Therefore, though flows up and down the annulus interact, the flows maintain characteristics of noninteractive turbulent boundary layers that exist for thick annuli. The temperature profile at the annulus midpoint is shown in Figure 3.19a. The steadily

decreasing gradient from the outer radius to the inner radius is expected with an adiabatic inner radius [42].
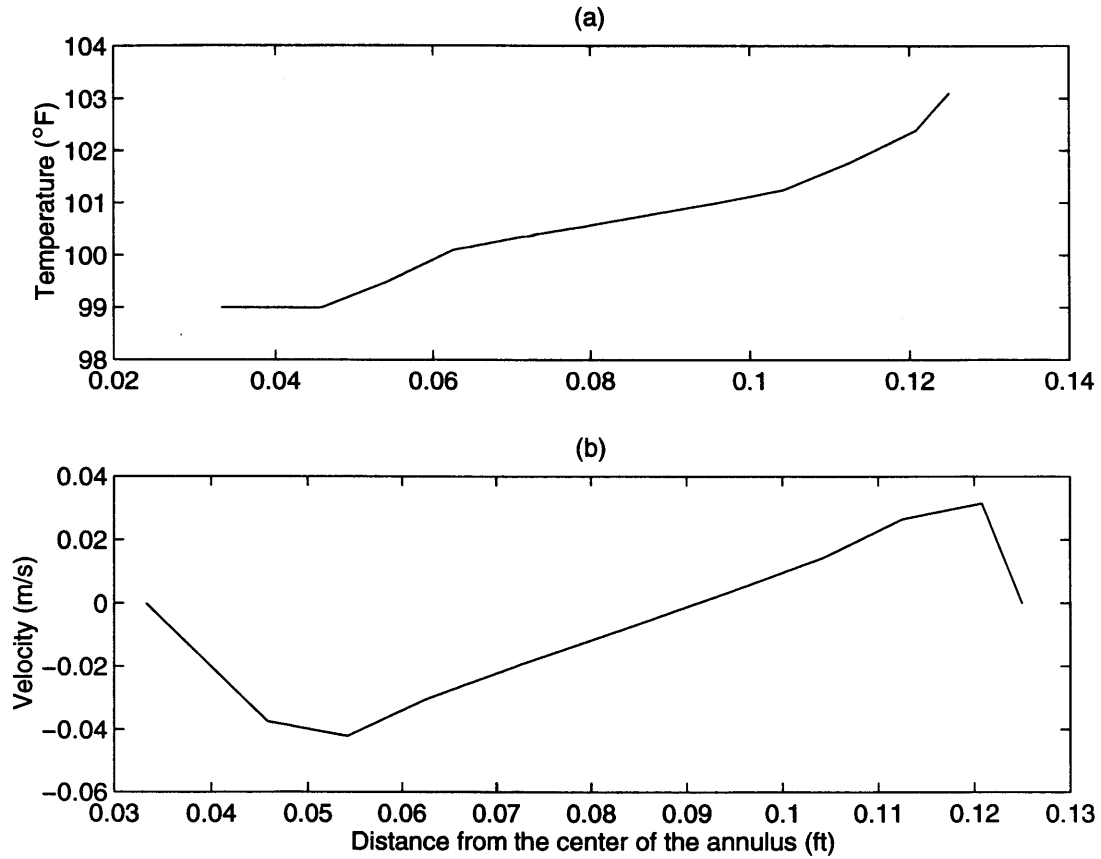
Figure 3.19: Typical (a) velocity and (b) temperature across annulus at mid-height.

The velocity profile at the midpoint of the annulus is shown in Figure 3.19b. Qualitatively, this profile is expected because the inner radius is insulated, while near the outer radius the entering heat flux causes a more peaked flow profile. The flow velocity is expected to be on the order of

$$v \sim \frac{\kappa}{H} (R_{E,H})^{0.4} = 0.03 \frac{ft}{s} \tag{3.12}$$

as found in Figure 3.19b [45]. In preserving mass continuity, the flow magnitude at the inner radius (lower flow area) is slightly larger.

The heat flux should also correlate with the temperature difference for the annulus. Again assuming boundary layer development unaffected by the flow on the inside of the annulus, one can use Anderson's data [45]. Anderson notes from experimental data that:

$$Nu = 0.579 \, (R_{E,H})^{0.173} \, .$$ (3.13)

The expected heat flux then is:

$$q'' = h\Delta T = 0.579 \, (R_{E,H})^{0.173} \frac{k\Delta T}{H} = 0.02 \frac{Btu}{ft^2 s} \, .$$

This corresponds well with the heat flux profile over the outer radius shown in Table 3.5. Qualitatively we would expect the heat flux to decrease at higher elevations in the annulus because of the temperature gradient in the adjacent solid. In addition, for heat generated in the solid, the thermal resistance to the side is less than that to the corner of the solid. The lower value at the bottom of the annulus is caused by heat loss at the bottom boundary. Both the estimate of velocity and heat flux based on dimensional analysis is only significant in matching the order of magnitude.

Distance from the Bottom (ft)	Heat Flux at Annulus Outer Edge (W/m^2)
0-1.25	0.039
1.25-2.25	0.043
2.25-3.25	0.032
3.25-4.83	0.017
4.83-5.83	0.004
0-5.83	**0.027**

Table 3.5: Computed Heat Flux at Annulus Outer Edge for Model A with Nominal Width of 1.0 in.

3.5 Annulus Characterization

3.5.1 Gap Width

The previous analysis was done with a nominal annulus width of 1.0 in., knowing this value to be close to the results generated in this section. When varying the width of the annulus it became apparent that matching all four temperatures measurements would not be possible by simply varying the annulus width. The three top submerged thermocouples fit the data well and were matched separately from the bottom thermocouple. Figures 3.20 and 3.21 show the matching profiles produced. For two gap sizes: 1.8 in. and 0.7 in., it is seen that the larger gap size matches the top three thermocouples and the smaller gap radius matches the bottom thermocouple. These values are significantly larger than that reported by Thurgood of 1/16 in.
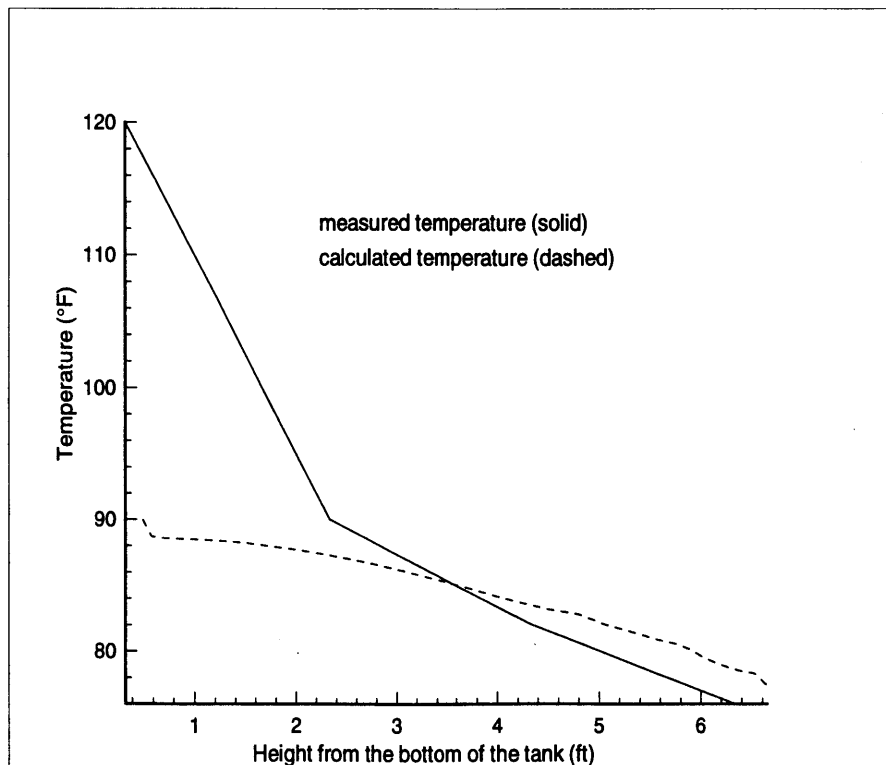
Figure 3.20: Comparison of measured and calculated temperature profiles at the center of the annulus matching TCPs 2-4 with the gap size = 1.8 in.
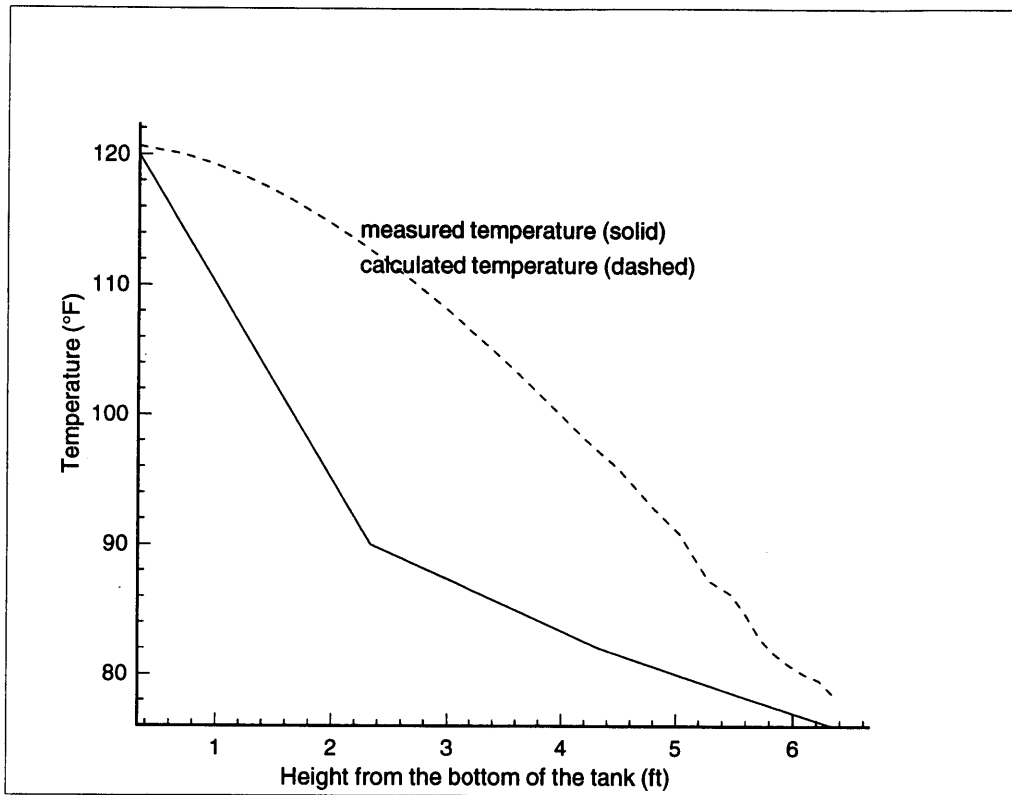
Figure 3.21: Comparison of measured and calculated temperature profiles at the center of the annulus matching TCP 1 with a gap size = 0.7in.

3.5.2 Temperature Suppression Due to Annulus

The second important result from the model is the radial distance in the sludge around the TC-14 which is affected by the annulus. The distance of radial effect is found by increasing the amount of sludge modeled (increasing the radius of the model until the temperature profile at the outer edge matches that of the tank section without an annulus, Model B). For the run matching TC-2 through TC-4, the amount of sludge modeled to achieve a true adiabatic outer edge was 18 feet. Figure 3.22 shows the temperature profile in comparison to that of Model B. Figure 3.23 shows the contours through the sludge including the estimated saturation temperature line (228 °F). The annulus then cools the sludge below the saturation temperature at a radius of 13 feet.
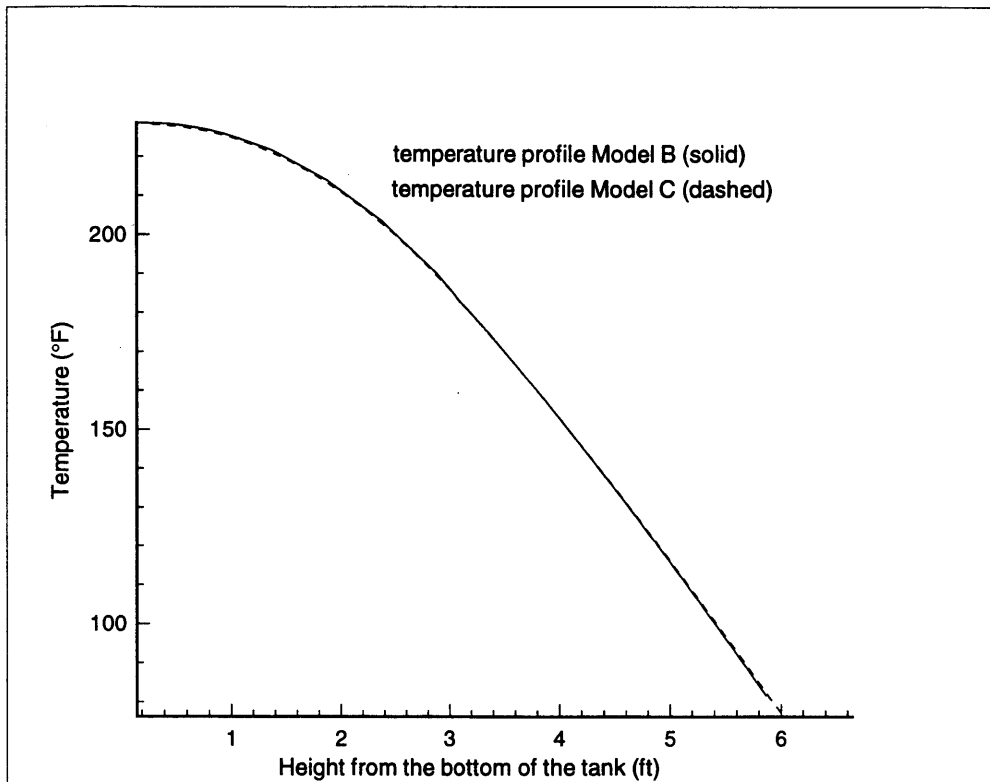
Figure 3.22: Comparison of boundary temperature to ensure correct adiabatic modeling for TCPs 2-4.
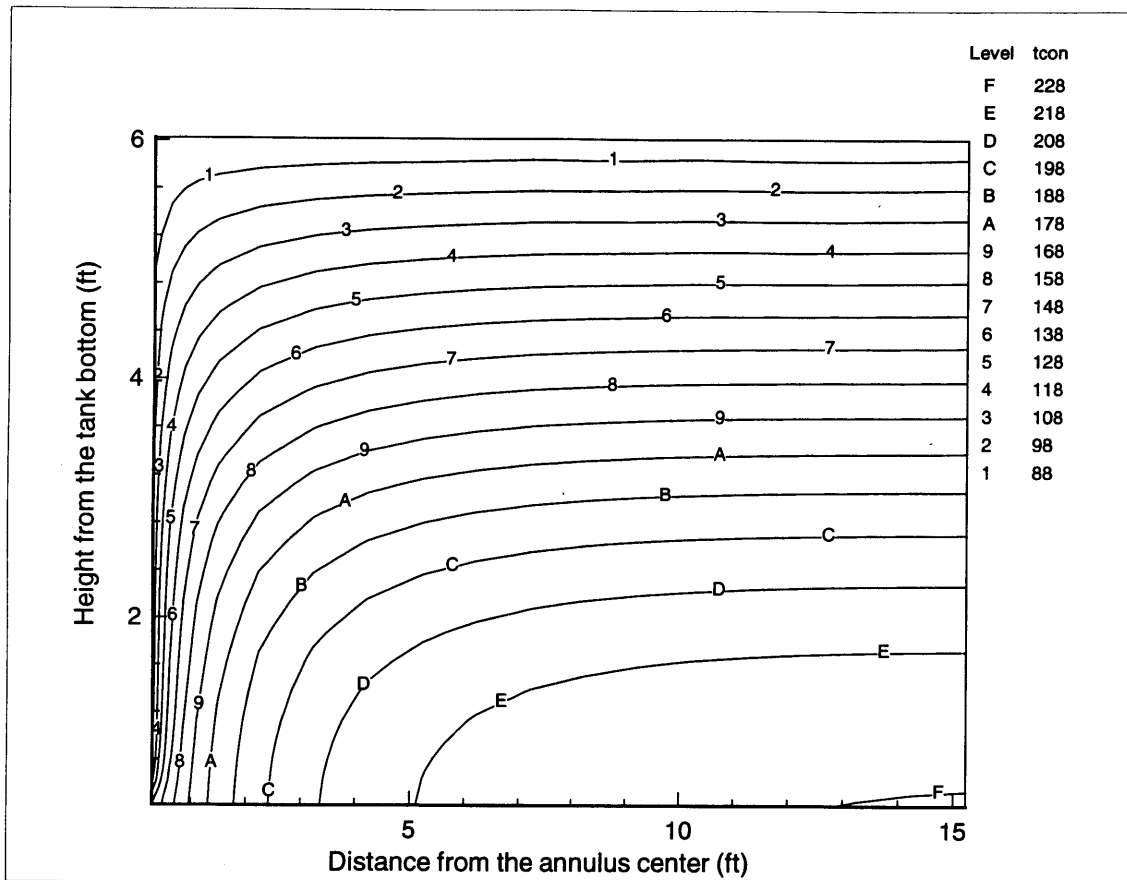
Figure 3.23: Temperature contours of sludge region indicating steam region suppression for TCPS 2-4 (°F).

Figures 3.24 and 3.25 are analogous to 3.22 and 3.23 but match the bottom thermocouple. In this case the radius of sludge cooled below the saturation temperature is 11 feet. The amount of sludge modeled to achieve the profile in Figure 3.24 was 16 feet.

3.5.3 Effect of Heat Generation Within the Annulus

Further investigations were done to match, in a single run, the calculations to all of the TC-14 readings. Results presented previously model the constant radius annulus with the heat generating sludge as an impermeable solid. The higher temperature reading at the lowest thermocouple is an indication that this model is not adequate in the lower region of the annulus. Two conditions which could increase this bottom temperature are heat
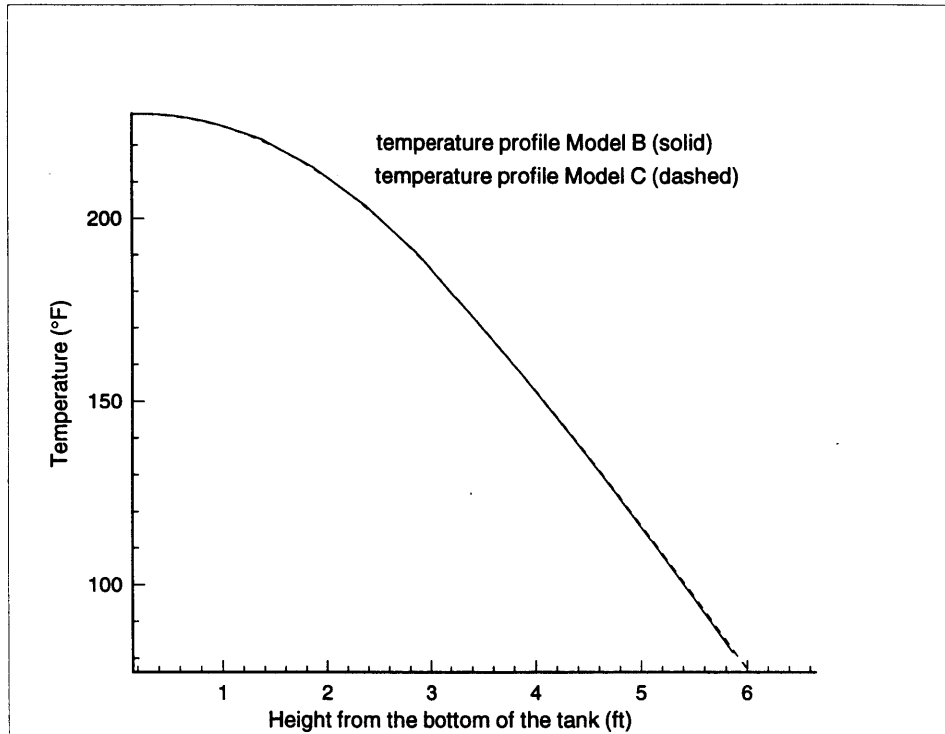
Figure 3.24: Comparison of boundary temperature to ensure correct adiabatic modeling for TCP 1.

generation within the annulus and an annulus whose radius varies with height.

The first condition, heat generation within the annulus, assumes that the lower portion has heat generating radioisotopes in concentrations equal to that in the adjacent sludge. Figure 3.26 shows the decrease in temperature caused by the increased buoyancy of added heat generation. The limited effect of this change, ~0.5 °F, is caused by the minimal increase in overall heat production in the region including and surrounding the annulus. Because of the limited effect and direction of this change, the modification was pursued no further.

3.5.4 Annulus Width Variation Along the Axis

Varying the width of the annulus in the axial direction provided a profile similar to that of all 4 submerged TCPs on TC-14. By iteration, the gap width for the bottom 0.5 ft was set at 0.18 in. and the gap width above was set to 2.0 in. to match measured data. The
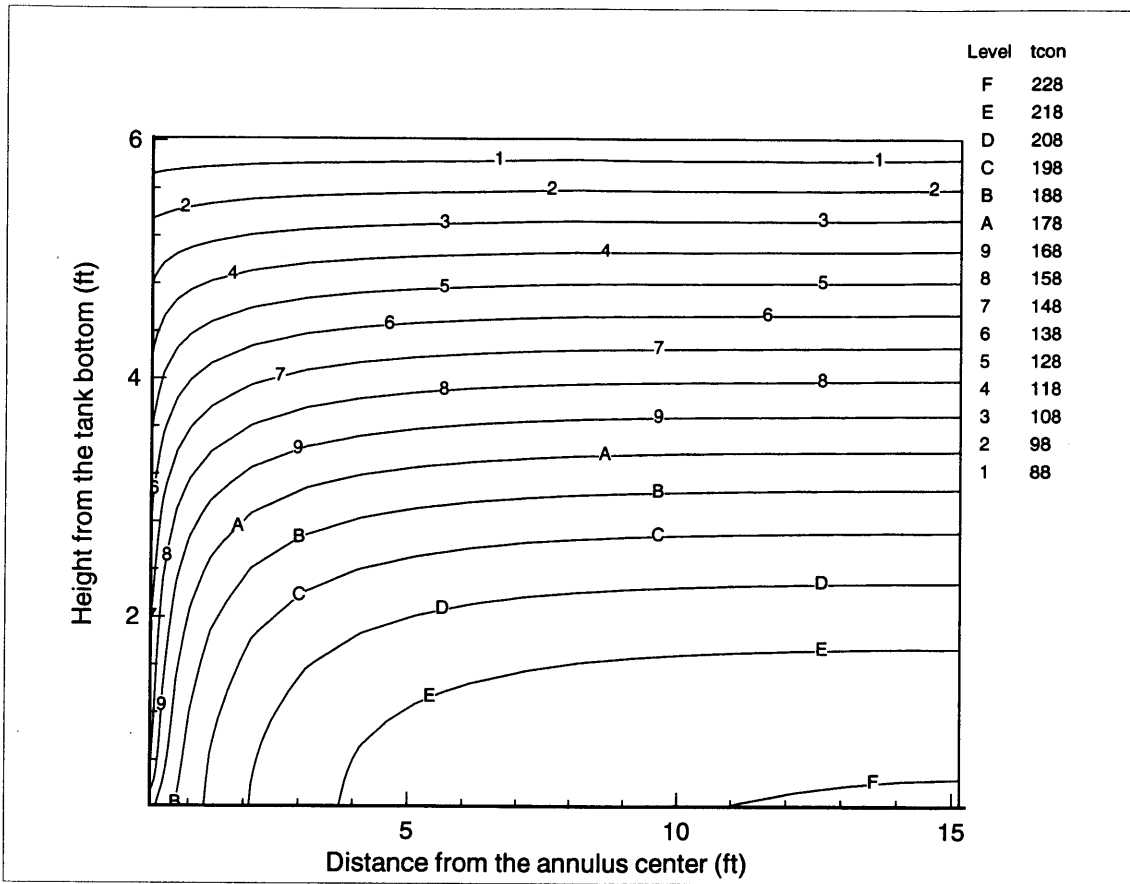
Figure 3.25: Temperature contours of sludge region indicating steam region suppression for TCP 1 (°F).

lower radius constricted flow enough to cause a temperature rise relative to the other temperatures at the inner radius of the annulus. Figure 3.27 shows the profile calculated against the TC-14 nominal data. The suppression of the steam region for this configuration is shown in Figure 3.28 as seen to be just over 12 ft.
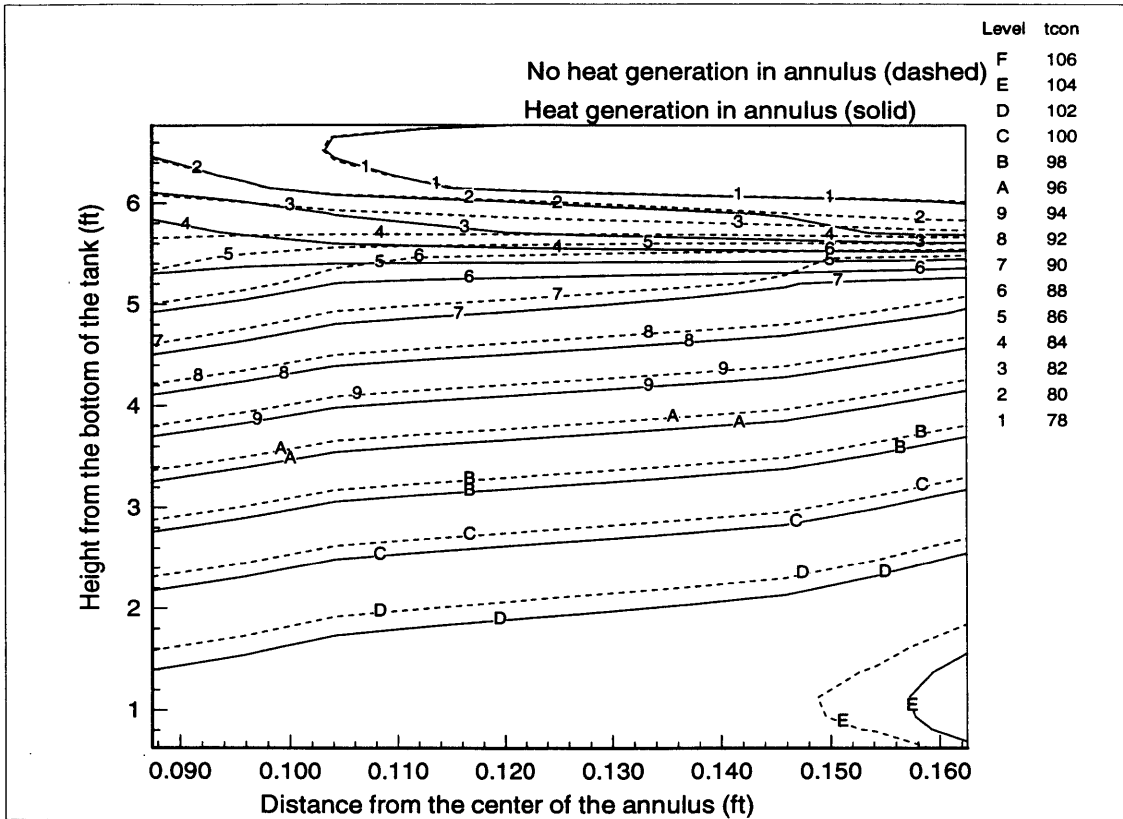
Figure 3.26: Comparison of annulus temperature contours with the addition of heat generation within the annulus (°F).
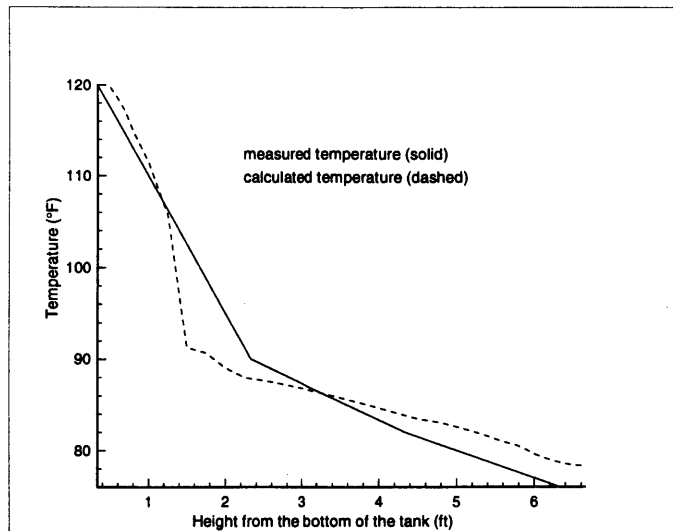
Figure 3.27: Calculated temperature profile for an annulus with an axially varying radius against the nominal measured temperature profile.
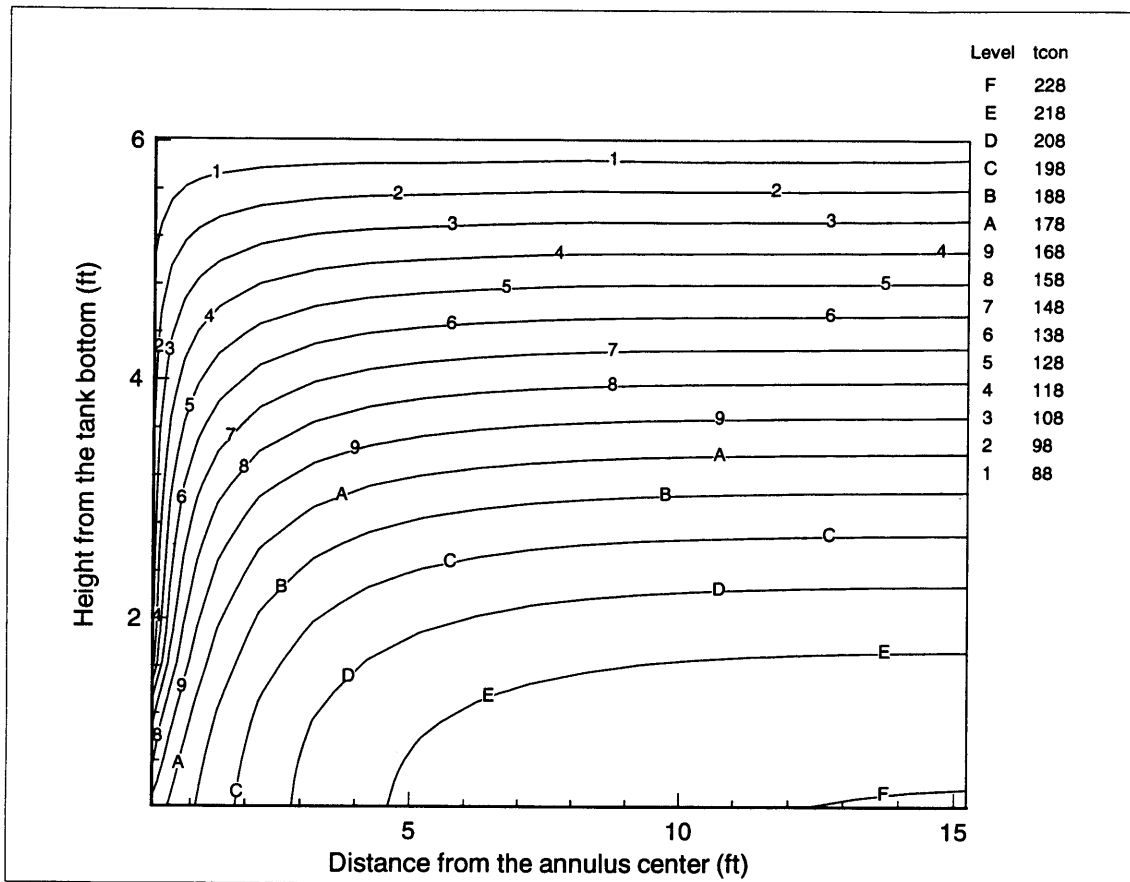
Figure 3.28: Resulting temperature contours in the adjacent sludge for an annulus with an axially varying radius(°F).

3.5.5 Effect of Reducing Overlying Layer Thickness

As mentioned earlier, the evaporation of the water in the tank serves as a major form of heat dissipation. Data shows the water level to vary between 3 and 9 inches due to evaporation and water refill. Results presented thus far, have only been for 9 inches of overlying water. During the majority of the time (after water addition the temperatures initially rise quickly), the temperature data shows a decrease in temperature for TC-14. One would expect, however, a lower liquid level to inhibit mixing at the top of the annulus and the annulus' effectiveness in transferring heat, causing an increase in temperature. Calculations using this model with 3 inches of overlying water show that the expectation is correct. Figures 3.29 and 3.30 show an increase of 2 °F in the annulus with temperatures

in the overlying fluid layer approaching temperatures found with 9 in thick fluid layer as the distance from the annulus increases. Therefore, this model does not explain the local heating and the increase of the TC-14 temperature readings which occur during water addition. Thus, we have used the lower temperature values from the monthly periodic measured data for determining the nominal temperature profile at the annulus center (see Section 3.4). For Figures 3.29 and 3.30, note that the plots directly overlap each other such that the simulation with 3 inches of overlying water cuts off approximately 6 inches below the simulation for 9 inches.
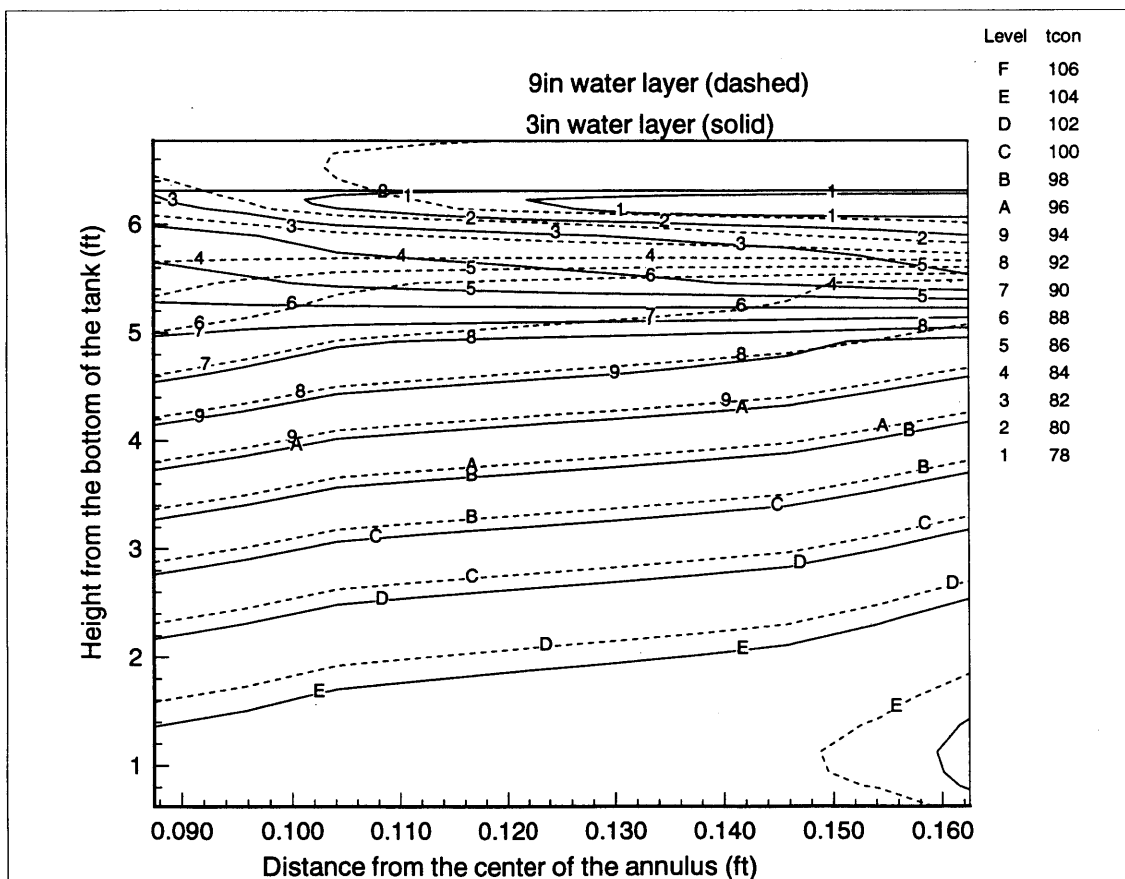
Figure 3.29: Change in temperature contours in the annulus for a reduced overlying fluid thickness from 9in to 3in.
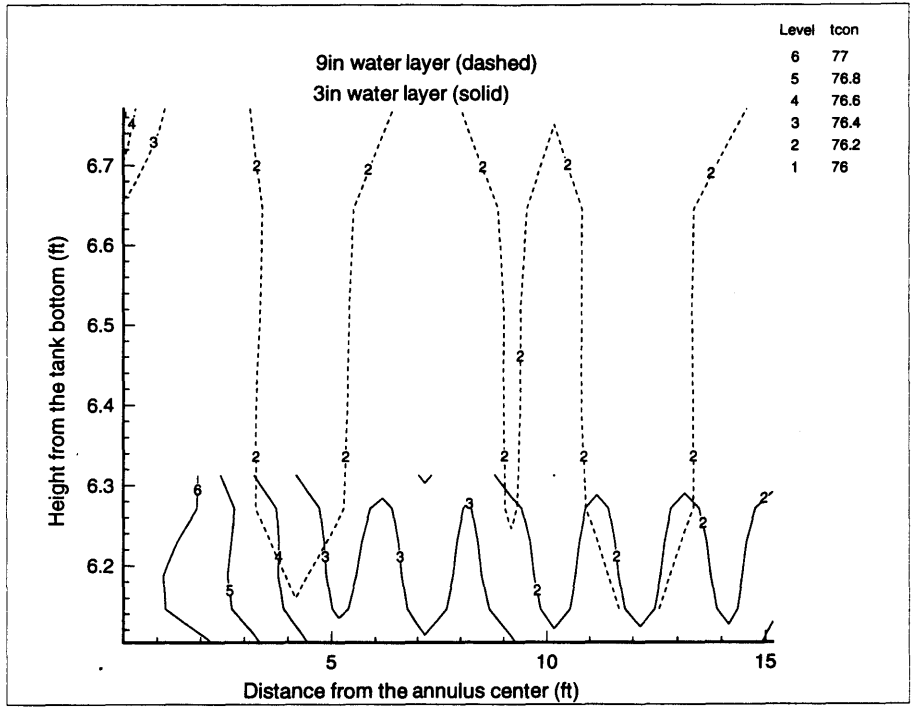
Figure 3.30: Change in temperature contours in the overlying fluid layer for a fluid thickness decrease from 9in to 3in.

Chapter 4

Summary and Conclusions

4.1 Results

4.1.1 The Potential for Natural Convection

Previous thermal modeling of Tank 241-C-106 includes only conductive heat transfer in the porous sludge. In considering the effects of fluid natural convection, this analysis includes two separate investigations. Fiirst chapter 2 establishes the potential for convection in the sludge considering various tank conditions. Beyond considering the sludge just as a porous medium, the discussion includes the effects on the onset of convection from both the fluid layer above the porous layer and the presence of a dissolved salt gradient. Finally an estimate of the convective to conductive heat transfer is made (by quantifying the Nusselt number) for tank conditions and properties which indicate the presence of convection.

A low and a high estimate of permeability are taken from literature describing Tank 241-C-106. The oscillations in the superposed fluid layer due to evaporation and water addition give the upper and lower bounds of the ratio of fluid to porous layer depths. Results of the high permeability case show that convection can exist, but they do not for the low permeability case. Considering the effect of the superposed fluid layer, computations show convection can exist for the entire range of permeabilities and range of depth ratios considered for the tank. Considering the salt gradient in a model for the porous region without an overlying fluid indicate convection would not exist. However, two factors are expected to affect this result. First, the solute gradient chosen was a linear gradient based on the overall salt concentration assuming no salt concentration at the top of the tank. Second, the superposed fluid layer would dominate the onset of convection as was shown in the absence of a salt gradient. Therefore it is expected that convection within the sludge does exist in Tank 241-C-106.

4.1.2 The Effect of Local Convective Cooling

In Chapter 3, the effects of local convection hypothesized to exist near thermocouple tree 14 was addressed. Previous analysis based on level data trends for Tank 241-C-106 and global thermal conduction modeling of the sludge conclude that a steam region may exist during summer. Local convection in an annulus around TC-14 is provided as an explanation for the temperature measurements not being at the saturation temperature. This region is modeled as a sludge-free annulus surrounding the thermocouple tree. Within the annulus, both convection and conduction are modeled, but in the sludge only conduction is modeled. This model allows comparison with previous studies to show the relative local effect of the annulus. Not allowing convection in the sludge results in a conservative estimate of the effect of local convection on reducing the hypothesized steam region.

Previous analysis assumed the effect of the annulus to be limited to within 6 feet or about 7% of the estimated steam region. (The actual region suppressed below the saturation temperature would be slightly less.) The more elaborate analysis of this thesis shows the radius of the region suppressed below the saturation temperature to be 12ft or 30% of the total steam region. Estimates of the size of the total region are based on model inputs provided by Thurgood who used water level data that indicated the presence of a steam region. The water level data was used by Thurgood to conclude a steam region might exist. The heat generation rate distribution and thermal conductivity were adjusted within reasonable parameters to determine the estimated steam region size. Assuming the estimate of such a void to be correct, the effect of the annulus, not considered when matching void to tank level data by Thurgood, would be to relocate the region of the void away from the TC-14 location. Because the void has a low aspect ratio it can be approximated as a 2-D disk near the bottom of the tank. A suppressed region of radius of 12 ft would change the necessitated steam region radius from approximately 24 ft to 26 ft. Note that TC-14 is not at the tank center, so that the region of suppression is not entirely within the steam region postulated to exist by Thurgood. If the size of the void postulated by Thurgood is correct, the effect of the annulus around TC-14 is to increase the outer radius of the steam zone while suppressing steam formation around TC-14. If the size

estimate is incorrent the local effect of convection around TC-14 is to reduce the steam region by 30%. These new steam region configurations should be kept in mind for intrusion activities to remove pumps, take core samples or otherwise disturb the sludge beyond normal operating conditions. On the other hand, because the conclusion of a steam region was based on the level data change with time and because no transient analysis of the tank was performed, we can neither confirm nor deny the presence of the steam region.

The presence of convection implies the water to be a greater contributor to heat transfer than would be true for a pure conductive analysis. Therefore the effects of waste dryout and computed maximum temperature should be recomputed taking into account both the reduction in conduction and convection before drainable liquid is removed.

4.2 Future Work

4.2.1 Data Analysis

The tank data includes two thermocouple trees and a level measurement. This data is insufficient to ascertain or negate the hypothesis of global convection. Because TC-14 is affected by local conditions, TC-8 should be used to compare global computer modeling of the sludge by including both convection and conduction. Previous modeling on this subject [12] implies that the profile measured by TC-8 reflects the presence of convection. Therefore a global model of convection and conduction in the sludge should be used to compare temperatures calculated against those measured. In addition the Nusselt number from the simulation should be compared to that calculated in Section 2.3. Convection characteristics from this simulation may also be used to improve upon the results on the annulus study of Chapter 3.

The introduction listed three unexplained characteristics in the data: lower temperatures at positions closer to the tank center, reduction in water level drop immediately following water addition, and an increase in temperatures following water addition. The first is explained by the analysis presented in Chapter 3. The second two may be explained by an analysis which extends the global model that combined convection and conduction to obtain a detailed map with the water temperatures. Because

the second two anomalies are functions of time, this analysis must consider the temporal effects. Oscillations in evaporation rates for the diurnal cycle are known to be four times greater than that of the seasonal cycle. Evaluation of the time response of the sludge modeled with convection must be used to decide the significance of the diurnal cycle. The analysis should model the effects of convection and conduction in the sludge, convection, conduction, and radiation in the dome air space, the phase change at the interface, and conduction in the exterior soil surrounding the tank.

As noted in Chapter 2, the increase in temperature following water addition may be caused by the suppression of convection due to a change in the dissolved salt gradient. That is fresh water is added to the top of the tank. As salt diffuses up, it creates a gradient in the layer below. After sufficient time the tank contents are well mixed due to convection, reducing the salt gradient, enhancing the convection and allowing temperature to decrease as stored heat is released. The period of this diffusion and trapping of heat in comparison to the 10-15 day observance of temperature increase should be checked to establish the validity of this theory. Because the convection and conduction in the sludge are in series with the evaporation for removing the majority of the generated heat (>70% by most published literature), the reduction in convection would cause reduction in the evaporation level. The necessity to supply sensible heat to the added water would also slow evaporation. Reductions in the heat transfer mechanisms would cause heating of the sludge following water addition, the third anomaly. Increasing the temperature as well would be the heat of dissolution evolved from reducing the concentrations of the salts by adding fresh water. Increased temperatures in the sludge would also suppress evaporation so the heating effects feed each other until diffusion and convection homogenize the salt concentration.

4.2.2 Data Collection

Better understanding of the tank would be aided greatly by increased and expanded data taking efforts. More frequent monitoring of temperatures and level data would provide a better indication of model validity for the diurnal cycle. Psychometric measurement of the inlet and outlet air could be used to evaluate the evaporation rate. A

core sample could provide an axial profile of particle diameter, porosity, and chemical composition. The chemical composition would indicate both salt concentration and heat generation as a function of height. This information would also help determine if the steam region is composed of numerous small bubbles or fewer larger bubbles which might have a greater potential to develop into a steam bump. Finally determining the presence of a steam region could be more easily determined by inserting thermocouples into different sections of the sludge.

Appendix A Tank Measurement Data

The following appendix gives the level and temperature data measured for Tank 241-C-106.

A.1 Level Sensor Data
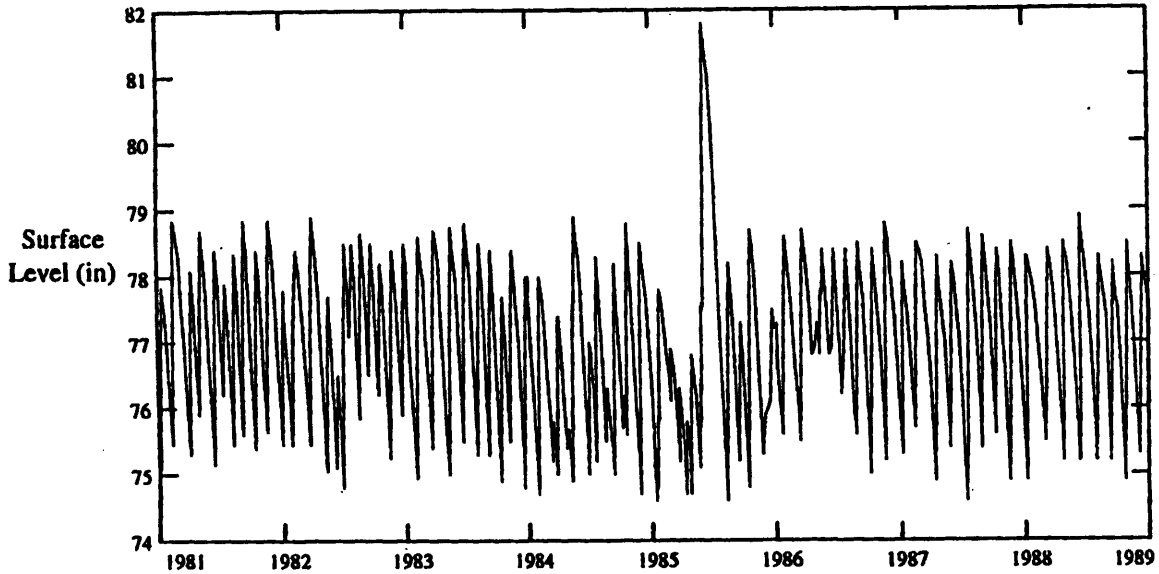
Figure A.1: Historical Surface Level Data (1981 through 1988) [7]
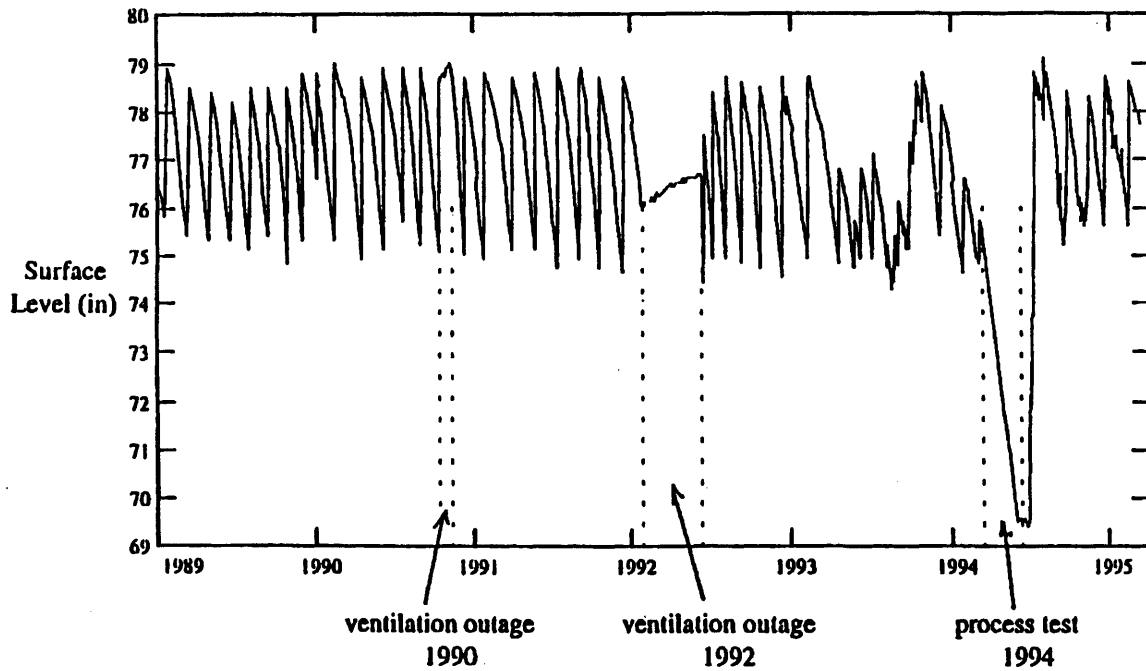
Figure A.2: Historical Surface Level Data (1989 through February 1995) [7]

A.2 Thermocouple Tree 8 Data
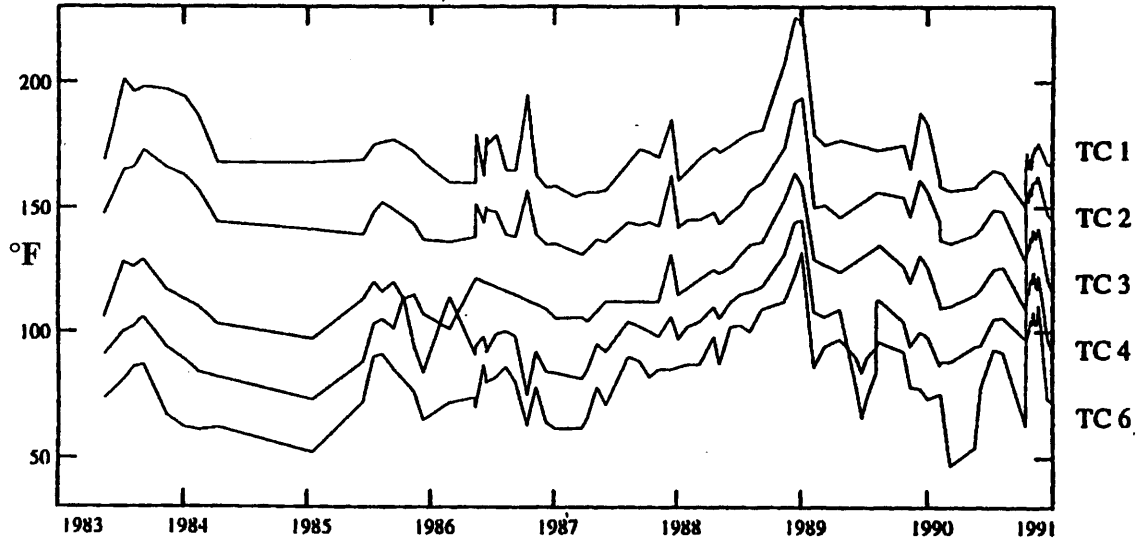
Figure A.3: Measured Temperatures for Tank 241-C-106 TC-8 (1983 through 1991) [7]
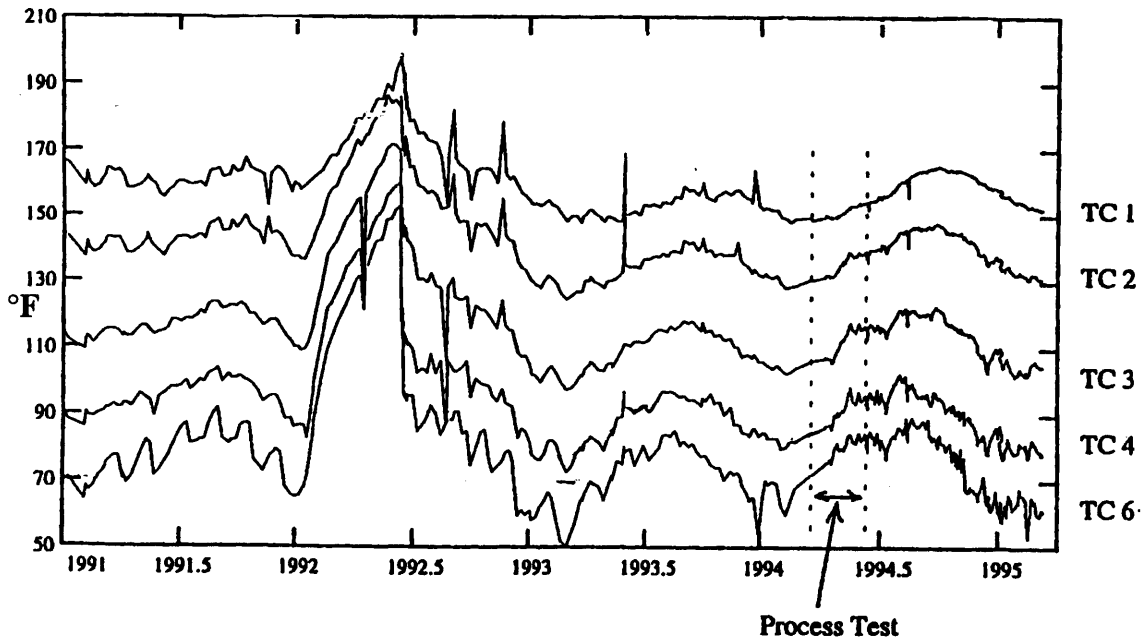
Figure A.4: Measured Temperatures for Tank 241-C-106 TC-8 (1991 through February 1995) [7]

A.3 Thermocouple Tree 14 Data
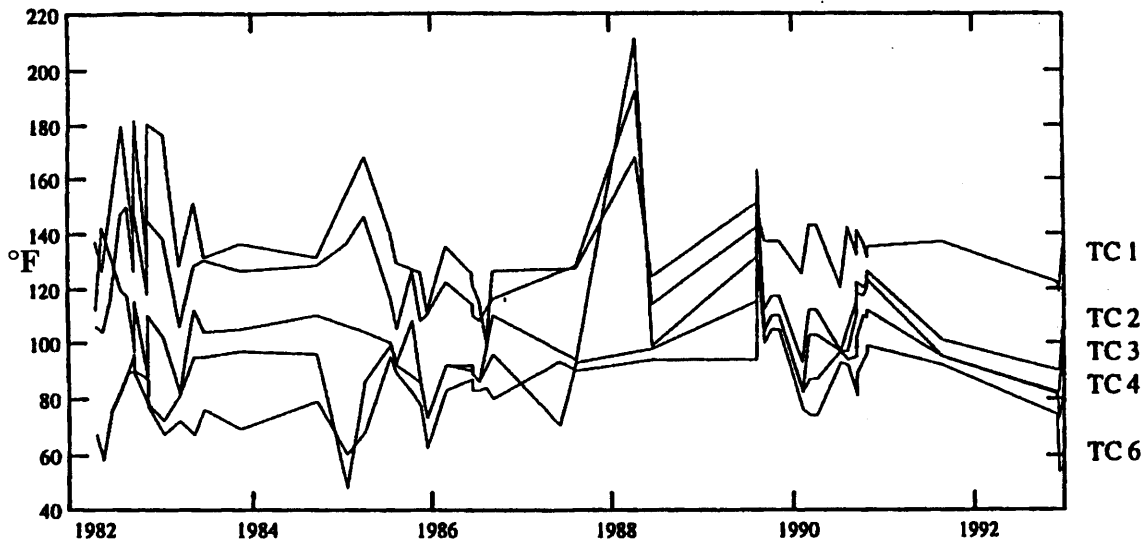
Figure A.5: Measured Temperatures for Tank 241-C-106 TC-14 (1982 through 1992) [7]
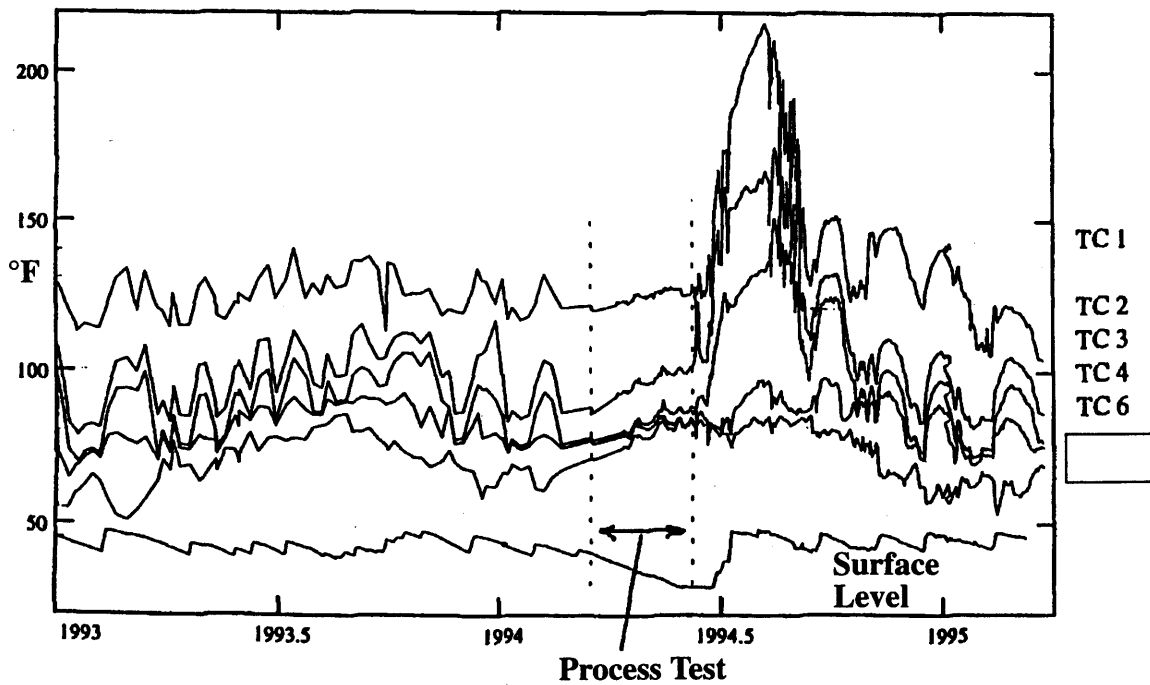
Figure A.6: Measured Temperatures for Tank 241-C-106 TC-14 (1993 through Feb. 1995)[7]

Appendix B

Errors Found in Numerical Procedure for Superposed Porous Region with Internal Heat Generation

B.1 Introduction

The theory and analytical solution presented by Somerton and Catton [26,27] is correct. The graphs presented based on the calculations from the numerical procedure described in the paper has errors. These errors do not effect the results for high and low η so that the comparison with individual fluid region and porous region data matched despite the error. Further, trends presented are also correct because of the nature of the error. The author identified two works which referenced the data of Somerton [26,27], the article by Prasad [47] giving an overview on superposed porous region convection work and Catton's [24] article describing the computation of heat transfer beyond the onset of convection. Though both referenced figures with incorrect numbers, the conclusions drawn on the basis of trends remained valid.

B.2 Description of Mistakes

The mistakes found in the numerical procedure used for generating critical Rayleigh numbers using the Galerkin technique were twofold, analytical and computational. First the method requires the energy equation, including both the velocity and temperature Fourier expansions, to be multiplied by $\sin(n\pi Z)$ and integrated over the region of interest. This resulted in numerous integrals one of which was

$$\int_{-\frac{1}{1+\eta}}^{0} Z\sin{(aZ)}\cos{(bZ)} \qquad\qquad\text{(B.1)}$$

The analytical solution to this integral had a sign error.

The second error was a coding error in which counting integers were used in calculations. In Fortran 77, such calculations can have errors because after each step of the calculation the result is truncated to an integer as dictated by the variable type. Because this mistake was done in the dominant term of a summation for an element on the main diagonal of a positive definite matrix, the truncation caused errors as great as an order of magnitude for the critical Rayleigh number.

B.3 Examples of Corrected Data

The impact of these two mistakes was not analyzed separately. The author used a Matlab code to repeat the numerical procedure. Two codes were written. The first, referred to as Code A, has the correct numerical procedure. The second, referred to as Code B, has the same mistakes as the Fortran code generated by Somerton. Table B.1 lists the test cases which compare the three codes. Table B.2 lists the two variables used for comparison, the internal and universal Rayleigh number, R_I and R_U, respectively. Both are compared for the three codes. For a given η, γ, and Da, the R_U should be the same regardless of the input R_E. As noted in the main text the external Rayleigh number, R_E, is given as

$$R_E = \frac{g\beta\Delta T L^3}{\upsilon_f \alpha_f}, \qquad\qquad\text{(B.2)}$$

and R_I is given as

$$R_I = \frac{g\beta Q_v L^5}{\upsilon_f \alpha_f k_m^2}, \qquad\qquad\text{(B.3)}$$

104

in which both are used to compute R_U,

$$R_U = \frac{\eta^4}{(1+\eta)^5(\gamma+\eta)} \cdot \left[R_E \cdot (1+\eta)^2 + R_I \right] .$$

(B.4)

Table B.1: Data Sets Used to Test New Numerical Procedure

Case (#)	Da	η	γ	R_E
1	$3.775*10^{-4}$	$1*10^{-5}$	0.5	0
2	$3.775*10^{-4}$	$1*10^{-5}$	10	0
3	$3.775*10^{-4}$	$1*10^{-5}$	10	$2.096*10^3$
4	$3.775*10^{-4}$	$5.75*10^{-2}$	1	10
5	$3.775*10^{-4}$	$5.75*10^{-2}$	1	1e4
6	$3.775*10^{-4}$	1	1	0
7	$3.775*10^{-4}$	1	5	0
8	$3.775*10^{-4}$	1	10	0
9	$3.775*10^{-4}$	1	1	$3.1616*10^4$
10	$3.775*10^{-4}$	1	1	$3.1616*10^2$
11	$3.775*10^{-4}$	1	5	0
12	$3.775*10^{-4}$	1	10	$2.493*10^3$
13	$3.775*10^{-4}$	1	10	0
14	$3.775*10^{-4}$	1	10	$1.493*10^3$
15	$3.775*10^{-4}$	2	5	0
16	$2*10^{-3}$	2	5	$4405*10^3$
17	$2*10^{-3}$	2	5	$1405*10^3$
18	$2*10^{-3}$	$5.75*10^{-2}$	0.5	0
19	$2*10^{-3}$	$5.75*10^{-2}$	1	0
20	$2*10^{-3}$	1	5	0
21	$2*10^{-3}$	1	10	0
22	1	2	10	0

Table B.2: Comparison of Results for Matlab Code A, Matlab Code B, and Somerton Data

#	R_I			R_U		
	Matlab Code A	Matlab Code B	Somerton Code	Matlab Code A	Matlab Code B	Somerton Code
1	$7.226*10^4$	$7.8323*10^4$	$7.8179*10^4$	$1.189*10^3$	$1.2892*10^3$	$1.2870*10^3$
2	$2.551*10^5$	$2.5463*10^5$	$2.5463*10^5$	$1.583*10^3$	$1.581*10^3$	$1.581*10^3$
3	$1.480*10^3$	$1.0119*10^3$	$1.0000*10^3$	$1.583*10^3$	$1.581*10^3$	$1.581*10^3$
4	$4.717*10^4$	$5.1218*10^4$	$5.1219*10^4$	$1.395*10^3$	$1.5147*10^3$	$1.515*10^3$
5	$7.18*10^4$	$1.1323*10^4$	$1.1325*10^4$	$1.394*10^3$	$1.5166*10^3$	$1.517*10^3$
6	$7.225*10^5$	$1.2746*10^5$	$1.2746*10^5$	$1.129*10^3$	$1.9916*10^3$	$1.992*10^3$
7	$1.060*10^5$	$1.3020*10^5$	$1.3023*10^5$	$1.419*10^3$	$1.739*10^3$	$1.741*10^3$
8	$2.634*10^5$	$3.0274*10^5$	$3.0270*10^5$	$1.487*10^3$	$1.710*10^3$	$1.708*10^3$
9	-	$1.4387*10^3$	$1.4390*10^3$	-	$1.9985*10^3$	$1.999*10^3$
10	$7.095*10^4$	-	-	$1.128*10^3$	-	-
11	$1.0458*10^5$	$1.3023*10^5$	$1.3023*10^5$	$1.883*10^3$	$1.7446*10^3$	$1.745*10^3$
12	-	$1.3892*10^3$	$1.3390*10^3$	-	$1.7106*10^3$	$1.711*10^3$
13	$2.634*10^5$	-	-	$1.485*10^3$	-	-
14	$8.260*10^4$	-	-	$1.485*10^3$	-	-
15	$1.1579*10^5$	$1.5957*10^5$	$1.5956*10^5$	$1.329*10^3$	$1.8322*10^3$	$1.832*10^3$
16	-	$1.5832*10^3$	$1.5990*10^3$	-	$1.8390*10^3$	$1.839*10^3$
17	$6.497*10^4$	-	-	$1.128*10^3$	-	-
18	$5.907*10^4$	$6.5315*10^4$	$6.5318*10^4$	$8.720*10^2$	$9.6426*10^2$	$9.640*10^2$
19	$3.605*10^4$	$3.9347*10^4$	$3.9348*10^4$	$1.065*10^3$	$1.1627*10^3$	$1.163*10^3$
20	$8.998*10^4$	$1.1642*10^5$	$1.1642*10^5$	$1.205*10^3$	$1.5596*10^3$	$1.560*10^3$
21	$2.3839*10^5$	$2.7896*10^5$	$2.7896*10^5$	$1.345*10^3$	$1.5747*10^3$	$1.575*10^3$
22	$2.1403*10^5$	$2.8303*10^5$	$2.8300*10^5$	$1.107*10^3$	$1.4650*10^3$	$1.465*10^3$

Using figures and data from Somerton's thesis [26] and interpolating from Cases 6-8 above, one can generate the following figure, Figure B.1, which shows the increase in predicted critical internal Rayleigh due to the errors.
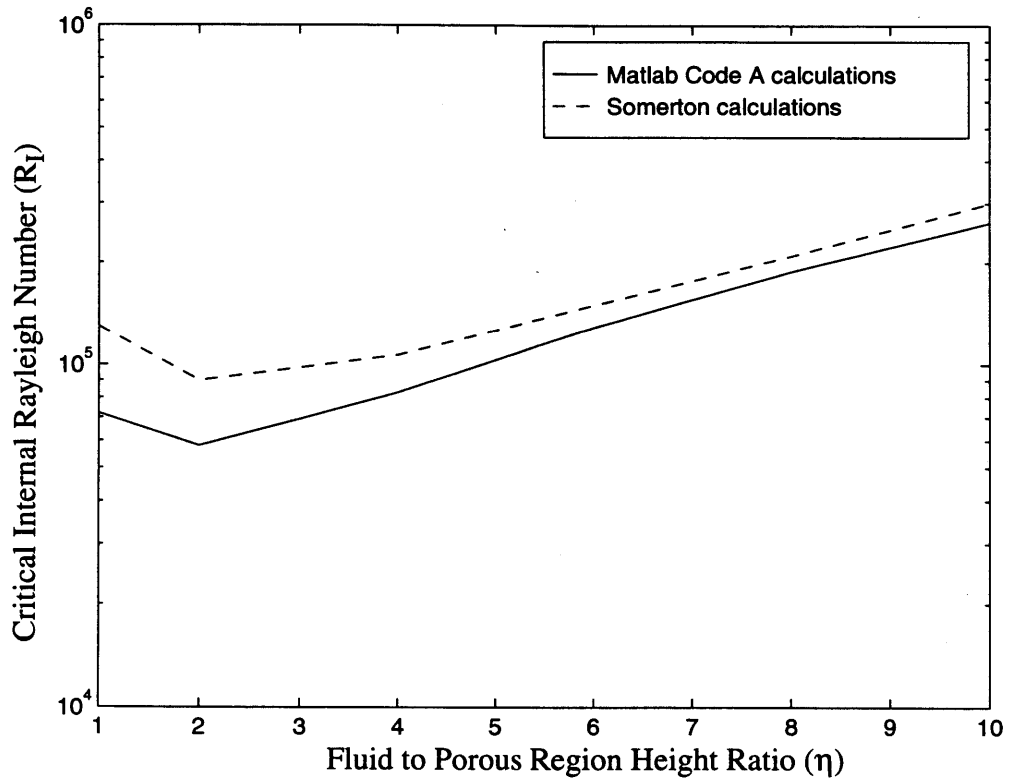
Figure B.1: Comparison of Somerton and Matlab Code A Calculations (Da=3.775*10^4, γ=1, R_E=0)

Appendix C

Onset of Convection for Small Darcy Number in Super-posed Porous and Fluid Layers

C.1 Introduction

The methods for solving the analytical problem of the onset of convection for an internally heated porous layer superposed by a fluid layer was solved by Somerton and Catton [26,27]. The solution provided, however, had a lower limit of the Darcy number of $3.775*10^{-4}$. This appendix outlines the procedure for finding the onset of convection for Darcy numbers below this limit. Secondly, in explicitly explaining the steps taken, the Galerkin technique used to find this stability limit will be explained in more detail.

C.2 Restrictions of Limiting Darcy Number

The limitation of a Darcy value of $3.775*10^{-4}$ corresponds to a D_p/L value of

$$\frac{D_p}{L} = \sqrt{Da\frac{175\,(1-\varepsilon)^2}{\varepsilon^3}} = 0.36,$$

for $\varepsilon=0.50$ by rearranging equations presented in Chapter 2. Physically then the method may only be applied to layers of combined porous and fluid regions which do not exceed 3 times the particle diameter of the porous region. Clearly, for common applications of this model including geothermal sources, nuclear reactor severe accidents, solar packed bed thermal storage, solidification of concentrated alloys, porous journal bearings, and waste tanks such a ratio is rarely found [47].

Somerton outlines a procedure for solving the equations for low Darcy number, but the solution treats the porous region as a solid wall without velocity. This solution then does

not model the porous region velocity distribution, the number of convection cells, or the effect of permeability for low depth ratios, η.

C.3 Method of Solution

In solving the nondimensionalized momentum and energy equations for both regions found in Section 2.2,

$$(D^2 - a^2)^2 W_1 = a^2 \Theta_1, \tag{C.1}$$

$$(D^2 - a^2) \Theta_1 = \frac{-W_1}{(\eta + \gamma)(\eta + 1)} \left[R_E(1 + \eta)^2 + \frac{1}{2}R_I \right], \tag{C.2}$$

$$(D^2 - a^2)^2 W_2 - \frac{1}{Da}(D^2 - a^2) W_2 = a^2 \Theta_2, \tag{C.3}$$

$$(D^2 - a^2) \Theta_2 = -W_2 \left\{ \frac{1}{(\eta + \gamma)(\eta + 1)} \left[R_E(1 + \eta)^2 + \frac{1}{2}R_I \right] + Z\gamma R_I \right\}, \tag{C.4}$$

with the Galerkin the method, one uses Fourier series expansions for temperature

$$\Theta_1 = \frac{1}{a^2} \left(\sum_K A_{K,c} \cos(\alpha_{1,K} Z) + \sum_K A_{K,s} \sin(\beta_{1,K} Z) \right), \tag{C.5}$$

$$\Theta_2 = \frac{1}{a^2} \left(\sum_K A_{K,c} \cos(\alpha_{2,K} Z) + \frac{\gamma}{\eta} \sum_K A_{K,s} \sin(\beta_{2,K} Z) \right), \tag{C.6}$$

where

$$\alpha_{1,K} = \frac{2K-1}{2} \pi \frac{1+\eta}{\eta}, \tag{C.7}$$

$$\beta_{1,K} = K\pi \frac{1+\eta}{\eta}, \tag{C.8}$$

$$\alpha_{2,K} = \eta \alpha_{1,K}, \tag{C.9}$$

$$\beta_{2,K} = \eta \beta_{1,K}, \tag{C.10}$$

which solves the temperature boundary and coupling conditions. Plugging these into the momentum equations, C.1 and C.3, gives the particular solutions of velocity as

$$W_{1,P} = \sum_K A_{K,c} \frac{\cos(\alpha_{1,K}Z)}{((\alpha_{1,K})^2 + a^2)^2} + \sum_K A_{K,s} \frac{\sin(\beta_{1,K}Z)}{((\beta_{1,K})^2 + a^2)^2}, \qquad (C.11)$$

$$W_{2,P} = \sum_K A_{K,c} \frac{\cos(\alpha_{2,K}Z)}{((\alpha_{2,K})^2 + a^2)^2} + \sum_K A_{K,s} \frac{\sin(\beta_{2,K}Z)}{((\beta_{2,K})^2 + a^2)^2}. \qquad (C.12)$$

The homogeneous solutions of velocity are given as (for the cosine portion):

$$W_{1,H,c} = B_{K,1,c}\cosh(aZ) + C_{K,1,c}Z\cosh(aZ) + D_{K,1,c}\sinh(aZ) + E_{K,1,c}Z\sinh(aZ), \qquad (C.13)$$

$$W_{2,H,c} = B_{K,2,c}\cosh(b1 \cdot Z) + C_{K,2,c}\cosh(b2 \cdot Z) + D_{K,2,c}\sinh(b1 \cdot Z) + E_{K,2,c}\sinh(b2 \cdot Z), \qquad (C.14)$$

where

$$b1 = a, \qquad (C.15)$$

$$b2 = \sqrt{a^2 + \frac{L^2}{P}}. \qquad (C.16)$$

An analogous set can be written for the sine portion of velocity. These 16 coefficients, $B_{K,1,c} - E_{K,2,c}$, (8 cosine terms, 8 sine terms) are solved using the 8 velocity boundary conditions and coupling conditions (see Chapter 2). These conditions are applied to both cosine and sine homogeneous solutions to generate 16 equations. The two systems of 8 equations and 8 unknowns cannot feasibly be computed symbolically.

It is these homogeneous terms where the computation problem occurs for region 2. The homogenous velocity solutions of region 2 have the expressions $\cosh(b2 \cdot Z)$ and $\sinh(b2 \cdot Z)$ where b2 is on the order of the square root of the inverse of the Darcy number for the porous region, a large number (see eqn. C.16). For b2 beyond around 700, these expressions cannot be computed by a PC.

To simplify expressions for determining limits, the author solved the homogeneous solutions of $W_{2,H,c}$ and $W_{2,H,s}$ in exponential terms instead of hyperbolic terms giving the cosine and sine reformulations for region 2 as:

$$W_{2,H,c} = B_{K,2,c}\exp(b1 \cdot Z) + C_{K,2,c}\exp(-b1 \cdot Z) + D_{K,2,c}\exp(b2 \cdot Z) + E_{K,2,c}\exp(-b2 \cdot Z) , \quad \text{(C.17)}$$

$$W_{2,H,s} = B_{K,2,s}\exp(b1 \cdot Z) + C_{K,2,s}\exp(-b1 \cdot Z) + D_{K,2,s}\exp(b2 \cdot Z) + E_{K,2,s}\exp(-b2 \cdot Z) , \quad \text{(C.18)}$$

and computed the coefficients based on the matrix generated by applying the velocity boundary and coupling conditions. Because the $\exp(\pm b2 \cdot Z)$ terms are still incomputable these terms are left symbolic. 12 of the 16 coefficients can be solved by taking the limit of the expression for the coefficients:

$$\lim_{b2 \to \infty} \frac{G\exp(b2L_P) + N\exp(-b2L_P) + O}{J\exp(b2L_P) + Q\exp(-b2L_P) + I} = \frac{G}{J} \quad \text{(C.19)}$$

These homogeneous expressions for the coefficients are found from applying Kramer's rule to the matrix. The remaining four coefficients are found in the next step in solving these equations

The energy equation is the last to be satisfied. Inserting the expressions for temperature and velocity, equations C.5,C.6, C.11,C.12, C.17,C.18 as well as the analogous sine terms, into the energy equation and integrating the terms by $\sin(n\pi Z)$ where n is the number of terms in the Fourier series expansion gives a 2n*2n matrix,

$$\overline{\overline{M}} \cdot \overline{A} = 0, \quad \text{(C.20)}$$

where A is the coefficient vector. The resulting integrals

$$\int_{-\frac{1}{1+\eta}}^{0} \sin(n\pi Z)\exp(\pm b2 \cdot Z)\,dz \quad \text{(C.21)}$$

are multiplied by the coefficients of the homogeneous terms. The remaining 4 undetermined coefficients, $D_{K,2,c}$, $E_{K,2,c}$, $D_{K,2,s}$ and $E_{K,2,s}$, are multiplied by their respective integrals of the form C.21, resulting in equations and limits of the form of equation C.19. In all limits, the expressions yield a finite nonzero solution.

After determining the universal Rayleigh number, the matrix is fully determined. Using eqn. C.20 determines the Fourier series expansion coefficients to within a constant. A similar method is used for computing the profiles of velocity. Because the velocity is

computed over a range of Z from 0 to $-1/(\eta+1)$, however, the computation of $D_{K,2}$ $\exp(b2Z)$ and $E_{K,2}\exp(-b2Z)$, is only significant for Z near 0 for the former expression and Z near $-1/(1+\eta)$ for the latter expression.

C.4 Method Validation

The accuracy of this extension of Somerton's method is checked against experimental data and trends observed in the literature. The only experimental data found for internally heated porous region superposed by a fluid layer giving the onset of the convection is that of Sun[16]. Rhee [48] and Cherng [49] provide data only at convection conditions beyond critical. Sun's data is compared against calculations in Table C.1.

Table C.1: Comparison of Sun's Results With Extended Somerton Results
$(Da=1.15*10^{-5}, \gamma=.0662)$

η	Sun's Data R_E,cr	Extended Somerton Calculations R_E,cr
0.10	$2.8*10^6$	$1.2*10^7$
0.13	$2.4*10^6$	$2.1*10^6$

The second method for checking validity is in three trends, the effect on R_U by Darcy number, Da, the effect of depth ratio, η, on critical wave number, a, and the effect of η on the number of convection cells. For this extended method the universal Rayleigh number, R_U, approaches 1700 as Da decreases. This trend is present in previous results of Somerton [26], Taslim and Narusawa [50], and Rudraiah [51]. As fluid ratio decreases, wave number increases, which is seen in the data of Taslim and Narusawa [50] and Chen and Chen [34]. Finally, as η and Da decrease, the number of convective cells increases. No experimental data was found which combined both low Da, low η, and convection cell observations. The trend observed in the calculations follows that set out by Somerton's previous analysis which showed the number of convection cells to double as Da and/or η decreases.

References

[1] National Research Council. Panel on Hanford Wastes, "Radioactive Wastes at the Hanford Reservation: A Technical Review," National Academy of Sciences, Washington, D.C., 1978.

[2] Farris, T. Napier, B. A., and Simpson, T.C., "Columbia River Pathway Dosimetry Report 1949-92," Pacific National Laboratory, Richland, WA, April 1994.

[3] Ikenberry, T. A., Simpson, J.C., Shipler, D.B., "Atmospheric Pathway Dosimetry Report, 1944-1992," Pacific National Laboratory, Richland, WA, April 1994.

[4] Trabalka, John R., Auerbach, and Stanley I., "One Western Perspective of the 1957 Soviet Nuclear Accident," *Seminar on the Comparative Assessment of the Environmental Impact of Radionuclides Released During Three Major Nuclear Accidents: Kyshtym, Windscale, Chernobyl. Vol.1*. Luxembourg, 1990 pp. 41-70.

[5] Hanlon, B. M., "Tank Farm Surveillance and Waste Status Summary Report for January 1994," WHC-EP-WM-0182-70, Westinghouse Hanford Company, Richland, Washington, May 1994.

[6] Thurgood, M. J., Fryer, B. C., Ogden, D. M., Sathyanarayana, K., "GOTH, Tank C-106 Thermal Hydraulics Analysis Related to the 1994 Process Test," NAI-940708-3, Issued by Numerical Applications, Inc., for the Westinghouse Hanford Company, Richland, Washington, March 6, 1995.

[7] Bander, T. J., "Tank 241-C-106 Process Test Report," WHC-SD-WM-ER-427, Rev.0, Westinghouse Hanford Company, Richland, Washington, May 30, 1995.

[8] Bander, T.J., "Radial Variation of Thermal Conductivity and Heat Generation," WHC-SD-WM-ER-217, Rev. 0, Westinghouse Hanford Company, Richland, Washington, September 13, 1993

[9] Bander, T. J., "Tank 241-C-106 Parametric Studies in Support of Safety Alternative Process," WHC-SD-WM-ER-290, Rev.0, Westinghouse Hanford Company, Richland, Washington, November 12, 1993.

[10] Reid, H. C. and Eyler, L. L., "Thermal Property Assessment of Tank 241-C-106," HCR-002, Pacific Northwest Labs, Rev.1, 1994.

[11] Barrington, C.A., "C-106 Seasonal Evaporation Rate Correlations," Safety Fluid Mechanics and Computational Center, Westinghouse Hanford Company, Richland, Washington, February 17, 1995.

[12] McGrail, B. P., Trent, D. S., Terrones, G., Hudson, J. D., Michener, T. E., "Computational Analysis of Fluid Flow and Zonal Depositionin Ferrocyanide Single-Shell Tanks," PNL-8876, Pacific Northwest Laboratory, Richland, Washington, October 1993.

[13] Piepho, M. G., "Preliminary Analysis of Tank 241-C-106 Dryout Due to Large Postulated Leak and Vaporization," WHC-EP-0831, Rev. 0, Westinghouse Hanford Company, Richland, Washington, February 1995.

[14] Gasser, R. D., and Kazimi, M. S., "Onset of Convection in a Porous Medium with Internal Heat Generation," *J. Heat Transfer*, Vol. 98, 1976 pp. 48-54.

[15] Buretta, R., "Thermal Convection in a Fluid Filled Porous Layer with Internal Heat Generation," Ph.D. Thesis, University of Minnesota, 1972.

[16] Sun, W. J., "Convective Instability in Superposed Porous and Free Layers," Ph. D. Thesis, University of Minnesota, 1973.

[17] Hwang, I., "Finite Amplitude Thermal Convection in Porous Media With Heat Source and Variable Viscosity," Ph.D. Thesis, University of Minnesota, 1971.

[18] Ergun, S., "Fluid Flow Through Packed Columns," *Chemical Engineering Progress*, Vol. 48, 1952 pp 89-94.

[19] Wong, K., and Dybbs, A., "An Experimental Study of Thermal Equilibrium in Liquid Saturated Porous Media," *International J. Heat and Mass Transfer*, Vol. 18, 1976 pp. 235-235.

[20] Veronis, G., "Larger Amplitude Benard Convection," *J. Fluid Mechanics*, Vol. 26, 1966 pp. 49-68.

[21] Lapwood, E. R., "Convection of a Fluid in a Porous Medium," *Proc. Camb. Phil. Soc.*, Vol. 44, 1948 pp. 508-521.

[22] Bander, T. J., "Revised Thermal History of Tank 241-C-106," WHC-SD-WM-ER-200, Rev.0, Westinghouse Hanford Company, Richland, Washington, June 17, 1993.

[23] Bander, T.J., "An Assessment of the Potential for a Steam Bump in Hanford Waste Tank 241-C-106," WHC-SD-WM-ER-379, Rev. D, Westinghouse Hanford Company, Richland, Washington, September 29, 1994.

[24] Catton, I., "Natural Convection Heat Transfer in Porous Media," *Natural Convection: Fundamentals and Applications*, Hemisphere, 1985 pp. 514-547.

[25] Suo-Antilla, A. J., and Catton, I., "The Effect of Stabilizing Temperature Gradient on Heat Transfer From a Molten Fuel Layer," *J. Heat Transfer*, Vol. 97, 1974 pp 544-548.

[26] Somerton, C. W., "The Convective Instability of Inductively Heated Porous Bed With Applied Temperature Gradients," Master's Thesis, University of California, Los Angeles, 1979.

[27] Somerton, C. W., and Catton, I., "On the Thermal Instability of Superposed Porous and Fluid Layers," *J. Heat Transfer*, Vol. 104, 1982 pp. 160-165.

[28] Neale, G., and Nadar, W., "Practical Significance of Brinkman's Extension of Darcy's Law: Coupled Parallel Flows Within a Channel and a Bounding Porous Medium," *Canadian Journal of Chemical Engineering*, Vol. 52, 1974 pp. 475-478.

[29] Agnew, S.F., "Analysis of the History of 241-C Farm," LAUR-93-3605, Los Alamos National Labs, Los Alamos, N.M., 1993.

[30] Nield, D. A., "Onset of Thermohaline Convection in a Porous Medium," *Water Resources Res.*, Vol. 4, 1968 pp. 553-560.

[31] Hensley, P.J., and Savvidou, C., "Modeling Coupled Heat and Contaminant Transport in Groundwater," *International J. Numerical and Analytical Methods in Geomechanics*, Vol. 17, 1993 pp. 493-527.

[32] Zaytsev, I. D., et. al., ed., *Properties of Aqueous Solutions of Electrolytes*, CRC Press, 1992.

[33] Sohnel, O., and Novotny, P., "Densities of Aqueous Solutions of Inorganic Substances," Elsevier, Amsterdam, 1985.

[34] Chen F., and Chen C. F., "Onset of Finger Convection in a Horizontal Porous Layer Underlying a Fluid Layer," *J. Heat Transfer*, Vol. 110, 1988 pp. 403-409.

[35] Malkus, W.V.R., and Veronis, G., "Finite Amplitude Cellular Convection," *J. Fluid Mechanics*, Vol. 4, 1958, pp 225-260.

[36] Meksyn, D., and Stuart, J.T., "Stability of Viscous Motion Between Parallel Planes of Finite Disturbances," *Proc. Roy. Soc., Series A*, Vol. 108, 1951 pp. 517-526.

[37] Agnew, S.F., Los Alamos National Labs, July, 1994, (Letter to Charlie O'Dell of the Department of Energy).

[38] Apley, W. J., "Report on Techical Review of LANL Letter Report," (internal memorandum to R. E. Raymond), Westinghouse Hanford Company, Richland, Washington, July 1994.

[39] Hollands, K. G. T., Raithby, G. D., Konicek, L., "Correlation Equations for Free Convection Heat Transfer in Horizontal Layers of Air and Water," *International J. of Heat and Mass Transfer*, Vol. 18, 1975 pp. 879-884.

[40] Chu, T. Y., and Goldstein, R. J., "Turbulent Convection in a Horizontal Layer of Water," *J. of Fluid Mechanics*, Vol. 60(1), 1973 pp. 141-159.

[41] Fuji, T., and Imura, H. "Natural Convection Heat Transfer from a Plate with Arbitrary Inclination," *International J. of Heat and Mass Transfer*, Vol. 15, 1972 pp. 755-767.

[42] Holman, J. P., *Heat Transfer*, Fifth Edition, New York, NY, 1981.

[43] Collier, J. G., Boyce, B. E., DeForge Dedman, A. S., and Khanna, R., "Natural Convection Through Narrow Annular Vertical Unheated Annuli at High Gas Pressures," Fourth International Heat Transfer Conference Vol.4, paper NC 2.6, Hemisphere, 1970.

[44] Yamakama, M., and Sakai, T. "Analysis of Natural Convection in Narrow Annular Gaps of LMFBR," *J. of Nuclear Science and Technology*, Vol. 23 1986 pp. 451-460.

[45] Anderson, R. Lauriat, G., "The Horizontal Natural Convection Boundary Layer Regime in a Closed Cavity," Proceedings of the Eighth International Heat Transfer Conference Vol. 4, Hemisphere, 1986, pp. 1453-1458.

[46] Thomas, R. W., and de Vahl Davis, G., "Natural Convection in Annular and Rectangular Cavities, a Numerical Study," Fourth International Heat Transfer Conference, Paris, Vol. 4. paper NC 2.4, 1970.

[47] Prasad, V., "Convective Flow Interaction and Heat Transfer Between Fluid and Porous Layers," *Convective Heat and Mass Transfer in Porous Media*, Kluwer Academic Publishers, 1991 pp. 563-615.

[48] Rhee, S. J., "Natural Convection Heat Transfer in Beds of Inductively Heated Particles," Master's Thesis, University of California, Los Angeles, 1977.

[49] Cherng, J. C., "Effect of Bottom Cooling on Natural Convection in Saturated Porous Layers with Internal Heat Sources," Master's Thesis, University of California, Los Angeles, 1978.

[50] Taslim, M. E., and Narusawa, U., "Thermal Stability of Superposed Porous and Fluid Layers," *J. Heat Transfer*, Vol. 111, 1989 pp. 357-362.

[51] Rudraiah, N., "Flow Past Porous Layers and Their Stability," *Encyclopedia of Fluid Mechanics: Slurry Flow Technology*, Gulf Publishing, Houston, 1986.